Alma Mater Studiorum · University of Bologna

School of Science
Department of Physics and Astronomy
Master Degree in Physics

Nanoscale characterization of two Semi-Vertical GaN stacks by Scanning Probe Microscopy

Supervisor:
Prof. Daniela Cavalcoli

Co-supervisor:
Dr. Albert Minj

Submitted by:
Giulia Napolitano

Academic Year 2022/2023

Abstract

Energy-efficient power devices benefit from GaN's superior intrinsic properties, such as wide band gap, high electron-saturation velocity, and high thermal conductivity. However, the efficiency of GaN-based devices is hindered by the presence of dislocations within GaN stacks. In this work, structural and electrical properties of threading dislocations in metal-organic vapor-phase epitaxy-grown Si-doped GaN (0001) were determined by combining multiple scanning probe microscopy approaches. Specifically, two semi-vertical GaN stacks on QST® substrates, characterized by different buffer layers, were investigated. The dislocation density was quantified using Atomic Force and Electron Microscopy, aiding in the identification of the most suitable buffer layer. The space charge region at the dislocation sites was examined through differential capacitance measurements (dC/dV) via Scanning Capacitance Microscopy. Additionally, Conductive Atomic Force Microscopy revealed leakage spots on the surface, constituting approximately 1% of the dislocation density, compatible with the hypothesis that pure screw dislocations are electrically active ones. To comprehend the electrical transport mechanism, I-V curves were acquired at leakage spots and different models were fitted. Furthermore, distinct morphological features on one sample's surface were investigated and attributed to a gallium oxide adlayer. The impact of KOH etching on the GaN surface was also explored, linking the formation of anisotropic steps to nitrogen-dangling bonds.

Contents

Introduction

Global energy consumption is surging significantly faster than in previous decades due to the swift expansion in industry and economy. Consequently, energy-efficient technologies are necessary to mitigate the challenges due to this phenomenon. The latter mainly depends on the power electronic converters. Notably, more than 60% of energy utilized for electricity reproduction is lost during the conversion process. The efficiency

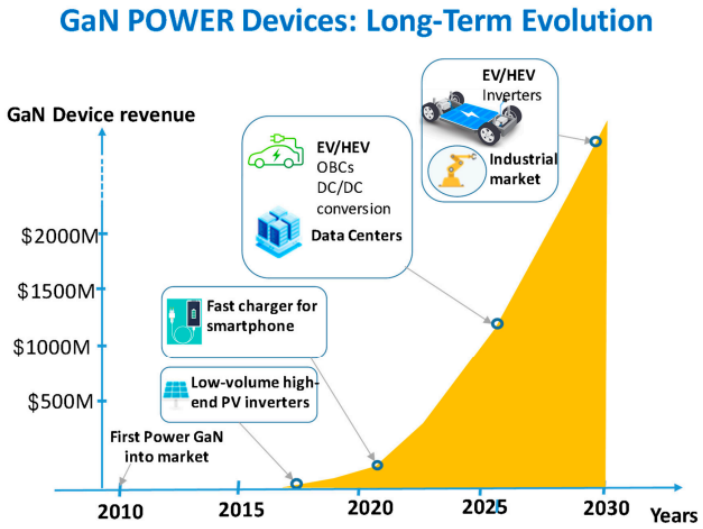

Figure 1: *GaN power electronic devices in long-term evolution for the Chinese market [1].*

of power electronics is determined by selecting a suitable semiconductor. In this context, GaN could operate at a high switch frequency to reduce the switching loss and increase the power density of the converters. The wide band gap of the semiconductor material results in a high critical electric field, which can lead to designs of electronic devices with a shorter drift region and therefore a lower on-state resistance when compared to a silicon-based device featuring the same voltage rating. Besides, it can reduce power electronics component size and likely cut down the system or component-level costs, while improving their performance and reliability. There are several fields of power elec-

tronics applications that benefit from the technological advancements of GaN devices, as shown in fig. 1, especially in the low-voltage (<200 V) power supply areas, which are, at present, having a growing impact on modern society, such as telecom/datacom, server SMPS, and wireless charging. Furthermore, it is an enabling technology for the integration of renewable energy with power converters, electric vehicles, industrial automation, and modular battery management systems, generally at a higher voltage rate (currently, 650 V is the standard for high-voltage GaN, with some power device fabrications achieving a maximum voltage of up to 1200 V) [1], [2].
However, due to the high cost of homoepitaxy, GaN is usually grown on silicon in commercial applications, and the lattice mismatch between these two materials induces a high dislocation density. This kind of defect is detrimental to the devices' electrical properties such as leakage current, blocking voltage, peak electric field, switching frequency, and dynamic ON resistance. For this reason, research is focused on developing strategies to reduce dislocation density, such as the employment of new substrates or different buffer layers. Moreover, the characterization of electrical properties of dislocations, still under debate, could be a crucial step for the optimization of these devices.
My thesis was carried out in the framework of a collaboration with the Physics and Astronomy Department (University of Bologna), Prof. Daniela Cavalcoli, and IMEC, an international research&development organization. I had the opportunity, supported by ERASMUS+, to perform a part of the traineeship at IMEC, as an intern of the Materials and Components Analysis (MCA) department in the Scanning Probe Microscopy (SPM) team. In particular, I was supervised by Thomas Hanstchel (thomas.hatschel@IMEC.be) and Albert Minj (albert.minj@IMEC.be). IMEC has been pioneering GaN technology for more than 15 years. It is actually working on QST® [3] substrate, in order to reach better quality of these devices. My work, summarized in this thesis, was focused on the structural and optoelectric characterization of two Semi-Vertical GaN stacks on QST® substrate, with different buffer layers. For this purpose, Atomic Force Microscopy, together with some of its modes such as Conductive Atomic Force Microscopy (C-AFM), Scanning Capacitance Microscopy (SCM), and Kelvin Probe Force Microscopy (KPFM), was employed. Moreover, I had the possibility to collaborate with a few scientists at IMEC in order to perform characterizations by Scanning Electron Microscopy (SEM), X-ray Photoelectron Spectroscopy (XPS), and Time-of-Flight Secondary Ion Mass Spectroscopy (ToF-SIMS).

The master thesis is organized as follows:

- **Chapter 1** presents GaN's fundamental properties, together with its main application. Dislocations are described in detail, mentioning the still ongoing debate about their electrical activity. Finally, how they impact negatively on GaN's devices features is summarized. Transport mechanisms that could lead to leakage

current are also presented

- **Chapter 2** is dedicated to the physical principles of the experimental methods employed. AFM, with its modes (C-AFM, SCM, KPFM), is introduced, as well as SEM, XPS, and ToF-SIMS. The advantages of dislocation-sensitive etching are also described. Besides, it provides a description of the samples' structure

- **Chapter 3** summarizes the main results achieved. In particular, it is divided into three main sections. The first is related to the study of dislocations with different techniques, in order to estimate their density and properties. The second section presents the study of some inhomogeneities, found on the surface of one of the samples, and how their origin was established. The third is about the attempt to explain the formation of highly directional steps after KOH etching

Chapter 1

Dislocations in GaN devices

1.1 GaN properties

Gallium Nitride is a III/V semiconductor, whose direct energy band gap is around 3.4 eV, used for power electronics and optical applications. This material can crystallize in two different structures: zincblende and wurtzite, which is the most thermally stable and so the easiest to synthesize. The wurtzite structure is commonly depicted as the hexagonal structure shown in fig. 1.1 (left). However, this is not the simplest repeating portion of the structure. Indeed, the unit cell can be seen in the section highlighted in red in fig. 1.1 (left), better shown on the right. GaN is usually grown in this lattice along (0001) orientation, characterized by lattice vectors a=3.216 $\mathring{A}$ and c=5.240 $\mathring{A}$, in fig. 1.2. In the GaN wurtzite structure, each Nitrogen atom shares electrons with the

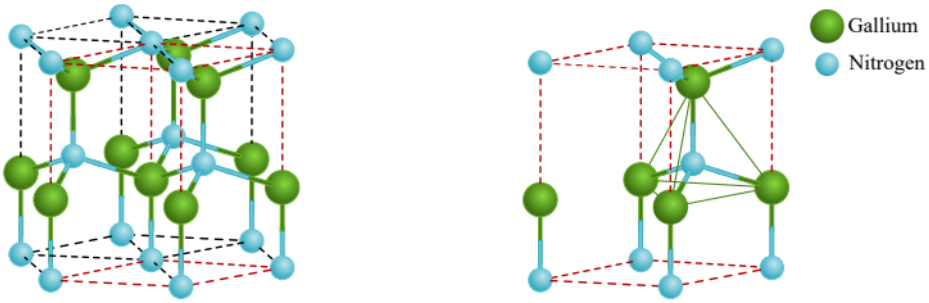

Figure 1.1: *Wurtzite structure (left) and unit cell of GaN (right). Polarization is along the (0001) direction [4].*

neighboring Gallium atoms by means of covalent bonds. However, due to Nitrogen's higher electronegativity, electrons have a tendency to remain closer to it. Consequently, a charge disparity arises between the atoms (with Nitrogen carrying a negative charge), resulting in the bond being partially ionic. Besides, GaN wurtzite structure is charac-

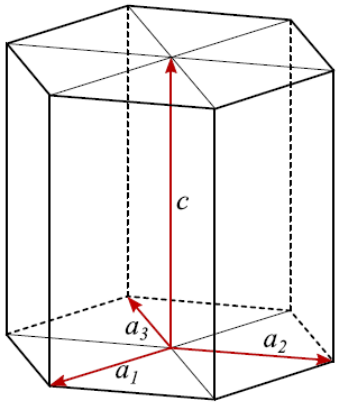

Figure 1.2: *Representation of Bravais-Miller index [4].*

terized by the lack of inversion symmetry. In particular, a crystalline structure exhibits this property if its unit cell is symmetrical with respect to its center point. So, for what concerns a unit cell, each atom inside has another identical atom equidistant from the center, but on the opposite side. The lack of inversion symmetry is a necessary condition for piezoelectric materials, that show electric polarization under mechanical stress [4] [5].

1.1.1 Piezoelectric Polarization

The piezoelectric polarization arises as a result of the mechanical strain exerted on the material. For instance, mechanical stress could emerge at the junction of two different materials. Given that the spacing between atoms differs in each material, at the junction, atomic distances need to adjust, inducing mechanical stress [6]. This mechanical stress will determine a modification in the bond angles, leading to an alteration in polarization at the material's level. In an ideal tetrahedron, the overall polarization is zero due to the symmetric distribution of electric charge across the tetrahedron. However, when mechanical stress is applied to the crystal, it can alter the bond angles between atoms. This disrupts the electric charge distribution within the structure, resulting in a nonzero net polarization. Within the wurtzite structure, as the c-axis lacks an inversion center, this nonzero net piezoelectric polarization is manifested at the material level.

1.1.2 Spontaneous Polarization

Because of asymmetries in the wurtzite arrangement, a certain polarization emerges at the material level along the c-direction axis even without the imposition of any mechanical stress. This inherent polarization is termed as spontaneous polarization. To simplify, it can be stated that the tetrahedrons lack perfect symmetry, resulting in some unbalance in their bond polarizations. Because of the absence of an inversion center, this overall

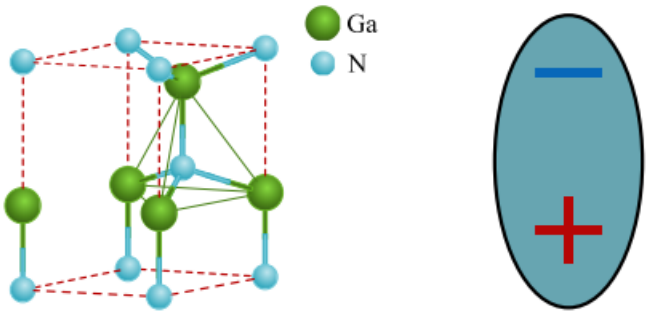

Figure 1.3: *Unit cell of the wurtzite structure and dipole representing the unit cell polarization [4].*

polarization is also mirrored within the material along the axis parallel to the c-direction.

Spontaneous and piezoelectric polarizations are always present along the c-axis. However, the direction of the polarization depends on the material orientation and the bond angle variation within the tetrahedron. Indeed, bottom and top polarizations are different and two polarities can be defined: Ga-polarity and N-polarity, also addressed as Ga-face and N-face or Ga-polar and N-polar. In GaN power devices, the Ga-polarity wurtzite is commonly used. In summary, there are two polarization types: the spontaneous polarization and the piezoelectric polarization. They are due to the lack of an inversion center of the wurtzite, resulting in an uncompensated polarization across the c-axis in the material. Therefore, a certain polarization appears in each unit cell and they can be represented a dipole, where there is a positive charge between the two ends (fig. 1.3) [7].

1.1.3 Doping

For what concerns doping, it has been demonstrated experimentally that GaN is characterized by n-type doping due to native defects (for example N vacancies) and impurities [8]. However, this type of doping is achieved and controlled by incorporating Si. The latter substitutes into a Ga-site, creating a single shallow donor with an activation energy of 12–15 meV, resulting in nearly complete donor ionization at room temperature. Due to the comparable electronic structural properties of Mg and Ga, Mg is extensively employed as a p-type doping element to create Mg-doped GaN. However, Mg creates a "quasi-shallow" acceptor level situated more than 170 meV above the valence band edge. The deep characteristic of this acceptor level results in a low acceptor ionization rate of several percent at room temperature. Consequently, excessively high Mg concentrations are required to achieve the desired effects [9]. Besides, the incorporation of atomic H significantly raises the resistance of Mg-doped GaN leading to the formation of Mg-H

neutral complexes [10]. Therefore, post-growth annealing steps are necessary to dissociate them and for the eventual removal of hydrogen from the crystal [11], [12].

Other band structure parameters of interest could be the effective density of states in the conduction and valence bands ($N_c = 2.3 \times 10^{18}$ cm^{-3} and $N_v = 4.6 \times 10^{19}$ cm^{-3} at room temperature), and the effective masses of electrons and holes ($m_e = 0.20$ and $m_h = 1.49$). The static and high-frequency dielectric constants are $\epsilon_s = 9.7$ and $\epsilon_h f = 5.3$ [5], [13].

1.2 GaN based devices

GaN offers several advantages over conventional Si power devices [14]. The energy to power conversion is the primary demand that stays for decades. However, the scientists are reaching the limit on how much Silicon and power efficiency can be improved for the transistors-based silicon. Recently, for this reason, wide bandgap (WBG) materials like SiC, Ga_2O_3, diamond, and GaN are receiving a lot of attention. The main features characterizing them are listed in table 1.1.

Materials	$\boldsymbol{E_g}$	ϵ	μ_n	$\boldsymbol{E_c}$	$\boldsymbol{V_{sat}}$	κ	***BFOM***
Si	1.12	11.7	1450	0.3	1	130	1
GaAs	1.42	12.9	8500	0.4	2	54	15
4H-SiC	3.26	10	950	3.0	2	500	340
GaN	3.39	9	1000	3.3	2.5	130	870
β-Ga_2O_3	4.8-4.9	10	300	8	2	20	3444
Diamond	5.6	5.7	4000	10	3	2000	24664

Table 1.1: *E_g (eV), ϵ, μ_n ($cm^2/V\ s$), E_c (MV/cm), V_{sat} (10^7 cm/s) and BFOM ($\epsilon\mu\ {E_{br}}^3$) are energy bandgap, relative dielectric constant, electron mobility, critical electric field, saturation velocity and Baliga's figure of merit, respectively, and thermal conductivity of (W/m K) [15], [16], [17].*

Their wider gap leads to a higher maximum electric field blocking capability. Thanks to the higher breakdown, a thinner drift layer is allowed, resulting in devices with lower ON resistance, further reduced by the high mobility. Moreover, higher saturation velocity and lower capacitances, allowed by the lower relative permittivity, enable faster switching

transients. Finally, the high thermal conductivity results beneficial for high power applications with demanding thermal requirements. As shown in table 1.1, GaN has a much higher Baliga's figure of merit (BFOM), defined as $\epsilon_s \mu E_{max}^3$, than SiC (which has been commercialized), a feature which is ascribed to its higher electron saturation velocity and higher critical electrical field. However, SiC has better thermal conductivity. Furthermore, GaN exhibits higher carrier mobility (μ) and thermal conductivity compared to Ga_2O_3, along with the ability to achieve both p-type and n-type doping. As shown

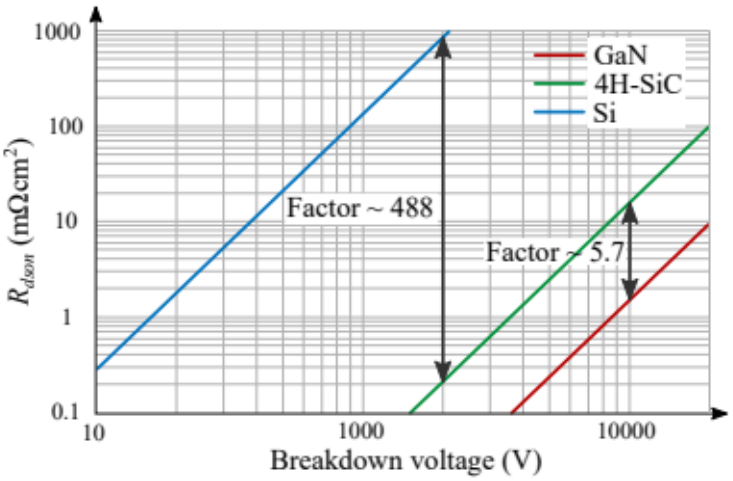

Figure 1.4: *Comparison of theoretical on-resistance in one dimension for unipolar Si, SiC and GaN devices [4].*

in fig. 1.4, that displays a comparison of the theoretical drift region ON-resistance of a n-type MOSFET, the minimum drift region resistance that can be obtained with GaN is about 5.7 times lower than SiC and about 2781 times lower than Si [4]. Thus, GaN material can considerably reduce the conduction losses of the power switching devices. Conversely, commercialization requires considerable progress. Up to now, GaN-based devices, such as three-terminal devices (Heterostructure field-effect transistors (HFETs) and MOSFETs), as well as two-terminal devices (Schottky barrier diodes (SBDs) and PN diodes (PNDs)), have emerged as critical areas of research, and significant advancements have been made in their applications for power rectification and power conversion [14].

Semiconductor power devices can be classified as diodes, transistors, and thyristors. For the sake of comparison between Si and GaN power devices (table 1.2), the discussion will be confined to diodes and transistors. A large part of GaN-based power device advancement work was directed towards lateral devices, namely HEMTs. GaN HEMTs (shown in fig. 1.5) provide a unique combination of features, including the ability to handle high current, voltage, and low ON-state resistance simultaneously. As a result,

Power devices	***Si***	***GaN***
Diodes	Schottky Epitaxial Double diffusion	Schottky Epitaxial
Transistors	BJT (npn, pnp) MOSFET IGBT	HEMT MOSFET JFET

Table 1.2: *WBG semiconductor power devices, comparison between GaN and Si [2].*

these devices can achieve high efficiency and high-power operation. A key component within GaN-HEMTs is the two-dimensional electron gas (2DEG), which forms an inherent channel between the drain and the source of the device. Its origin is a consequence of the formation of a triangular potential well due to band bending at the interface. Thus, electrons can move only in the parallel plane to the junction surface. This 2DEG channel enables efficient electron transport and contributes to the superior performance of GaN-based HEMTs, reducing the interaction that electrons may have with surrounding atoms. Besides, a high electron density is achieved without the need to dope the semiconductor. Since impurities added by dopants interact mostly with electrons, the lack of dopants in the 2DEG channel further improves the electron mobility. Therefore, the presence of this channel is vital for achieving high electron mobility and enhancing the device's overall capabilities in terms of power handling and switching speed. Indeed, while GaN presents an electron mobility around 1000 cm^2/Vs, the electron mobility in the 2DEG channel increases to around 1500 cm^2/Vs - 2000 cm^2/Vs and has an electron density around 10^{13} cm^{-2} [18].
Lateral GaN devices have inherent limitations when it comes to achieving high blocking voltages, generally capped at around 1200 V. Issues arise concerning the lateral current flow, particularly in proximity to the overlying dielectric and buffer layers, which can affect device performance and reliability. Additionally, the lateral device structures face challenges in simultaneously achieving very high voltages and currents for GaN HEMTs, limiting their applicability in high-power applications. Some of the main bottlenecks can be summarized as:

- the parasitic conduction at the buffer/substrate interface under high voltage
- the dynamic R_{ON} issues
- the normally-ON behavior

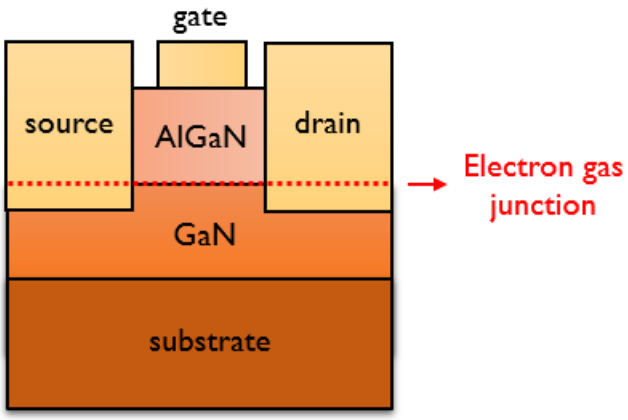

Figure 1.5: *GaN-HEMT basic structure representation and the dashed line shows a two-dimensional electron gas junction.*

To address these limitations and unlock the true potential of GaN technology, researchers have turned to vertical device structures, inspired by the design principles of their Si and SiC counterparts. Innovative approaches in both device engineering and materials processing have been developed. Figure 1.6 illustrates schematic drawings of vertical SBDs and PNDs designed to achieve minimum breakdown voltages (BV) of 600 V and 1200 V, respectively [2] [19].

1.2.1 Emerging vertical GaN power devices

Vertical GaN devices have emerged as promising candidates to expand GaN's application space into the medium-voltage range. Moreover, vertical devices are less susceptible to surface traps due to the typical location of the peak electric field inside the GaN layers. To date, various multi-kilovolt vertical GaN diodes and 1.2–2 kV vertical GaN transistors have been reported, featuring different architectures such as PN diode, Schottky barrier diode, junction barrier Schottky diode, current-aperture vertical electron transistor, trench MOSFET, fin-channel MOSFET, and fin-channel JFET. SBDs are fabricated through the patterning and deposition of palladium on the epitaxial layer of GaN. On the other hand, PNDs are constructed by in-situ development of a magnesium-doped epitaxial layer of p+ GaN on top of the epitaxial drift region of n-type GaN. Subsequently, patterning and deposition of palladium are performed to establish connections with the p-type GaN. The SBD demonstrates a forward threshold voltage of approximately 0.9 V, while the PND exhibits a threshold voltage of around 3.0 V. Both power diodes feature an active area of approximately 0.005 cm^2 and have demonstrated the capability to handle pulsed currents exceeding 10 A. Vertical GaN MOSFETs (fig. 1.7) present a favorable operation by providing a normally off solution, thus surmounting an important

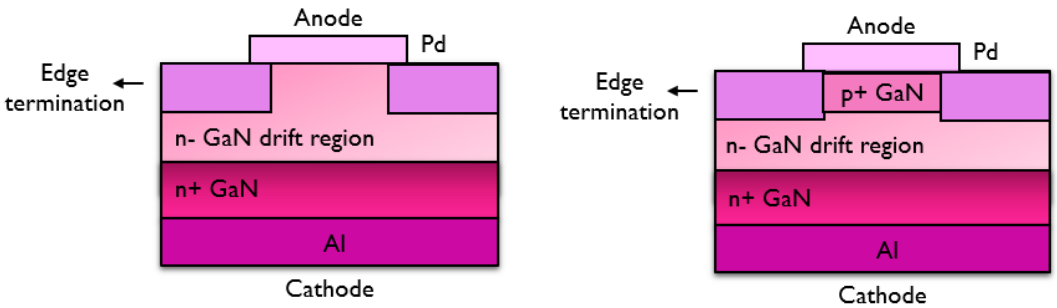

(a) *Schottky* **(b)** *PN junction*

Figure 1.6: *Schematic representation of vertical GaN power diodes: Schottky (left) and PN junction (right).*

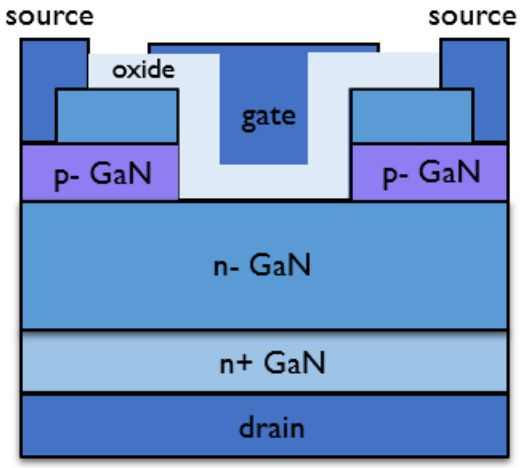

Figure 1.7: *Vertical GaN-MOSFET.*

drawback of any GaN HEMT-based construction. Although vertical GaN devices are still actively under development, they have successfully passed multiple traditional reliability qualification experiments, including High-Temperature Reverse Bias, High-Temperature Operating Life, temperature humidity bias, and temperature cycling. These experiments have revealed that fundamental failure mechanisms can often be attributed to the quality of the substrate and epitaxy material. Key factors influencing device performance and reliability include substrate orientation, surface preparation, and epitaxial growth initiation [20].

1.2.2 GaN optical devices

GaN is also a suitable material for blue-green emission in laser diode (LD) photoelectric devices, as well as light-emitting diodes (LEDs), due to the lower order of magnitude of the light transition probability in indirect bandgap materials compared to direct bandgap materials, along with its wide gap. Additionally, group III nitrides display high resistance to degradation caused by intense illumination and high currents, thanks to their strong chemical bonds. Moreover, the tunability of the Al-In-Ga-N composition enables the achievement of a band gap covering the entire visible spectrum, leading to the realization of primary light sources in blue, green, and red [21].

However, there are still some challenges affecting the breakdown, switching characteristics, and quantum efficiency for optoelectronic applications. In particular, the main source of these issues is related to dislocation defects. Due to the lack of cost-efficient bulk GaN substrates, the alternative is to use foreign substrates (Si, SiC, sapphire), cheaper and available up to 12 inches in diameter. However, these substrates are both lattice and thermal mismatched to GaN. This results in a high dislocation density (10^8-10^{10} cm^{-2}), due to the stress built up during growth. In order to reduce their density, IMEC is working on a different substrate, QST® (poly-crystalline AlN), developed by Qromis [22]. Moreover, as shown by Nakamura et al., the quality of GaN film can be further enhanced by the employment of a buffer layer, typically composed of an alternating sequence of GaN and AlGaN thin films. This buffer behaves as an intermediary between the substrate and the active GaN layer, providing a smooth transition between both layers and guaranteeing a good quality of the active GaN layer [23].

1.3 Threading dislocations

Dislocations are linear crystallographic defects that determine a change of the atomic positions in their neighborhood, with respect to the original sites. In these regions non-vanishing Burgers vectors exist (fig. 1.8). Their origin comes from the displacement of atoms in such a way as to minimize the strain. Grain boundary initiation and interface

interaction are common sources of dislocations. Dislocation lines can be considered as boundaries between slip and no-slip regions in a crystal. The magnitude and direction

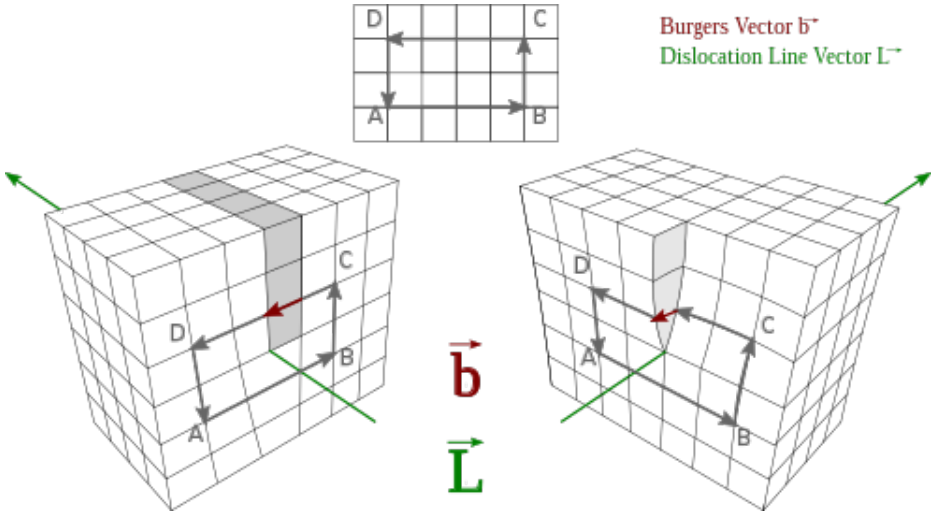

Figure 1.8: *Dislocations of edge (left) and screw (right) type. The red and green vectors represent the Burgers vector and the dislocation line respectively.*

of the slip are represented by Burgers vector, which is perpendicular to an edge dislocation (due to an extra (or missing) half-plane of atoms introduced mid-way through the crystal, distorting nearby planes of atoms), and parallel to a screw dislocation (parallel planes lose their identity becoming a continuous spiral ramp). Dislocations that are more complex than edge or screw dislocations can still be described by a single path-independent Burgers vector, though the relation between the direction of this one and the geometry of the dislocated region will not be as simple as for the previous cases. They are known as mixed dislocations [24], [25]. Dislocations can undergo different types of motion, each contributing to the deformation and mechanical behavior of materials. Dislocation motion is generally of two types, conservative and/or non-conservative, depending on whether the number of atoms in the neighborhood of a dislocation core changes as a result of the motion. As shown in fig. 1.9, an edge dislocation (A) can move conservatively by gliding in the slip direction (B), or non-conservatively by climbing in a direction normal to the slip plane (C) [26], [27]. A more detailed description of these types of motion is presented in the following:

- **Climb** is a type of edge or mixed dislocation motion movement perpendicular to its slip plane, through the diffusion of atoms or vacancies. It can be either positive or negative. In a positive climb, the dislocation acts as a vacancy sink, absorbing a vacancy in order to shift itself upwards. In a negative climb, it acts as a vacancy source and the vacancy at the bottom of an extra half-plane is replaced by an atom, which causes the dislocation to move downwards. Such a process

may occur in real crystals when atomic motion is assisted by substantial thermal agitation (i.e., deformation proceeds at a high temperature) and when the crystal possesses a population of point defects (interstitials and vacancies), which may become attracted to dislocation cores by virtue of their interacting stress fields. This is one of the processes that can remove dislocations from a sample when it is annealed at high temperatures

- **Glide** refers to the motion of dislocations within a crystal lattice under the application of an external force, such as shear stress. Dislocations can perform this kind of motion through the crystal lattice planes on a slip plane, along their slip direction. They are primarily responsible for plastic deformation in materials at a much lower stress than would be required to move a whole plane of atoms past another

- **Cross-slip** is a process in which pure screw dislocations move from one allowable slip system to another that shares the same slip direction. This phenomenon occurs when a dislocation meets an obstacle or another dislocation, and it switches its glide direction to continue moving within the crystal lattice. Cross-slip is essential in dislocation interactions and deformation mechanisms. Only pure screw dislocations can cross-slip, as their line and Burgers vector are parallel to each other, such that no unique slip plane normally exists. Because no atoms need to be added or removed by this process, cross-slip and screw dislocation motion, in general, are conservative

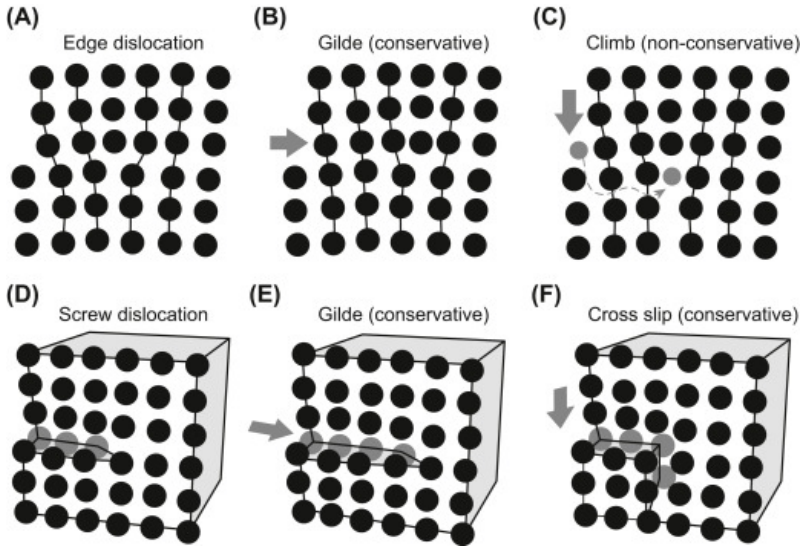

Figure 1.9: *Schematic representation of edge and screw dislocations with the type of conservative and non-conservative motion allowed for each one [26].*

A threading dislocation is one that extends from the surface of a strained layer system, goes through the layer, and penetrates the substrate or bends at the interface [28]. Threading dislocations occurring in hexagonal GaN along [0001] were found with a density reaching 10^{10} cm^{-2}. The main reason behind such structural deformations is the considerable disparity between the thermal expansion coefficients (α) and lattice constants (a_0) of the nitride layer and the substrates or between two nitride layer [29]. In-plane equilibrium lattice constant, the biaxial strain of a GaN layer pseudomorphically grown on the respective nitride layers or substrate, and the thermal expansion coefficient (at 600 K) are summarized in table 1.3.

	GaN	**AlN**	**InN**	**Al2O3(0001)**	**6H-SiC**	**Si(111)**
a ($\mathring{A}$)	3.190	3.110	3.544	4.759	3.073	3.840
$\epsilon_{\|\|,GaN}$	0	2.4	11.2	+49	3.6	+20.5
$\alpha(10^{-6}K^{-1})$	5.0	5.3	5.7	6.7	4.3	2.6

Table 1.3: *Properties of nitrides along (0001) and various substrates. Here a, $\epsilon_{||,GaN}$ and α are in-plane equilibrium lattice constant, the biaxial strain of a GaN layer pseudomorphically grown on the respective nitride layers or substrate and thermal expansion coefficient (at 600K), respectively [21].*

Threading dislocations can be classified according to their Burgers vector:

- **screw** (c) Burgers vectors parallel to dislocation line so that it is proportional to c. They could be full-core and open-core. According to DFT, they are supposed to introduce both shallow and deep states. The introduced energy levels are widely spread within the band gap and are distributed along the dislocation line, potentially leading to a metallic type of conduction
- **edge** (a) Burgers vector is 1/3(1120) and their formation occurs at the nucleation layer, with a subsequent propagation across the bulk. Their pits are smaller and grouped because it has been shown to be more energetically convenient
- **mixed** (a+c) As the name suggests, mixed-type TD consists of both the components of edge and screw with Burgers vector as 1/3(1123)

1.4 Electrical behavior of dislocations

Since the 1990s, dislocation electrical activity has been under debate due to the incoherence between the findings through different techniques. Several studies have been

performed in order to probe leakage, recombination, and charge state. For example, C-AFM results address leakage currents to open-core screw dislocations and full-core mixed ones. In particular, Hsu et al. show, by comparing the current maps to topographic images and transmission electron microscopy results, that reverse bias leakage occurs primarily at dislocations with a screw component [30]. Kim et al. performed C-AFM mapping shows two kinds of leakage current paths existing in the n-GaN layer: open-core dislocation and pure screw dislocation, with the first type associated with a more significant leakage current [31]. A completely different result was achieved by Wang et al. by studying an undoped GaN layer by C-AFM. In particular, full-core screw dislocations and mixed dislocations were found to provide conductive paths for device leakage currents, with edge and open core characterized by a less detrimental impact [32]. Hamachi et al. analyze the electrical characteristics of Schottky contacts on individual threading dislocations with a screw component to assess their impact on reverse leakage current. They found that both screw dislocations generating the significant leakage current and those producing the small leakage current had the same Burgers vector ($\mathbf{b}$=[0001]), along with a similar closed-core structure and helical propagation morphology. This suggested that the leaky screw TDs had an atomically different closed-core configuration that could have been locally formed via interactions with point defects during the climbing process [33]. On the other side, emission microscopy associates them just to full core screw dislocations, stating that open core are instead electrically inactive. Usami et al. identified a correspondence between leakage spots and some of CL dark ones. By performing KOH etching they classified etch pits on the base of their size and they observed just medium pits coinciding with leakage. TEM revealed also that pure screw dislocations were present under the leakage spots [34]. Besides, they claimed open-core structures to be electrically inactive [35]. Narita et al. investigated p-n diodes in reverse bias and, through EMS observations from the backside of each device, identified the current leakage paths and the same closed-core TSDs near each luminous point. Burgers vector of the extracted TSDs was identified as $\mathbf{b}$ =[0001] [36].
Regarding recombination properties, edge, and mixed types were pointed out as non-radiative recombination centers. Kaganer et al. described exciton dissociation as due to polarization-reduced field at (0001) surface termination, differing from Schockley Read Hall (SRH) recombination, where traps play the most important role. For this reason, further study on the charge state or charge-induced field at the location site could be important for a better understanding of recombination processes. Simpkins et al., through the employment of Kelvin Probe Force Microscope (KPFM), classified both edge and mixed dislocations as negatively charged in n-type GaN buffers, by measuring surface potential variations at their site. Another technique that can be employed for this purpose is Scanning Capacitance Microscopy (SCM), able to reveal the presence of space charge region around dislocations. This analysis also allows to access the drift layer, even after the growth of other layers on top (highly doped p-type layer, n+ layer, metallic

contacts, and passivation layer) and the multiple treatments that the sample undergoes (Mg-activation, ohmic contacts, passivation, etc.). Therefore, this technique provides the possibility to assess the alteration of electrical behaviour at TDS after all these steps.
These discrepancies related to the electrical properties probably arise from the employment of a classification based on Burgers vector instead of core structure, that depends on growth stoichiometry and can change during device processing steps. However, the mechanisms that regulate these processes are still unclear and further studies are needed in this direction.

1.5 Detrimental effects of dislocations

GaN is known to be more tolerant with respect to other III/V compounds for what concerns dislocations, that seem to be less detrimental. However, they still play an important role in power device failure, behaving as leakage paths for current.
For GaN devices, in order to overcome the competition in the power device market, it is required to exhibit normally-off behavior with high off-state blocking voltages and low off-state current leakage. In the following sections, it is summarized how different features of power devices are affected by dislocations. Before, to understand these phenomena it is essential to understand the trap concept due to crystal structure imperfections.

1.5.1 Basics of semiconductor defects traps

In the manufacture of a semiconductor, the resulting crystal structure is usually not perfect and impurities could be introduced. These defects can manifest in various forms, such as the presence of foreign atoms or cracks in the crystal structure. They can introduce localized levels within the semiconductor energy gap. Depending on the distance from the band edges in terms of energy, it is possible to classify them as:

- **shallow level** placed few k_BT far from conduction/valence band
- **deep level** placed several k_BT away from conduction/valence band

A scheme is reported in fig. 1.10. When imperfections create shallow level traps, the trapped charges can be re-emitted back into the CBM or VBM via phonon absorption, activated by the thermal effects. The energy levels of a shallow trap usually are created by intentionally introducing impurities (dopants) into the semiconductor material in order to manufacture electronic devices such as MOSFETs or diodes. In contrast, deep traps are usually generated by unintentional defects in the crystal structure, rather than by intentional doping. Deep traps can have a negative impact on the performance of a semiconductor, because they cannot be thermally excited, preventing carriers from flowing freely through the material and eventually behaving as recombination centers [37].

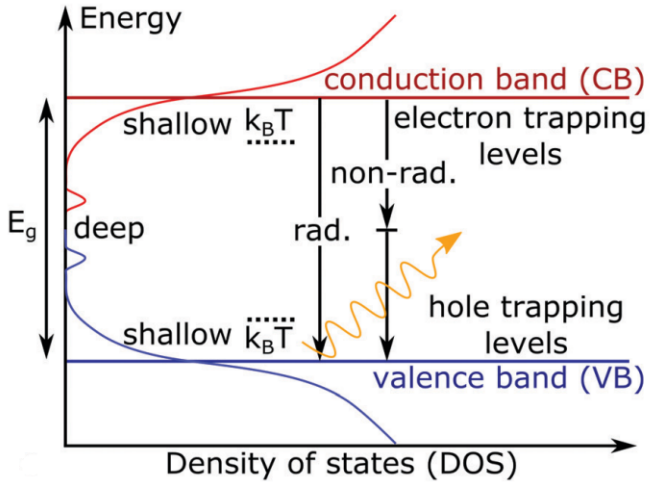

Figure 1.10: *Schematic representation of state density in a disordered semiconductor, whereby both band-to-band radiative and non-band to-band non-radiative recombination (vertical arrows) can occur [37].*

1.5.2 Breakdown voltage

Besendörfer et al. showed how conductive dislocations influence forward and reverse characteristics of AlGaN/GaN Schottky diodes as well as on gate failure of AlGaN/GaN HEMTs in OFF-state. Indeed, a shift of the turn-on voltage of AlGaN/GaN Schottky diodes to lower absolute values with the increasing of conductive TD density and gate failure of AlGaN/GaN HEMTs in OFF-state, when located at the drain side of the gate edge, were observed. Fig. 1.11 shows the drain bias at which gate failure is observed, related to the number of conductive TDs at the gate edge. The breakdown is believed to occur according to the percolation theory [38]. In vertical GaN diodes, increased blocking voltage directly depends on increased drift layer thickness (reverse breakdown voltages >3.9 kV have been reported for devices with drift layers 30 μm thick). The breakdown process is expected to occur through the avalanche process. Experimental evidence has indicated that breakdown voltage remains largely unaffected by threading edge dislocations but decreases with an increased density of threading screw dislocations, even though the edge dislocation density is significantly higher in all instances. Indeed, they act as carrier traps that produce localized sites of increased electric fields that contribute to breakdown. It is difficult to find a direct correlation between threading screw dislocation density and breakdown voltage because both are independent functions of increased drift layer thickness. The dislocation density decreases with increased drift layer thickness due to dislocation-pair annihilation and generation of dislocation loops. On the other side, breakdown voltage increases due to a larger area of electric field distribution. Although the precise breakdown mechanisms and their connection to the

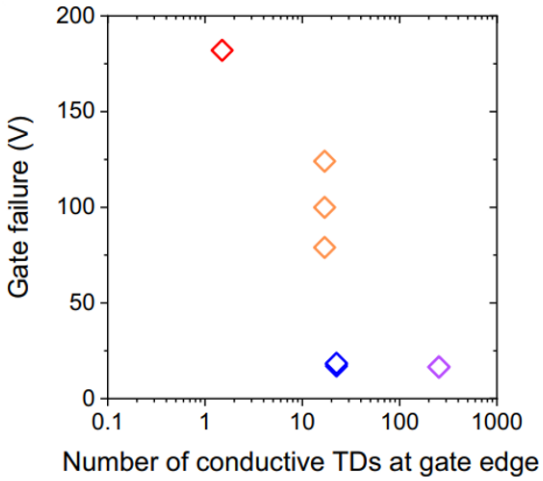

Figure 1.11: *The drain bias at which failure is observed is related to the number of critical dislocations located at the drain side of the gate edge as statistically expected from C-AFM measurements [38].*

electric field are still under investigation, it is widely acknowledged that an inherent breakdown mechanism in devices involves the build-up of point defects at the gate edge due to carrier transport under high electric fields. Alongside point defects, the elevated density and mobility of dislocations in GaN lead to premature breakdown and restrict the peak electric field strength [39].

1.5.3 Switching frequency

Regarding the switching frequency, it is mainly determined by intrinsic mobility and device geometry. GaN is characterized by carrier mobility twice that of SiC, so it is considered an excellent candidate material for ultra-high frequency applications. TDs, placed in the carrier path of the device, can be the source of scattering and charge-trapping processes, reducing switching frequency. Specifically, the decrease in carrier mobility has been linked to unpaired bonds along the edges of dislocations, which behave as electron traps, leading to the creation of negatively charged intrinsic areas within the 2DEG. These areas then act as centers for Coulomb scattering. Besides, edge dislocations have been demonstrated to generate a strain field that induces deformation potential scattering. Both scattering mechanisms might also be relevant for screw dislocations. However, edge dislocations are more abundant, so their impact could overshadow the effects of screw dislocations. Consequently, any attempt to differentiate the effects based on the type of dislocation becomes challenging.
When considering the device's shape, the complete 2DEG channel within planar HEMTs

runs across threading dislocations. In the case of vertical devices, the current flows vertically towards the ohmic contact and might only move perpendicular to dislocations shortly or not at all, depending on how the device is designed. Of course, the length of the channel has a significant influence over the switching speed, given that these two factors share an inverse relationship. The use of a vertical configuration for the device can mitigate these scattering challenges, thanks to the reduced interaction between dislocations and carriers. In vertical devices, therefore, the frequency at which switching occurs is considerably less affected by dislocations and is primarily reliant on the length of the channel. However, this length poses a trade-off concern as the drift layer thickness must be increased to achieve higher blocking voltages.

1.5.4 Dynamic ON-Resistance

The dynamic ON-resistance (R_{ON}) emerges when the transistor's R_{ON} remains elevated following a high-voltage (OFF-ON) switching occurrence. Two models have been formulated to elucidate this phenomenon in planar GaN HEMT devices:

- **off-state trapping**, where significant off-state voltages facilitate the accumulation of electron-acceptor traps, leading to an increase in the quantity of trapped electrons. This effect becomes more pronounced with higher off-state voltages and extended off-state durations
- **hot electron trapping**, where high-energy electrons escape the 2DEG and become trapped in the passivation layer or within the gate-drain AlGaN region.

In both these mechanisms, the time required for these trapped electrons to be released is accountable for the dynamic R_{ON}. Figure 1.12 shows the evolution of the dynamic on-resistance as a function of the drain source voltage and the time. As previously noted, GaN is affected by a high density of charge-trapping dislocations and planar GaN HEMT devices are particularly susceptible to charge trapping due to the lateral alignment of the 2DEG and threading dislocations. Consequently, this device architecture experiences more pronounced dynamic R_{ON} in comparison to vertical devices. In fact, a comparison of dynamic R_{ON} concerning off-state voltage between lateral and vertical devices reveals that GaN HEMTs encounter a peak in dynamic R_{ON}, followed by a gradual decline in resistance, whereas vertical devices exhibit negligible alterations in it with increasing off-state voltage. While the precise mechanism underpinning the occurrence of the maximum dynamic R_{ON} and its subsequent decrease at higher off-state voltages in planar HEMTs is not yet fully comprehended, it is evident that vertical devices exhibiting current flow parallel to threading dislocations show enhanced dynamic performance.

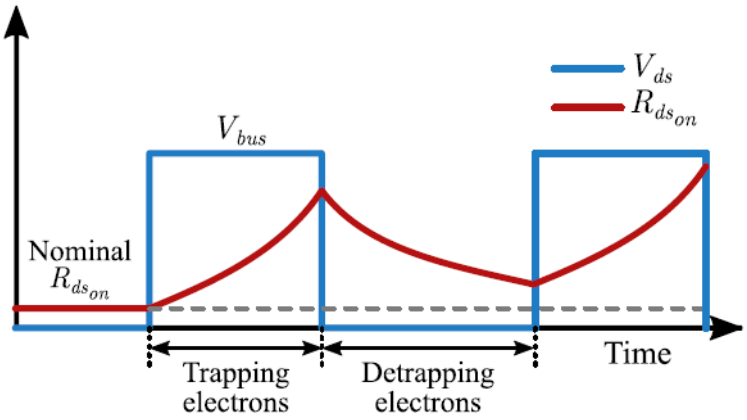

Figure 1.12: *Detrapping/trapping of electrons and its effect on the on-resistance [4].*

1.6 Conduction mechanisms through dislocations

In order to describe the leakage current mechanism, different models have been proposed. In particular, it is possible to distinguish conduction mechanisms influenced by the electrical properties at the interface between the electrode and the dielectric material (known as electrode-limited conduction mechanisms or injection-limited conduction mechanisms). In this case, the crucial parameter is the barrier height at this interface. On the other hand, there are also conduction mechanisms that depend on the properties of the dielectric material itself. These are called bulk-limited conduction mechanisms or transport-limited conduction mechanisms, with the primary parameter being the energy level of traps within the dielectric films.
In electrode-limited conduction mechanisms, dislocations might influence the situation by reducing the barrier height at the electrode-dielectric interface. In bulk-limited mechanisms, however, dislocation trap levels play a significant role. They will be explained in detail in this section [40] [41]. Fig. 1.13 shows the schematics through which these models can be represented. On top, the electrode limited mechanisms: Schottky emission and Fowler-Nordheim tunneling. Below, are the bulk-limited mechanisms: Poole-Frenkel emission and hopping conduction

1.6.1 Schottky or Thermionic Emission

It is a conduction mechanism that occurs if electrons manage to obtain enough energy provided by thermal activation to overcome the energy barrier at the interface. It is one of the most often observed mechanisms, especially at high temperatures. The expression

of Schottky emission is

$$J = AA^*T^2 exp\left[\frac{-q(\phi_B - \sqrt{qE/4\pi\epsilon_r\epsilon_0})}{kT}\right] \tag{1.1}$$

$$A^* = \frac{4\pi q k^2 m^*}{h^3} = \frac{120 m^*}{m_0} \tag{1.2}$$

where J is the current density, A^* is the effective Richardson constant, m^* is the effective one, T is the absolute temperature, q is the electronic charge, ϕ_B is the Schottky barrier height (i.e., conduction band offset), E is the electric field across the dielectric, k is the Boltzmann's constant, h is the Planck's constant, ϵ_0 is the permittivity in vacuum, and ϵ_r is the optical dielectric constant. For a standard Schottky emission, the plot of $log(J/T^2)$ versus $E^{1/2}$ should be linear. It is possible to get the barrier height from the intercept of the latter.

1.6.2 Fowler-Nordheim Tunneling

According to classical physics principles, if the energy of incoming electrons is below the potential barrier, these electrons will experience reflection. Nevertheless, in quantum mechanics, it is predicted that the electron's wave function will manage to cross the potential barrier, given the barrier's thinness (<100 $\mathring{A}$). Consequently, the probability of electrons being present on the opposite side of the potential barrier is not negligible due to the phenomenon known as tunneling. F-N tunneling comes into play when the applied electric field reaches a significant intensity, enabling the electron's wave function to penetrate the triangular potential barrier and transition into the conduction band of the dielectric material. The relationship that describes this phenomenon is

$$J = \frac{q^3 E^2}{8\pi h q \phi_B} exp\left[\frac{-8\pi(2qm^*)^{1/2}}{3hE}\phi_B^{3/2}\right] \tag{1.3}$$

This effect is dominant at low T, where thermionic emission is reduced. In this case, a plot of $log(J/T^2)$ versus $1/E$ should be linear.

1.6.3 Poole-Frenkel Emission

P-F emission engages a process quite similar to Schottky emission. In particular, the difference lies in the fact that this is a bulk-limited mechanism, as the barrier height that must be overcome is the one of trap states. Indeed, electrons can be thermally excited from traps to transition into the conduction band of the dielectric. Hence, P-F emission is sometimes referred to as internal Schottky emission. Imagine an electron confined within a trapping center; the Coulomb potential energy of this electron can be diminished by

an electric field applied across the dielectric layer. This reduction in potential energy might amplify the probability of an electron undergoing thermal excitation to escape from the trap and enter the conduction band of the dielectric material. For a Coulombic attraction potential between electrons and traps, the current density can be written as

$$J = q\mu N_c E exp\left[-q\left(\phi_T - 0.933\sqrt{\frac{qE}{\pi\epsilon_r\epsilon_0}}\right)\frac{1}{kT}\right] \tag{1.4}$$

where μ is the electronic drift mobility, N_c is the density of states in the conduction band, and $q\phi_T = \Phi_T$ is the trap energy level. The factor 0.933 has been inserted as an approximation, in order to account for the 3D nature of the emission, which was assumed to occur in a 1D-chain in the model used to get this equation. The plot of $log(J/E)$ versus $E^{1/2}$ is called the Poole-Frenkel plot and is expected to be linear [40].

1.6.4 Hopping conduction

Hopping conduction is due to the tunneling effect of trapped electrons "hopping" from one trap site to another one. Within P-F emission, the carriers have the capability to overcome the trap barrier, thanks to their thermal energy. In scenarios involving hopping conduction, the energy of the carriers is lower than the maximum energy of the potential barrier between two trapping sites. Nevertheless, they can still move by employing the tunneling mechanism. It is possible to state that the P-F emission corresponds to the thermionic effect and the hopping conduction corresponds to the tunnel effect. By assuming that under the Gaussian disorder mode the trap energy levels follow a Gaussian distribution centered at Φ_T, this introduces a trap mini-band. This framework is called Variable Range Hopping model (VRH). In this case, the mobility is modeled as

$$\mu = \frac{\nu_0 b}{2E} e^{-(\frac{\sigma}{kT})^2}[e^{(ebE/kT)} - 1] \tag{1.5}$$

where ν_0 (hopping frequency) = 10^{11} s^{-1}, b is the trap to trap distance), σ (energy dispersion) = 80 meV and E is the electric field. The hopping frequency can be further formulated as

$$\nu_0 = \Gamma_1 e^{(\frac{-4\pi}{h})\sqrt{2m^*\Phi_T}} \tag{1.6}$$

where Γ_1 is the attempt-to-escape frequency, m^* is the effective mass, Φ_T is the trap energy measured from the conduction band edge and h is Planck's constant [42].

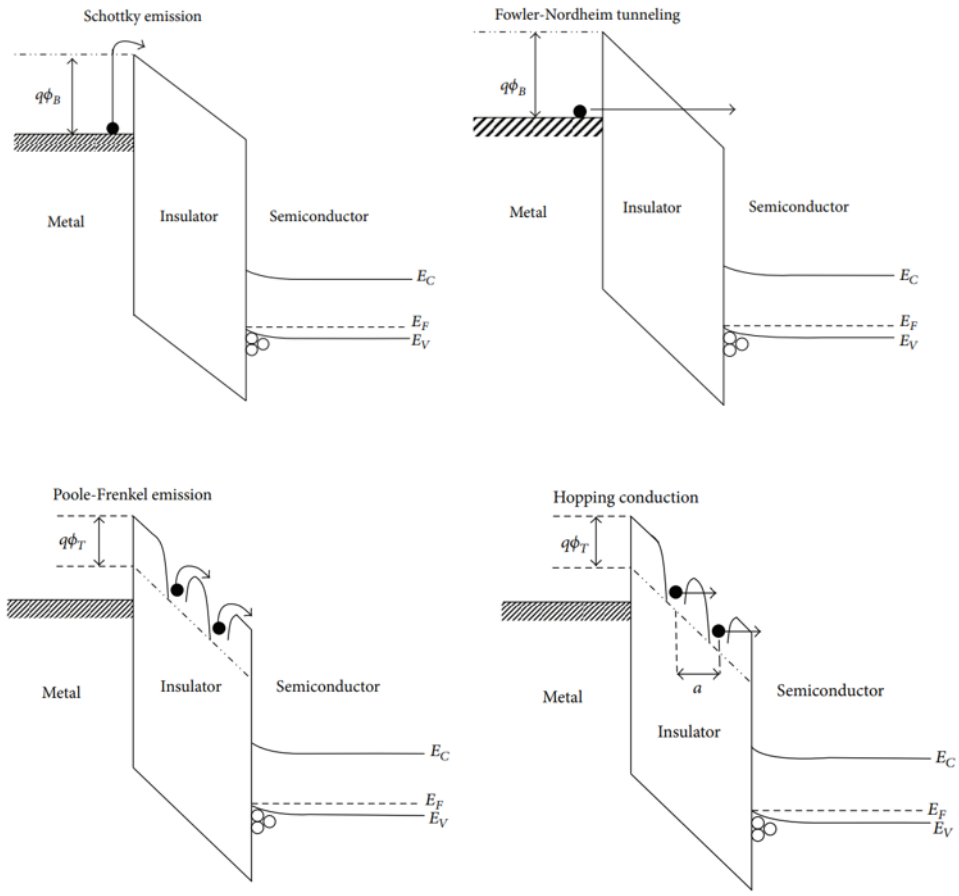

Figure 1.13: *On top, the schematic representations of electrode limited mechanisms: Schottky emission and Fowler-Nordheim tunneling. Below, there are the bulk-limited mechanisms: Poole-Frenkel emission and hopping conduction [40].*

Chapter 2

Materials and Methods

2.1 Samples

The present study was performed on three samples, portions of 200 mm blanket wafers (non-patterned) grown with AIXTRON's G5+ C fully automated metal-organic chemical vapor deposition (MOCVD) in IMEC. All three samples were grown on QST® substrate, produced by Qromis. QST® is an engineered wafer with a poly-AlN core and a conductive monocrystalline Si(111) layer at the front side, on top of a buried oxide. All the active device layers, intended for the fabrication of trench gate MOSFET devices, including the n+-GaN source layer, the p-GaN inversion channel layer, the n-type drift layer, and n+-GaN drain layer, were separated from the substrate by an unintentionally doped (UID) GaN buffer and strain management layers (SMLs). Fig. 2.1 (a) and (b) show their structure. The main difference between the first two samples is related to the use of an epitaxial lateral overgrowth (ELOG) technique in the unintentionally doped (UID) GaN layer of the stack (fig 2.1(b)), while for the other sample (fig 2.1 (a)) this technique was not used [43]. In the following, in order to distinguish them, they will be labeled according to the growth technique used in the UID GaN layer (UID and ELOG samples respectively). The third sample, depicted in fig 2.1 (c), was used as a reference because it has already been investigated in previous studies. While the latter is characterized by the drift layer on top (i.e. n-type), the other stacks were fully grown towards device fabrication. Two primary factors drove this choice. Firstly, halting the growth process would be a financial waste, considering industrial scale growths. Secondly, diffusion of Si from the layer into p-type layer and Mg-diffusion in top n+ layer at high growth temperatures would differ significantly from the reference case, where no such diffusion occurs. Therefore, exploring the entire device could be more interesting and reliable. It is possible that some differences could arise when compared to the reference sample, owing to the introduction of these additional layers.
Measurements were conducted on their surface, on the cross-section, and on beveled

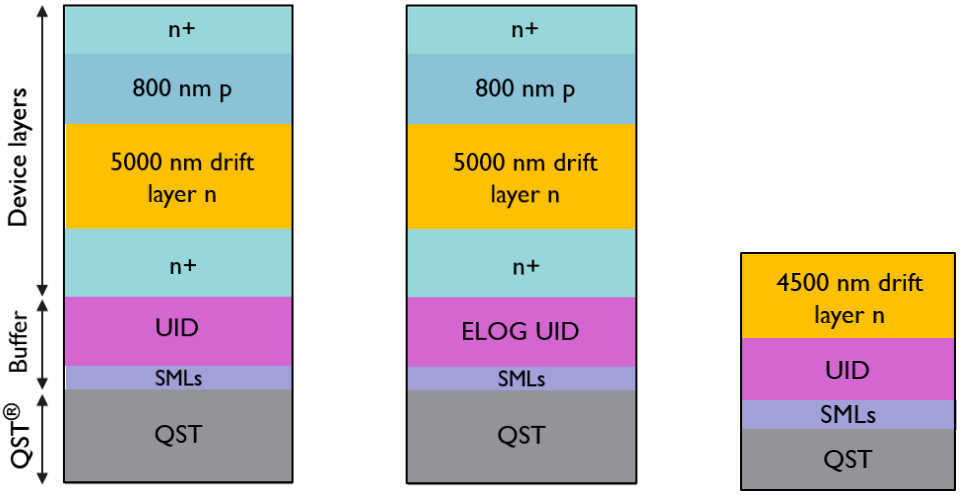

(a) *UID GaN without ELOG* **(b)** *UID GaN with ELOG* **(c)** *Reference sample*

Figure 2.1: *Structure of GaN stacks on QST® substrate. The main difference is the use of an epitaxial lateral overgrowth (ELOG) technique in the unintentionally doped (UID) GaN layer of one of the two stacks.*

samples. The latter methods allow us to study the electrical properties of threading dislocations in a fully fabricated device. Cross-sectional analysis was carried out on the cleaved plane (11-20), following the method employed by Ebert et al. The cleaving was performed in ambient conditions. Beveled samples were realized by conducting chemical mechanical polishing, which included multiple consecutive steps of grinding with polishing papers that have decreasing grain size. In one case it was combined with KOH etching, to achieve a smoother surface.

2.2 Atomic Force Microscopy (AFM)

Atomic Force Microscopy (AFM) is a type of Scanning Probe Microscopy (SPM) with a resolution of fractions of nanometer. This is achieved by measuring any force -van der Waals, electrical, magnetic- between a tip, through which the sample surface is scanned, and the sample under study. The measurement is performed by looking at the deflection of an elastic material, the cantilever, on which the tip is mounted. A laser beam is focused onto this one and reflected back on a photosensitive detector made by photodiodes (PSPD). The beam is adjusted to be at the center of the PSPD system, in such a way any photocurrent is measured. Cantilever deflection determines also a shift of this one,

and so the production of a photocurrent, exploited by the feedback system to move the tip in order to keep at a fixed value the interaction (known as SET POINT), by moving the piezoactuator in the z direction. Scanning is performed through an XY-piezoelectric actuator. This is represented in fig. 2.3.
Contact mode AFM is based on this principle and provides a direct measurement of the forces acting on the tip. Alternatively, the cantilever can be excited to vibrate at its resonant frequency. Under the influence of tip-sample forces, the resonant frequency (consequently also amplitude and phase) of the cantilever will change and serve as measurement parameters. This is called the **dynamic AFM**. If the tip approaches the surface, the oscillation parameters, amplitude, and phase are influenced by the tip-surface interaction, and can, therefore, be used as feedback channels. The second method prevents mechanical instability, also called "jump-to-contact", making the cantilever virtually stiffer at the point of strong force interaction. Therefore, the equilibrium point of the oscillation is still far away from the point of closest contact. This difference is shown in fig. 2.2. However, the drawback is related to the increased complexity of measurement interpretation. It is possible to distinguish between **tapping** and **non-contact mode**. In the first case, the cantilever vibrates with larger amplitudes and there is an intermittent contact with the sample surface. Instead, in the second case oscillation amplitudes are smaller, so that the probe is kept at a distance of several nm up to tens nm.
In dynamic mode, the oscillation trajectory of the cantilever is determined by three parameters: amplitude, phase, and frequency. Tip-sample interaction can affect all of them so that they are defined as internal parameters. The external ones are instead related to excitation amplitude and frequency. Tip-sample forces could be assessed only if all the parameters are measured, so feedback loops are employed to keep internal parameters constant, by adjusting the external variables. In the case of amplitude modulation mode (AM-AFM), the excitation frequency is set to a predefined value and the amplitude remains constant through the feedback. The amplitude is chosen at a frequency close to the resonance of the cantilever. When the force-distance curve reaches the repulsive part, the tip is hindered from indenting further into the sample, resulting in smaller oscillation amplitudes. An alternative is the frequency modulation mode (FM-AFM), in which the feedback system exploits the frequency as the set point. The main difference is that the changes in oscillation frequency are dependent on the force gradient when the restoring force of the cantilever that is associated with tip oscillating energy is large compared to the interaction force between the tip and sample surface. Therefore, this mode detects the force gradient rather than force itself, a factor enabling it to have higher spatial resolution than tapping [44], [45].
The possibility to control the motion of the sharp tip close to the surface led to the emergence of new electrical modes, that emerged as very promising in the field of semiconductors. Figure 2.4 shows Bruker's Dimension r-Icon and Park NX10, the two AFM tools employed during this thesis.

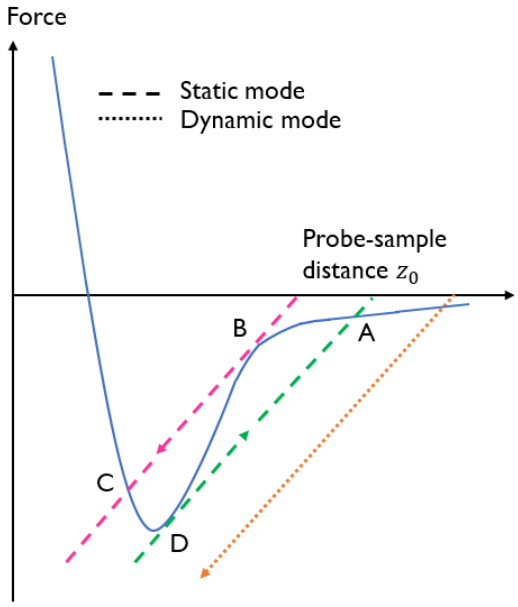

Figure 2.2: *Force–distance curve of a typical tip–sample interaction. In static-mode AFM the tip would follow the force curve until point B is reached. If the slope of the force curve becomes larger than the spring constant of the cantilever (dashed line) the tip will suddenly jump to position C. Upon retraction a different path will be followed along D and A again. In dynamic AFM the cantilever oscillates with a preset amplitude. Although the equilibrium position of the oscillation is far from the surface, the tip will experience the maximum attractive force at point D during some parts of the oscillation cycle. However, the total force is always pointing away from the surface, therefore avoiding an instability [44].*

2.2.1 Scanning Capacitance Microscopy (SCM)

In this technique, a metal-coated tip is scanned over an oxidized semiconductor surface in contact mode, employing the usual feedback circuit to keep a fairly constant cantilever deflection (fig. 2.5). The metal-coated tip and the oxidized semiconductor together form a metal-oxide-semiconductor (MOS) capacitor. The capacitance is related to the applied bias. Indeed, for a n-type semiconductor, if a positive bias is applied to the tip, there will be an accumulation of carriers at the semiconductor/oxide interface. Instead, if a negative bias is applied to the tip, a depletion layer will be created by the repulsion of carriers. It behaves as an additional dielectric layer, in series with the oxide one, decreasing the overall capacitance. When the bias becomes more negative, the inversion regime is achieved and capacitance returns to its original value. However, if the latter changes quickly, the inversion layer does not manage to form and the capacitance drops up to

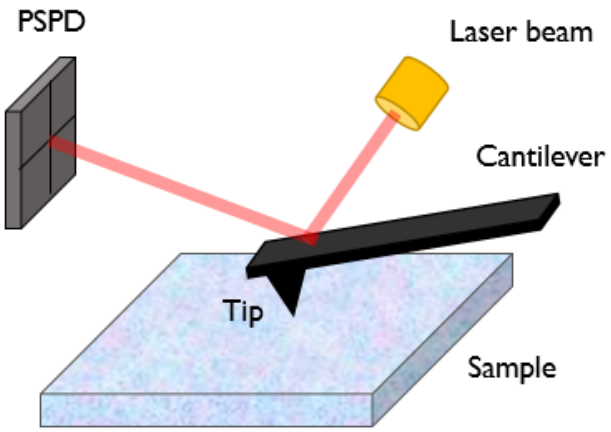

Figure 2.3: *Schematic diagram showing the several components of AFM.*

the breakdown (deep depletion). This behavior is shown in fig. 2.6. In SCM, a kilohertz frequency AC bias is applied to the tip to induce alternated accumulation and depletion of carriers (avoiding the formation of an inversion layer) and so capacitance changes. The latter is measured using an ultra-high frequency capacitance sensor. SCM images are constructed from the change in capacitance (dC) in response to the low-frequency sine wave voltage (dV) and represent the slope of the capacitance–voltage (C–V) curve at V_{DC}. As the tip moves from a region with a high carrier density to one with a lower carrier density, the output increases due to the steeper slope of the C–V curve (described by dC/dV amplitude) [46]. In fact, regions with fewer carriers deplete more easily, resulting in increases in the difference in capacitance between the accumulation and deep depletion regimes, and in the slope in the depletion regime. dC/dV phase signal allows to distinguish the type of doping, carrying information about the sign of the slope. By ramping the DC bias applied to the sample at each pixel, so that a dC/dV versus V curve may be recorded, Scanning Capacitance Spectroscopy can be performed [46].
Electrical properties of dislocations can be detected by exploiting this technique. In particular, the formation of skewed-funnel type local features, associated with a drop of $|dC/dV|$ in the drift layer could be related to the presence of dislocations surrounded by depletion/space charge region. The formation of a funnel-type contrast can be understood both from the conjunction of space charge regions of the p-n junction and around the dislocation or by interpreting this region as fully depleted i.e., with negligible electron density. This can be understood by the fact that the capacitance formed by the depletion region of the dislocations adds to the tip-sample junction capacitance in series, thereby reducing the net capacitance and consequently, the $|dC/dV|$ signal. For a better understanding of the differences in the SCM signal level between the dark regions and the

(a) **(b)**

Figure 2.4: *(a) Bruker's Dimension r-Icon. (b) Park NX10.*

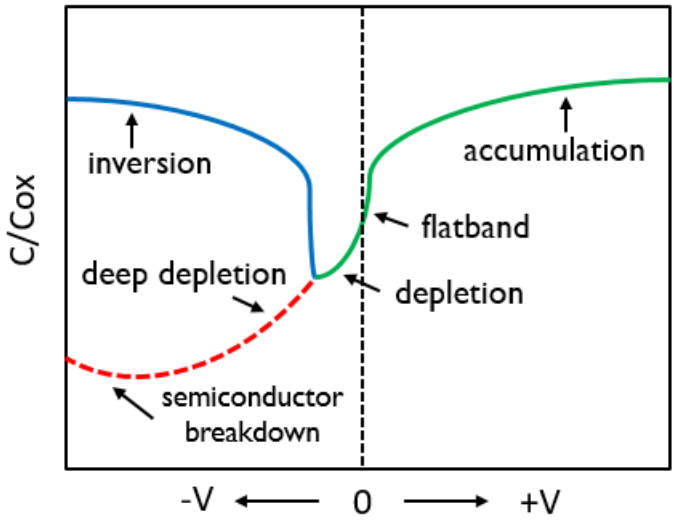

Figure 2.5: *Schematic C–V curves for an n-type semiconductor for low-frequency bias changes (solid line—inversion) and high-frequency bias changes (dashed line—deep depletion). Cox is the capacitance of the oxide layer at the semiconductor surface*

rest of the film, local C–V curves could be acquired both near and far from dislocations, with the tip held stationary on the sample surface. The presence of dislocations would

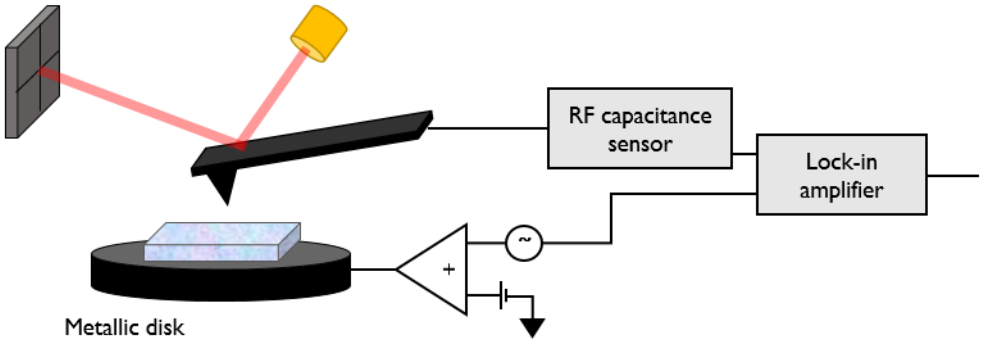

Figure 2.6: *Schematic diagram of Scanning Capacitance Microscope.*

Technique	SCM
Information	Carrier type, concentration Traps, fixed charges
Maximum Sensitivity	10^{-22}F $Hz^{-1/2}$
Capacitive Frequency Range	900 MHz to 1050 MHz
Spatial Resolution	20 nm

Table 2.1: *The table summarizes the possible information achievable by SCM, together with basic performance specifications [48]*

affect the signal through a shift of the flatband potential, due to the presence of charge nearby and to a smaller capacitance (larger depletion depth) [47].

2.2.2 Conductive Atomic Force Microscopy (C-AFM)

A conductive tip is scanned in contact with the sample surface, while a bias is applied to them, in order to probe both sample topography and local current. An electric circuit, with current amplifiers and filters, monitors the current. A schematic is shown in fig. 2.7. Instrumentally, the distinction is sometimes made between C-AFM, which employs a linear current amplifier, with a range 2 pA - 1 μA, and TUNA which has a lower noise floor (40 fA) and employs a more sensitive linear current amplifier, with a range from 50 fA to 120 pA. This instrument could be also used to measure I-V curves at a desired point of the surface: current is measured while voltage is ramped. By fitting them it is possible to identify the main transport current mechanism on stage. Dislocations could

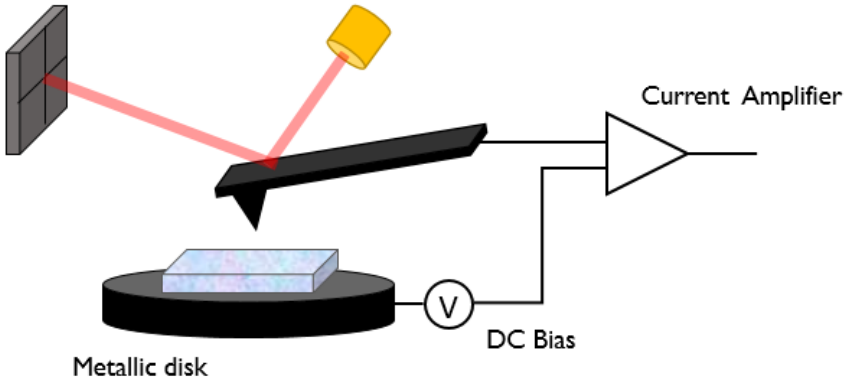

Figure 2.7: *Schematic diagram of Conductive Atomic Force Microscope-*

Technique	C-AFM (TUNA)
Information	Schottky barrier height
	Leakage paths
	Spreading resistance
Electrical Resolution	1 pA
Spatial Resolution	10 nm

Table 2.2: *The table summarizes the possible information achievable by C-AFM, together with basic performance specifications.*

provide pathways for leakage currents, so C-AFM seems useful to identify the location of electrically active ones [46].

2.2.3 Kelvin Probe Force Microscopy (KPFM)

KPFM was introduced as a tool to probe the local contact potential difference (CPD) between a conductive tip and the sample, thereby mapping the sample work function or surface potential with high spatial resolution. Indeed, these quantities are linked by the following relationship

$$V_{CPD} = \frac{\phi_{tip} - \phi_{sample}}{-e} \tag{2.1}$$

In this case, AFM operates in intermediate and non-contact modes, respectively related to the change in oscillation amplitude and resonance frequency as the feedback signal. Therefore, intermediate mode and non-contact mode are referred to as amplitude modulation (AM) and frequency modulation (FM) operation, respectively. Its components are shown in fig. 2.8. In particular, when an AFM tip is brought close to the sample surface,

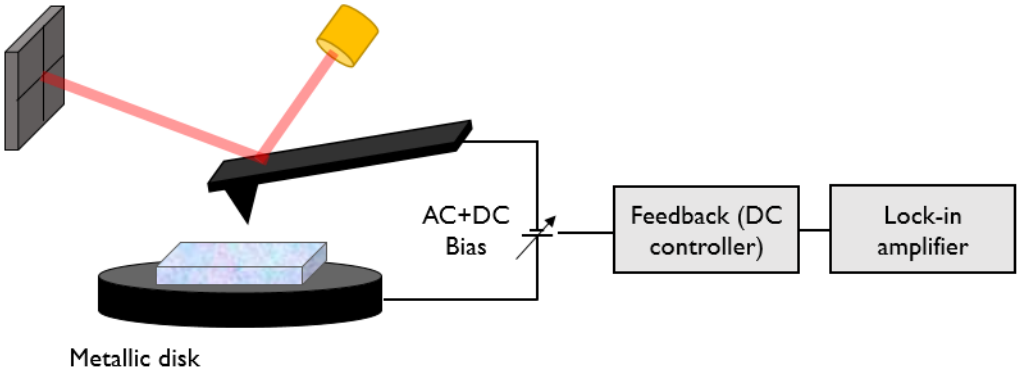

Figure 2.8: *Schematic diagram of Kelvin Probe Force Microscope.*

an electrical force is generated between this one and the tip, because of the differences in their Fermi energy levels. An electrical force acts on the contact area, due to the V_{CPD}. This force can be nullified: if an applied external bias (V_{DC}) has the same magnitude as the V_{CPD} with opposite directions, the applied voltage eliminates the surface charge in the contact area. The amount of applied external bias (V_{DC}) that nullifies the electrical force due to the V_{CPD} is equal to the work function difference between the tip and sample. The three steps of this process are schematized in fig. 2.9. By applying an AC voltage (V_{AC}) and a DC voltage (V_{DC}) to the AFM tip, KPFM manages to measure the work function of the sample. Indeed, V_{AC} is employed to get oscillating electrical forces between the AFM tip and sample surface, while V_{DC} nullifies the oscillating electrical forces originating from CPD between tip and sample surface. The electrostatic force (F_{es}) between the AFM tip and sample is given by:

$$F_{es}(z) = -\frac{1}{2}\Delta V^2 \frac{dC(z)}{dz} \tag{2.2}$$

With dC/dz as the gradient of the capacitance between the tip and sample surface and ΔV, the difference between V_{CPD} and the voltage applied to the AFM tip, given by

$$\Delta V = V_{tip} \pm V_{CPD} = (V_{DC} \pm V_{CPD}) + V_{AC} sin(\omega t) \tag{2.3}$$

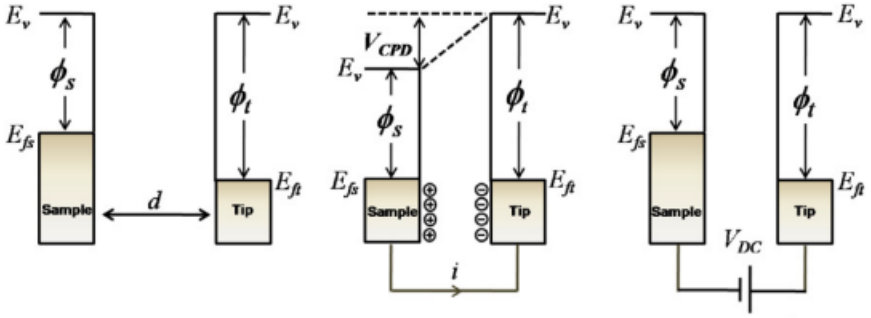

Figure 2.9: *Electronic energy levels of the sample and AFM tip for three cases: tip and sample are separated by distance d with no electrical contact, tip and sample are in electrical contact, and external bias (V_{DC}) is applied between tip and sample to nullify the CPD and, therefore, the tip–sample electrical force. E_v is the vacuum energy level. E_{fs} and E_{ft} are Fermi energy levels of the sample and tip, respectively [45].*

The sign is related to the fact that the bias is applied to the sample(+) or the tip(-). Substituting the definition of ΔV, the result is an equation made by three parts

$$F_{DC} = -\frac{\partial C(z)}{\partial z}\frac{1}{2}(V_{DC} \pm V_{CPD})^2 \tag{2.4}$$

$$F_{\omega} = -\frac{\partial C(z)}{\partial z}(V_{DC} \pm V_{CPD})V_{AC}sin(\omega t) \tag{2.5}$$

$$F_{2\omega} = \frac{\partial C(z)}{\partial z}\frac{1}{4}V_{AC}^2[cos(2\omega t) - 1] \tag{2.6}$$

F_{DC} determines a static deflection of the AFM tip. F_{ω} is used to measure the V_{CPD}, and $F_{2\omega}$ can be exploited for capacitance microscopy. A lock-in amplifier is employed to measure the V_{CPD}, to extract the electrical force component with frequency ω. The output signal of the lock-in amplifier is directly proportional to the difference between V_{CPD} and V_{DC} [45].

2.2.4 Conductive AFM tips

The techniques described above require the use of a conductive probe connected to an external source (where the probe indicates the entire assembly of tip, cantilever, and chip). We used alternatively Pt/Ir coated Si probes (PPP-NCSTPT from NanoAndMore) and diamond tips produced at IMEC. The first is the simplest and cheapest choice. Coating in a noble metal is useful to prevent oxidation from affecting the measurements. However, in some cases, the lateral forces experienced by these ones in contact mode can result in wear and de-adherence of the metal film. To solve this issue, diamond tips can be employed. These ones are characterized by sharp, hard diamond peaks

Technique	KPFM
Information	Surface potential Band bending Defects
Energy Resolution	5-20 meV
Spatial Resolution	Better than 10 nm

Table 2.3: *The table summarizes the possible information achievable by KPFM, together with basic performance specifications [45].*

leading to very good resolution and resistance to wear, leading to higher stability. Also, Adama diamond tips were employed for one kind of measurement, in which very high stiffness was required. In order to realize electrical measurement, samples were attached to a conductive sample holder with conductive silver paste. Additionally, indium was deposited in the silver paste through a heating pen, to get a better contact.

2.3 Scanning Electron Microscopy (SEM)

Scanning Electron Microscopy (SEM) exploits a focused, high-energy electronic beam to produce images of a sample. Electrons-sample interactions could be different and reveal several pieces of information about the investigated material. In particular, it provides detailed information on surface topography via secondary electrons (SE), and surface chemistry via backscattered electrons (BSE), allowing energy or wavelength-dispersive X-ray spectroscopy and cathodoluminescence. In addition, SEM can provide crystallographic information via electron backscatter diffraction (EBSD) [49].
The beam of electrons is produced at the top of the microscope by an electron gun. The electron beam follows a vertical path through the microscope, which is held within high vacuum. The beam travels through electromagnetic fields and lenses, which focus it down toward the sample. A schematic diagram of its structure is shown in fig. 2.10 (a). A FEI Apreo SEM was used during my internship (fig. 2.10 (b)).
Secondary electrons (SE) are produced when incident electrons excite other electrons in the sample losing some of their energy in the process. The excited electrons move towards the surface of the sample and, if they still have sufficient energy, they escape from the surface. Alternatively, when the electron beam strikes the sample, some of the electrons are elastically scattered (deflected from their original path) by atoms in the specimen.

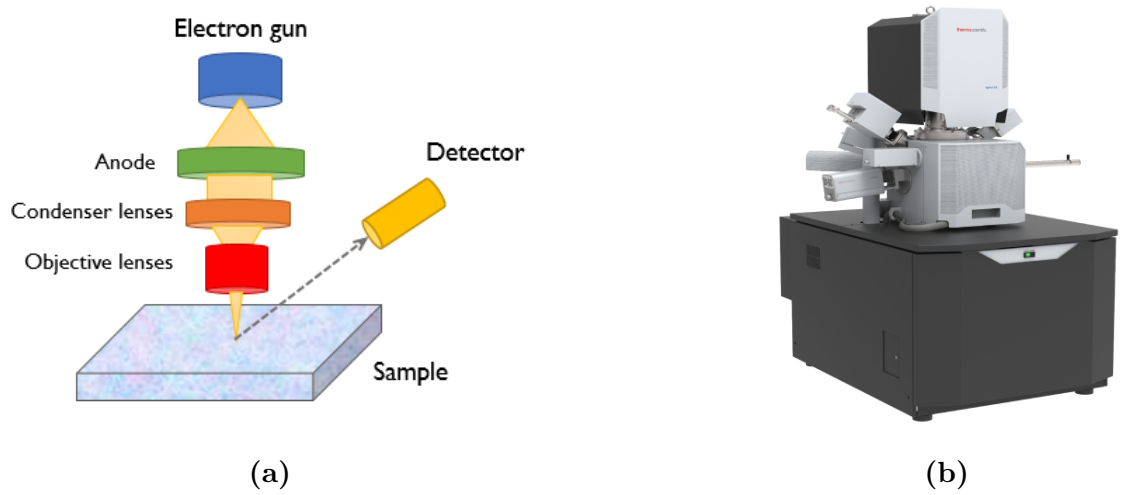

(a) **(b)**

Figure 2.10: *(a) Schematic diagram of Scanning Electron Microscope. (b) FEI Apreo SEM.*

The ones that rebound from the sample surface are called backscattered electrons (BSE). The primary beam electrons can also excite transitions of specimen's electrons, leading to emitted radiation when they relax back to the ground state. UV/visible/near IR EM radiation is related to Cathodoluminescence (CL) phenomenon. Also, X-rays could be produced by this interaction and eventually exploited to map the chemical composition of the sample.

2.3.1 Electron Channelling Contrast Imaging (ECCI)

This technique is based on the exploitation of BCE for detailed characterization of structural properties. Electron channeling contrast images are produced from electrons that channel down, or equivalently are diffracted from the crystal planes of a suitably oriented sample. Changes in crystallographic orientation or changes in lattice constant due to local strain are revealed by correspondent changes in contrast in a channeling image. The measurement is acquired by monitoring the intensity of BCE as an electron beam is scanned over the sample. Dislocations could block (or open) a channel, leading to a higher (lower) number of BCE and appearing as spots with black-white contrast.
In order to select the set of planes ("diffraction vector **g** selection") from which electrons are diffracted it is necessary to change the angle of the incident beam and to record the intensity variation. Different planes would satisfy Bragg conditions, giving rise to overlapping bands of bright and dark lines (Kikuchi lines), known as Electron Contrast Pattern (ECP). The point on ECP around which the electron beam is rocked is referred as the pattern center (PC). If a Kikuchi line intersects the PC, the corresponding plane

Technique	SEM
Information at nanoscale	Surface structure and defects Average elemental information Elemental composition
Resolution	1-10 nm
Depth of field	4mm–0.4mm
Magnification	10x–3000000x

Table 2.4: *The table summarizes the possible information achievable by SEM, together with basic performance specifications.*

provides channeling contrast.
In principle, ECCI allows us to distinguish between dislocation types on the base of B-W contrast direction [50].

- **screw dislocations** two possible directions for B-W contrast **b** of [000±1] for a given **g**
- **edge dislocations** the direction of B-W contrast depends on **b** and not on **g**. As GaN is a wurtzite semiconductor there are six possible **b**$(1/3 < 11\text{–}20 >)$ and so six directions for a given **g**, at 60° to each other
- **mixed dislocations b** is the vector sum of their edge and screw components (**b**$(1/3 < 11\text{–}23 >)$).There are 12 possible **b** for mixed dislocations at 30°

In order to resolve dislocations with this kind of technique, a small (nm), high brightness (nA or higher), low divergence (a few mrad) electron beam is needed.

2.3.2 Cathodoluminescence (CL)

The electronic beam excites the material and causes it to emit photons as it returns to the ground state. In the present study, the employed detector was panchromatic and operated in an energy range of 1.1-4.1 eV.
Dislocations are expected to be non-radiative recombination centers, that reduce minority carrier concentration over a cylinder around them and consequently also the intensity of CL signal, leading to dark regions. In principle, intensity profiles recorded across these

areas of reduced luminous efficiency contain information on both the minority-carrier (or, in GaN, exciton) diffusion length and the recombination strength of the dislocation [51].

2.4 X-ray Photoelectron Spectroscopy (XPS)

XPS is a fundamental technique in modern surface and materials science for the determination of surface chemistry, bonding structure, and composition of surfaces and interfaces. Indeed, it is a surface-sensitive analytical technique, in which soft X-rays (almost 6 keV) bombard the surface of a material and the kinetic energy of the emitted electrons is measured. Photoelectron emission occurs due to a complete transfer of the x-ray energy to a core-level electron. Fig. 2.11 shows a schematic diagram of XPS instru-

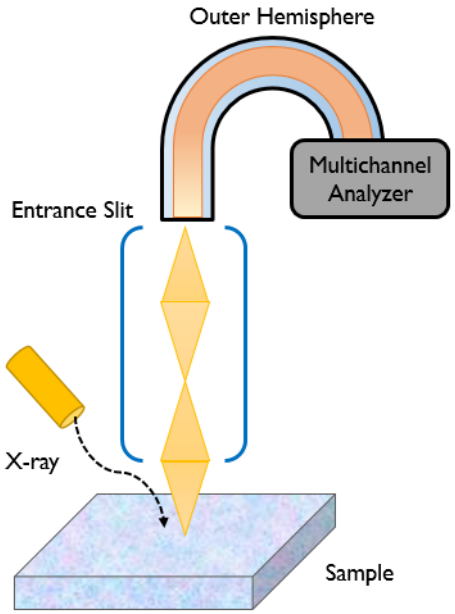

Figure 2.11: *Schematic diagram shows the major components of XPS instrument.*

ment, containing an x-ray source, sample stage, extraction lenses, analyzer, and detector housed in an ultra-high vacuum environment. They are housed within an ultra-high vacuum (UHV) environment to avoid surface contamination and the scattering between electrons and air molecules during the travel toward the analyzer. It can be summarized mathematically in the following relationship

$$h\nu = BE + KE + \Phi_{spec} \tag{2.7}$$

It states that the energy of the x-ray (hν) is equal to the binding energy (BE) of the electron (how tightly it is bound to the atom/orbital to which it is attached), plus

the kinetic energy (KE) of the electron that is emitted, plus the spectrometer work function (Φ_{spec}), a constant value. The latter is included because BE is measured with respect to the Fermi level, not the vacuum level. By rearranging this equation, it is possible to extract the binding energy. Photoelectron peaks are notated by the element and orbital from which they were ejected. Binding energy is a material property and it is independent from the source of x-rays employed. This technique relies on the fact that the chemical environment of an atom has a pronounced effect on the assessed binding energies of core-level electrons (*chemical shift*). The information is extracted by comparing the experimental binding energy to literature databases. [52]. To understand

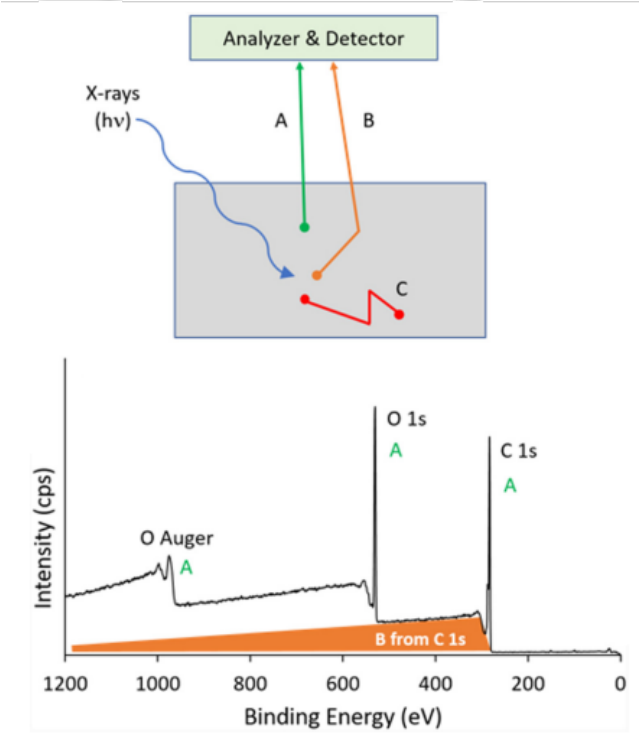

Figure 2.12: *Different ways of electron interaction with the sample are shown to be dependent on the depth at which they are generated. Electrons at the surface, labeled A, that produce XPS and Auger peaks, do not undergo any scattering. The ones generated closer to the surface and undergoing at least one inelastic collision are labeled B and contribute to the background (orange shaded area). Electrons that undergo multiple collisions and do not escape the sample are labeled C.*

why it is a surface-sensitive technique, it must be considered that x-rays that irradiate the sample can penetrate quite deeply (a few μm into the sample). Electrons, labeled C, generated this deep in the sample will undergo many inelastic collisions (collisions that involve the loss of energy) and eventually will lose all their energy before escaping

Technique	XPS
Information	Quantitative elemental analysis Chemical environment Binding Energy (BE)
Depth resolution	0.5-5nm
Spatial resolution	Spectroscopy: 1-40mm Imaging: 5mm
Sensitivity	0.1-1 atomic%

Table 2.5: *The table summarizes the possible information achievable by SEM, together with basic performance specifications.*

from the sample. On the other hand, electrons generated closer to the surface may only experience one or two inelastic collisions before escaping and reaching the detector (labeled B). Consequently, these electrons leave the sample with less kinetic energy than expected, as they have lost some energy randomly during their path to the detector. They contribute to the background signal's vertical step, which accompanies any significant peak. Only the electrons that escape the surface without any inelastic collisions (A) will contribute to the characteristic photoelectron peaks that we use in XPS analysis. The scheme in fig. 2.12 summarizes this concept.
For what concerns data analysis, an internal standard is used to correct the energy scale, allowing the comparison to other reference data. Almost all surfaces are characterized by the presence of carbon contamination, due to the exposure to the atmosphere, and the lowest binding energy C 1s peak (graphitic or CH_2 like carbon) is often employed. The energy of this peak ranges between 284.8 and 285 eV.

2.5 Time-of-Flight Secondary Ion Mass Spectrometry (ToF-SIMS)

Time-of-Flight Secondary Ion Mass Spectrometry (ToF-SIMS) is a surface-sensitive analytical method that uses a focused, pulsed ion beam (Cs or microfocused Ga) to produce secondary ions in a sputtering process (fig. 2.13). It is closely related to SIMS, which uses a constant beam of primary ions to etch a sputter crater into a sample over a period

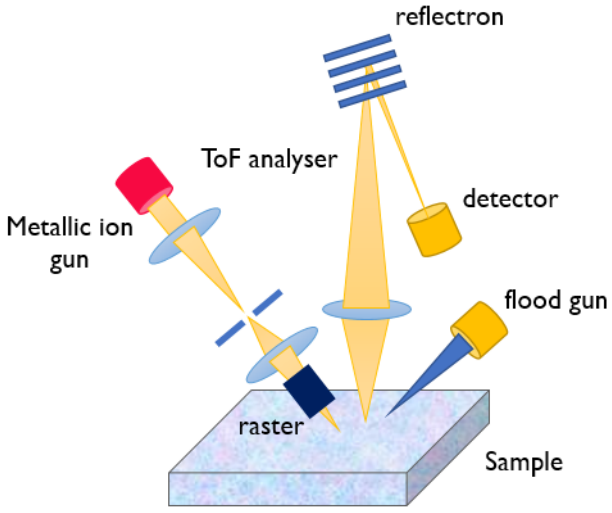

Figure 2.13: *Schematic representation of ToF-SIMS apparatus.*

of minutes. In contrast, ToF-SIMS uses a pulsed ion beam and does not significantly sputter etch or damage the sample surface on the timescale of the analysis. This lack of damage makes it an ideal technique for the analysis of surfaces for the presence of both elemental (most elements in the periodic table) and molecular species, with a very shallow sampling depth (1-2 nm). Analyzing these secondary ions allows identification of the atoms and molecules present on the surface of the particles, the absorbed molecules, and contaminants. In particular, this is possible by accelerating them into a flight tube and their mass is determined by measuring the time at which they reach the detector. ToF-SIMS can provide mass spectral information, image information in the xy plane across a sample, and also depth profile information on the z dimension into a sample if combined with ion sputtering (with either the same primary ion gun or using an additional Cs, O or Ar cluster ion beam). The primary beam can be focused to sub-μm dimension, meaning the technique can be used to analyze features in the 1 μm to 500 μm. Moreover, its surface sensitivity allows to detect species present at lower levels than traditional surface analysis techniques such as XPS and Auger [53].

2.6 Dislocation Sensitive Etching (DSE)

Dislocation Sensitive Etching (DSE) is related to the etching of different threading dislocation surface pits with different etch-rates and shapes. Dislocations are preferential sites for etching, due to the presence of locally high surface energy that makes etch pits favorable to initiate from that position. They are the result of the interaction between the dislocation stress field and the surface energy. Due to the correlation between

Technique	ToF-SIMS
Information	Elemental composition (layer by layer and quantitative)
Depth resolution	1-3μm
Spatial resolution	<0.1μm

Table 2.6: *The table summarizes the possible information achievable by ToF-SIMS, together with basic performance specifications.*

dislocations and etch pits, their observation has become a highly valuable method for investigating dislocations in crystals. This technique offers advantages such as low cost and a straightforward experimental procedure. Moreover, the etch pit observation method is frequently employed to quantify the dislocation density in crystals. In samples with high dislocation density, smaller etch pits are favored for accurately determining the overall dislocation density, as it is more challenging for small etch pits to merge. Conversely, in samples with low dislocation density, larger etch pits are preferred to differentiate between different types of dislocations. Additionally, the morphology of the etch pits allows for the distinction of the dislocation type [55]. This is due to different polarities and decoration types, resulting in a different reactivity with the etchant. It has been demonstrated that screw dislocations tend to etch more than mixed and edge dislocations. However, the variation in etch rate with respect to mixed type dislocations, and therefore the size of etch pits, might not always be significant enough to differentiate them effectively. Edge dislocations exhibit the smallest etch rate and are generally distinguishable by their characteristic geometric arrangement [56], [54].
For GaN, different etchants have been tested, like HCl, H_3PO_4/H_2SO_4 and molten KOH [57]. Lu et al. proposed an interpretation of the origin of etch pits. In particular, different shapes (labeled as α, β and γ) were distinguished by SEM, TEM and AFM. Their structure is displayed in fig. 2.14. It is believed that α pits are associated to pure screw dislocations, β to pure edge and γ to mixed ones [54].
In the present study, etching was performed through aqua regia and 30% diluted KOH. The level of safety of this substance had to be taken into account to determine the solution and the temperature. Different attempts were performed and the final recipe was to etch for 1 hour in aqua regia and for 40 minutes in KOH at a temperature between 90°-100°, reached with the help of a hot plate and monitored by a thermometer.

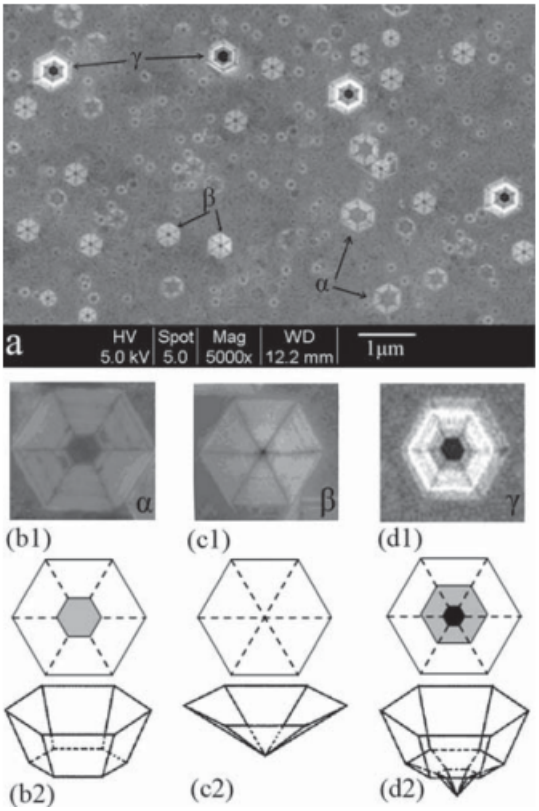

Figure 2.14: *(a) A typical SEM image of KOH etched GaN surface. (b1) α type, (c1) β type, and (d1) γ type etch pit are observed correspondingly. Two-dimensional and 3D schematic view of (b2) α type, (c2) β type, and (d2) γ type etch pit are demonstrated [54].*

Chapter 3

Results and discussion

Firstly, AFM images capturing surface topography were obtained for each sample (see fig. 3.1). These measurements were acquired by Bruker's Dimension Icon, using PPP-NCST (from NanoAndMore) tip probes. For topography measurements, both tapping and peak force modes were used. Scan rate was kept below 0.35 Hz for the given scan size in the work (25 μm^2). All the images were analyzed by Gwyddion software program, in order to remove the artefacts (such as data leveling, background subtraction, alignment of rows, correction of horizontal scars) and to process data from these maps. As shown for the reference sample (fig. 3.1(a)), numerous pits, attributed to dislocations terminating at the surface, can be easily identified. Indeed, different sizes and depths can be recognized: the smaller pits are also shallower, and the depth ranges from just 0.5 nm up to 1.5 nm for the bigger ones. The diameters range from 10 to 50 nm. In evaluating these values it's important to account for the radius of the tip, expected to be 8 nm if new. Notably, larger pits can be discerned, marked by white arrows in fig. 3.2,

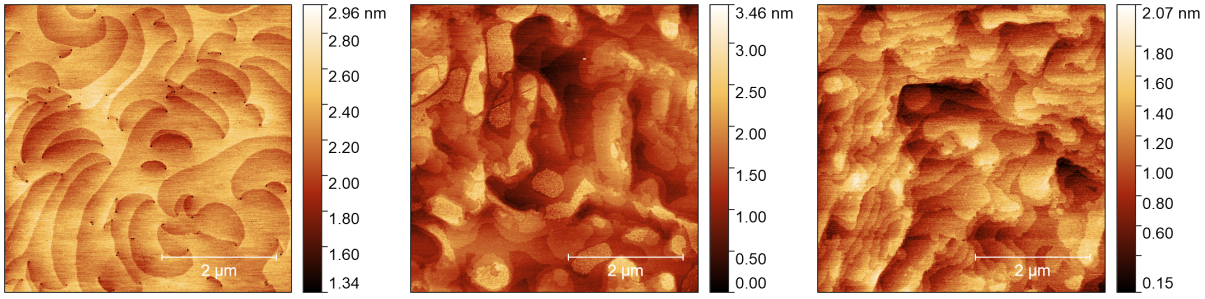

(a) **(b)** **(c)**

Figure 3.1: *Surface topography by AFM of (a) reference, (b) UID, and (c) ELOG sample.*

interacting with terraces and leading to their swirling. Therefore, they are dislocations with a screw component [58]. Additionally, another type of pits, which is much smaller

in dimensions and is often observed in close proximity to one another can be observed. Some of them are enclosed by yellow curves in fig. 3.2. As they don't interact with the terraces, they are expected to lack screw components and can be deduced as edge-type dislocations.

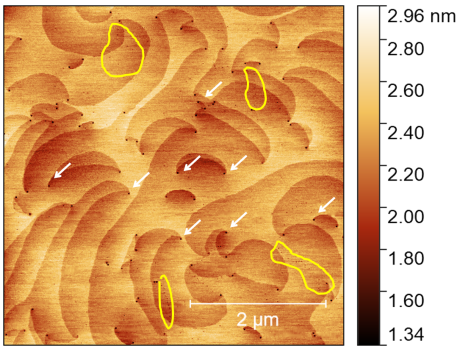

Figure 3.2: *Surface topography by AFM of reference samples. Yellow marks highlight edge dislocations, while white arrows are used for screw and mixed ones.*

Unfortunately, when the whole device's epitaxial stack is grown using either of the buffers, UID (fig. 3.1(b)) and ELOG (fig. 3.1(c)), the morphology is considerably complex, making the detection of dislocations using the morphology very challenging. Consequently, any attempt to estimate their density would likely result in an underestimation. In particular, sporadically distributed patches with much higher roughness and with higher height by 1 nm, were observed in the morphology of the UID sample (seen as brighter regions in fig. 3.3). The second section of this chapter will be devoted to elucidating their origin. To obtain a more accurate estimation of the dislocation density, a decision was made to employ chemical etching using aqua regia, a known solution for removing metallic contamination and gallium oxide [59], as well as 30% diluted KOH solution (at 90°) [57]. The results of these etching processes are depicted in fig. 3.5 and 3.6, respectively. While aqua regia treatment led to noticeable changes in the morphology of the UID sample and even removing the above-mentioned rough patches, it did not provide sufficient information for an accurate evaluation of the dislocation density. Similar limitations were encountered when examining the KOH-etched surface. Very interestingly, the formation of highly directional features was observed on the latter. The third section of this thesis will be related to the investigation of this phenomenon. However, in both cases, some bigger pits could be identified (with a diameter of up to 90 nm).
As previously mentioned, the results will be divided into three main sections:

- optoelectric characterization of dislocations
- investigation of anomalous morphological features for UID case
- anisotropic step formation during KOH etching

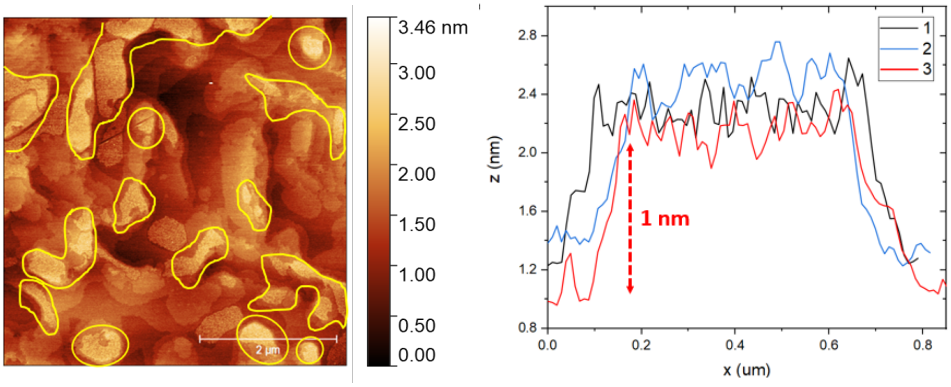

(a) **(b)**

Figure 3.3: *(a) UID sample topography by AFM. Yellow marks indicate higher regions on the surface. (b) Line profile across three of the yellow-marked regions.*

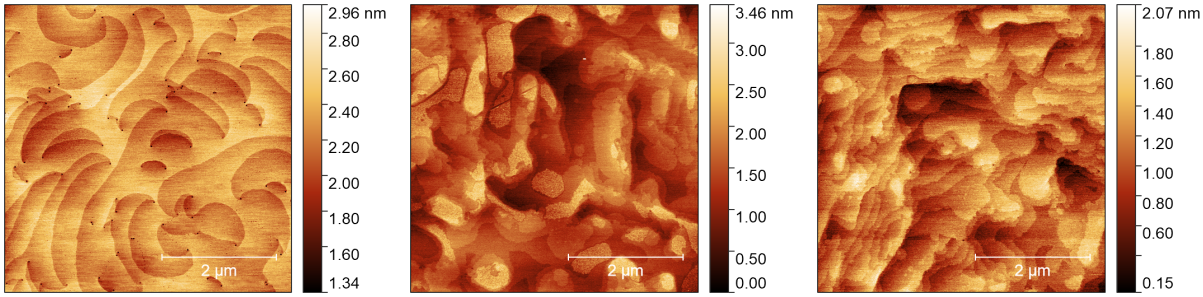

(a) **(b)** **(c)**

As grown

Figure 3.4: *Surface topography by AFM of (a) reference, (b) UID and (c) ELOG samples.*

3.1 Optoelectric characterization of dislocations

3.1.1 Scanning Electron Microscopy (SEM)

To obtain a reliable estimation of the dislocation density, it was decided to employ Cathodoluminescence (CL) and Electron Channeling Contrast Imaging (ECCI). An area of $\sim$42 μm^2 was investigated. The resolution was maximized by selecting 5 kV as beam energy and 0.80 nA as beam current. From the images shown in fig. 3.7, it is evident that the UID sample exhibits a more significant number of darker spots in the CL map and of black/white contrast regions in the ECCI image. The final results of dislocation density by CL, ECCI, and AFM are summarized in table 3.1. It is clear that CL provides the best characterization in terms of color contrast and sensitivity to dislocations, while

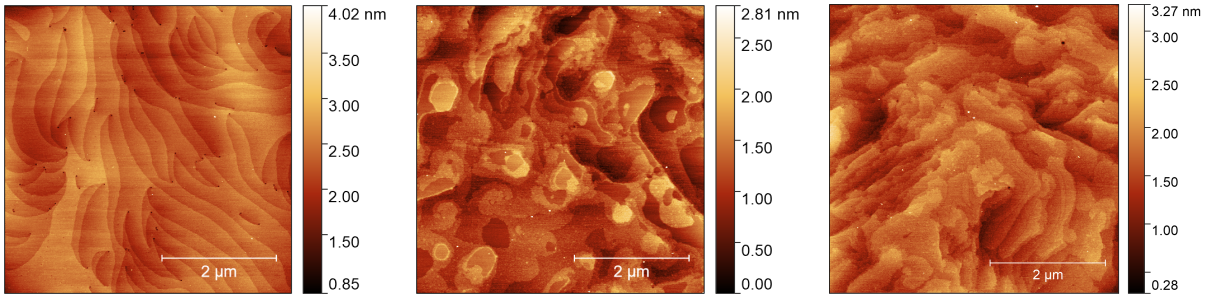

(a) **(b)** **(c)**

Aqua regia

Figure 3.5: *Surface topography of (a) reference, (b) UID, and (c) ELOG sample after aqua regia etching.*

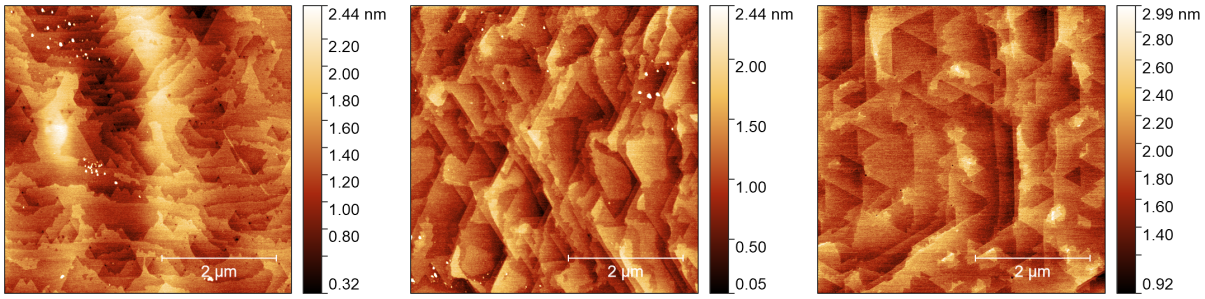

(a) **(b)** **(c)**

KOH

Figure 3.6: *Surface topography of (a) reference, (b) UID, and (c) ELOG sample after KOH etching.*

the lower amount detected from ECCI is only due to the poor resolution that does not allow to resolve the smallest pits. The different values must be addressed to the fact that these techniques detect dislocations by considering different output signals. While AFM probes the morphology, CL measures the luminescence and ECCI monitors the behavior of backscattered electrons. In particular, the lower density for the UID sample found by AFM must be probably addressed to the complex morphology, also due to the presence of additional features on the surface.

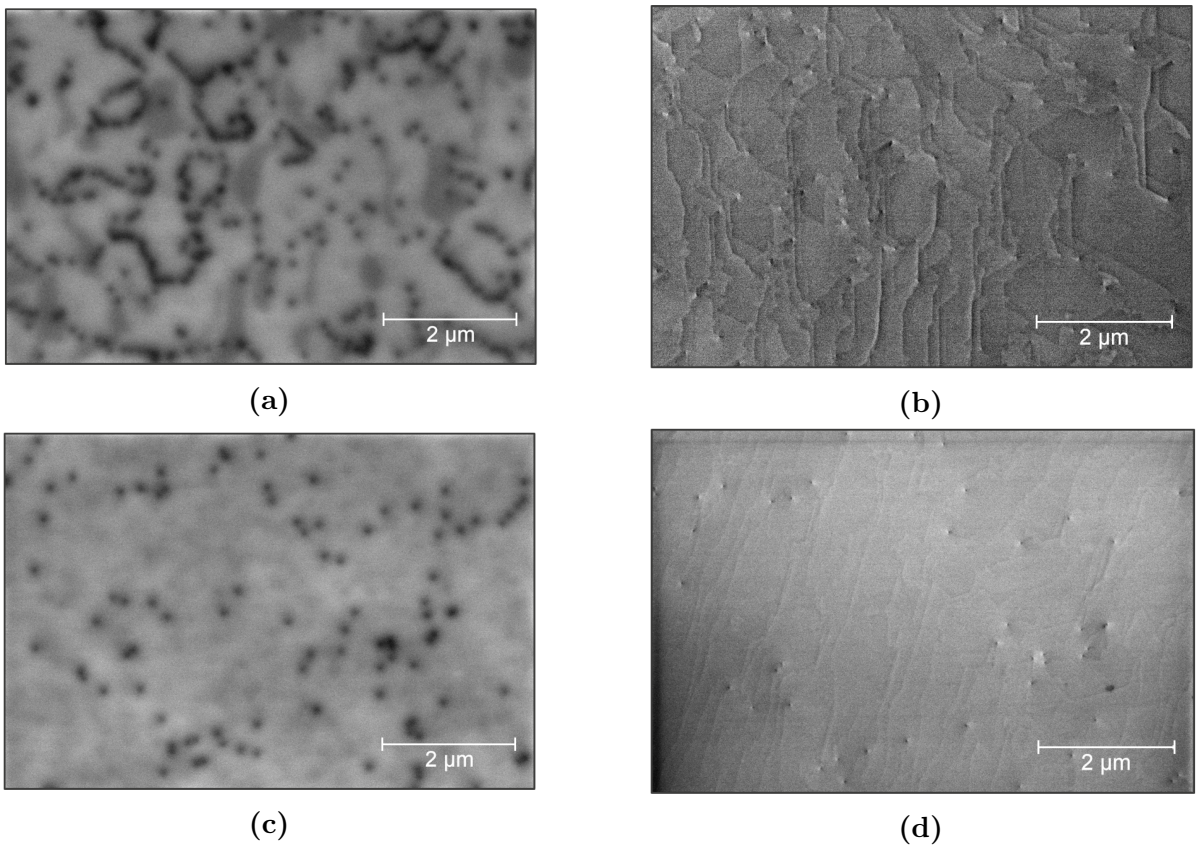

Figure 3.7: *CL (a,c) and ECCI (b,d) maps of UID and ELOG buffer samples, respectively, acquired with a beam energy of 5 kV and a beam current of 0.80 nA.*

	Dislocation density ***(10^8 cm^{-2})***		
	CL	**ECCI**	**AFM**
UID	6.1±0.5	1.3±0.3	0.5±0.1
ELOG	2.0±0.1	1.0±0.04	0.8±0.2
Reference	7.8±0.1	0.8±0.1	8.1±0.2

Table 3.1: *Table summarizes the dislocation density achieved by CL, ECCI, and AFM techniques from the three samples.*

3.1.2 Scanning Capacitance Microscopy (SCM)

Optimization of SCM imaging condition: Plan-view measurements

Scanning Capacitance Microscopy (SCM) measurements were performed on Bruker's Dimension Icon. Pt/Ir coated PPP-NCSTPT conductive tips were employed. Still, it was necessary to optimize the imaging condition in order to get a reliable result, as shown in the following.
Firstly, maps were acquired by Bruker's Dimension Icon and compared to the ones by Park NX10 on the same sample. Indeed, the latter had been used several times for this

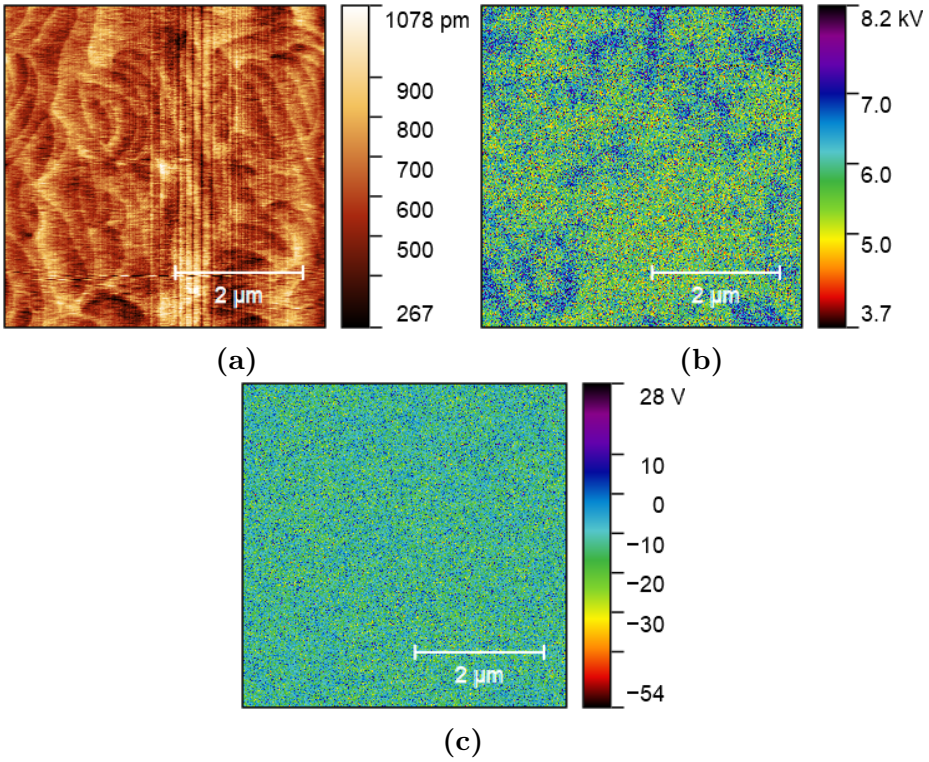

Figure 3.8: *The image shows (a) topography and SCM (b) amplitude and (c) phase maps from reference sample surface by Bruker's Dimension Icon. AC bias of 1.2 V and DC bias of -1.5 V.*

kind of measurement. For the first, an AC bias of 1.2 V and a DC of -1.5 V were applied, while for the second the AC bias was set to 3 V and the DC was the same. As can be noticed from the comparison of the maps achieved by Bruker's Dimension Icon (fig. 3.8) and Park NX10 (fig. 3.9) on the reference sample surface, the first result is not reliable: it does not manage to provide correct information about reduced signal regions due to dislocations. Besides, the phase, which should be around -90°, indicating an n-doped

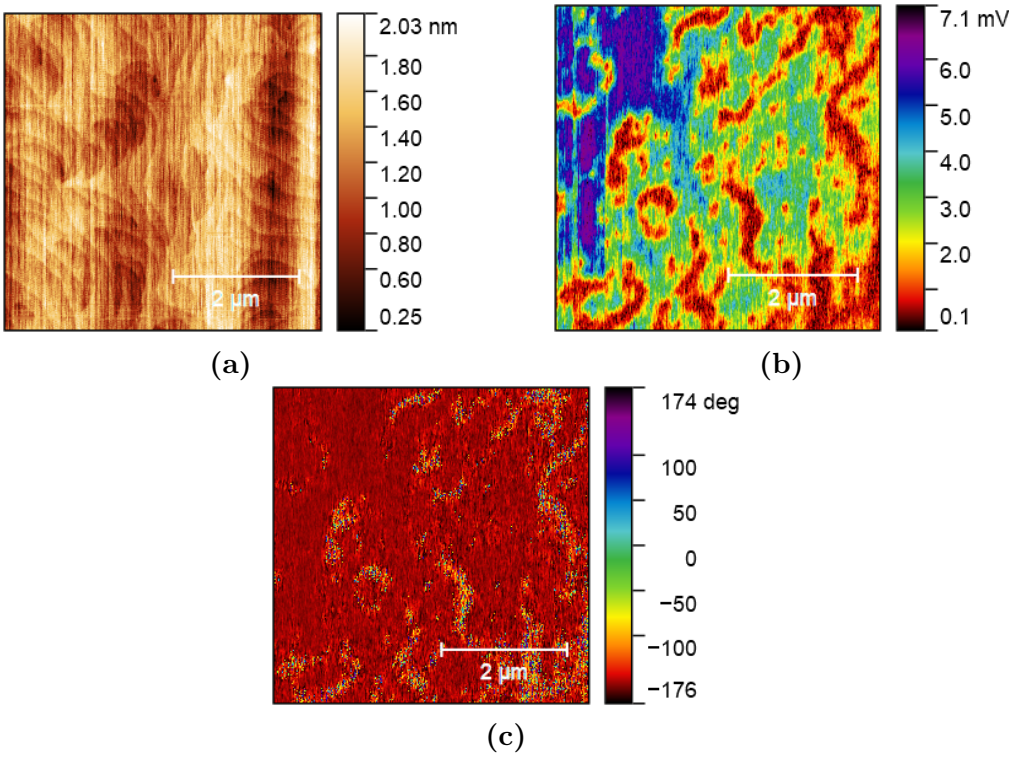

Figure 3.9: *The image (a) topography and SCM (b) amplitude and (c) phase maps from reference sample surface by Park NX10. AC bias of 3 V and DC bias of -1.5 V.*

layer, is closer to zero. The different responses should be related to the RF capacitance sensor, characterized by a wider RF bandwidth for Park NX10, allowing the selection of the most sensitive frequency of the resonator.

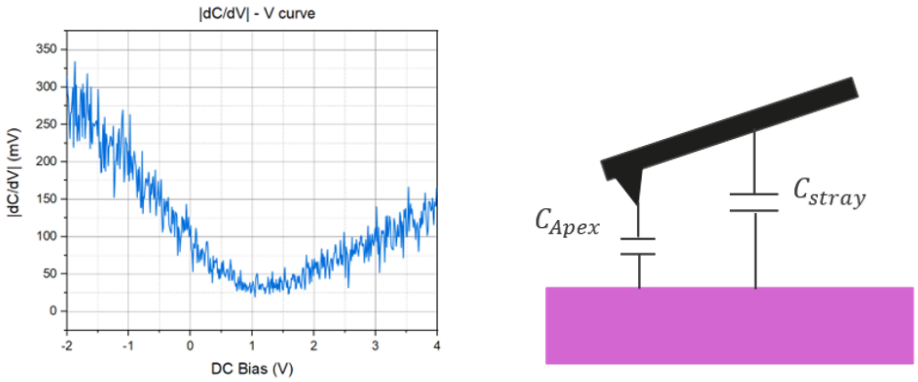

(a) **(b)**

Figure 3.10: *(a) Scanning Capacitance Spectroscopy performed on one point of the reference sample surface, showing the artifact at positive bias. (b) Representation of parasitic capacitance between the sample and the cantilever, affecting the measurement.*

However, our aim was to find a way to reproduce the same measurement by Bruker. By performing spectroscopy on the sample, an artifact in the SCM signal was observed as a function of the DC bias. Specifically, a linear increase was detected at positive bias (as shown in fig. 3.10 (a)), which is likely linked to the lower resolution. This observation led to the idea that the signal might be influenced by parasitic capacitance between the surface and the cantilever, masking the true behavior. A scheme showing them is presented in fig. 3.10 (b). Consequently, to mitigate this impact, measurements were carried out at the sample's edge, keeping the same DC and AC bias.

Maps acquired at the edge display the correct outcome, and the resolution appears significantly enhanced, close to the one attained by Park NX10 (see fig. 3.11).

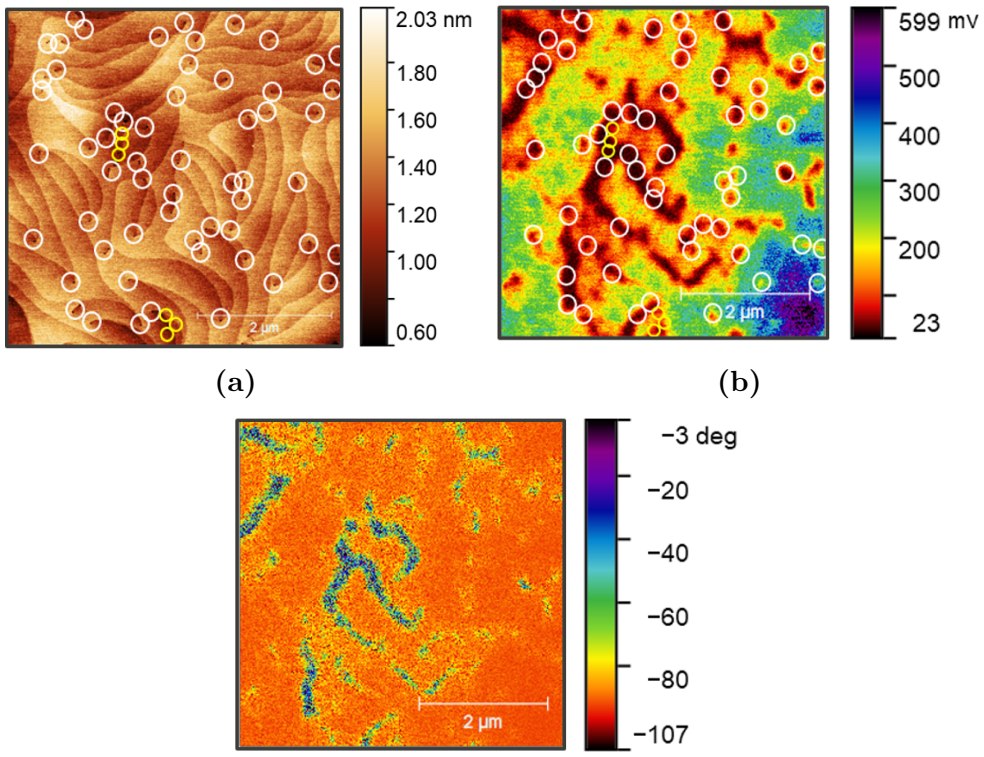

Figure 3.11: *The image shows the (a) topography and SCM (b) amplitude and (c) phase maps from the reference sample surface by Bruker's Dimension Icon, by measuring at the edge.*

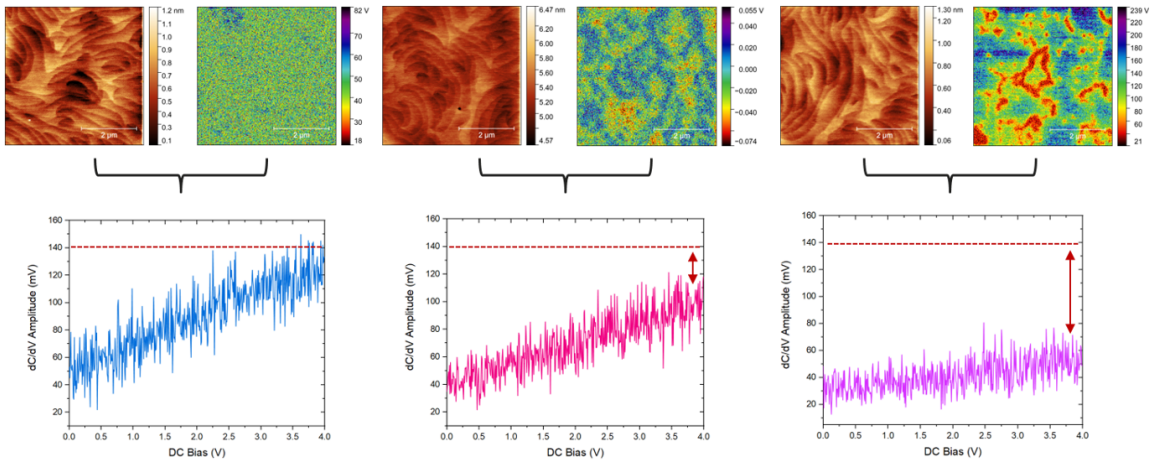

(a) Pt/Ir (3.2 N/m)

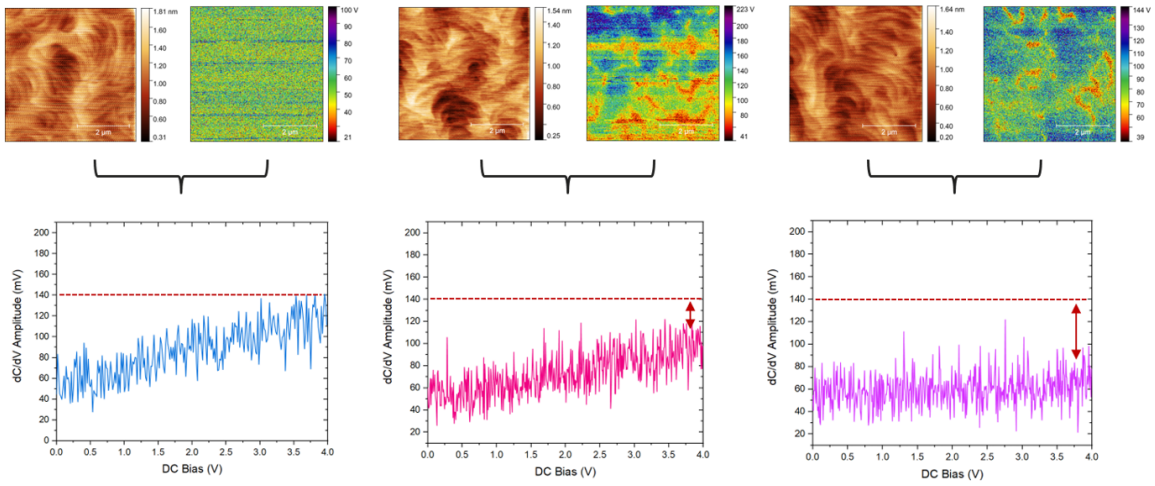

(b) Diamond (20.7 N/m)

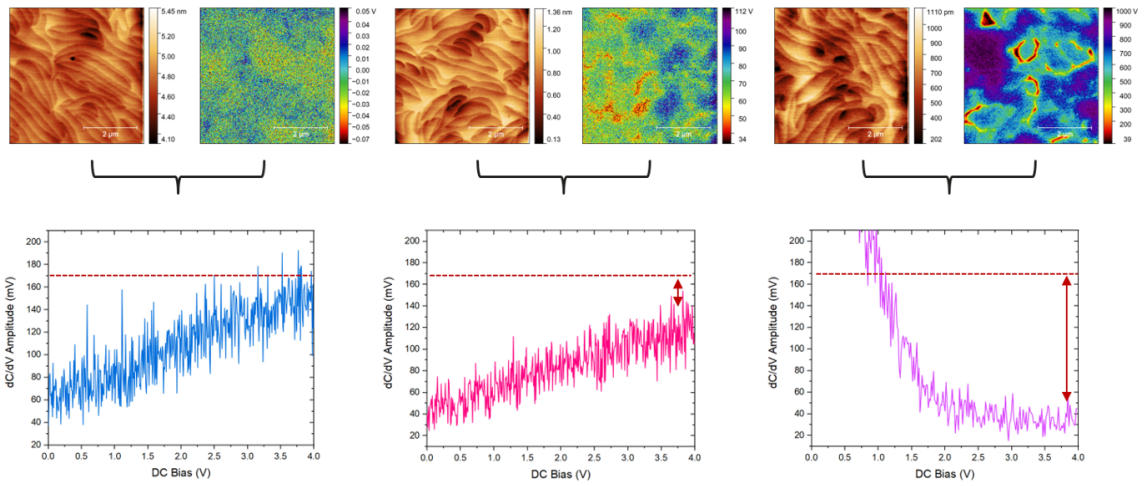

(c) Adama (106.9 N/m)

Figure 3.14: *Topography and SCM maps measured from the center to the edge (from left to right). Below, the spectroscopy at positive bias on the same area. Measurements were performed by using (a) Pt/Ir, (b) diamond, (c) Adama tip.*

Another way to decrease the impact of stray capacitance could be the use of tips characterized by higher stiffness. Indeed, the oscillation due to stray capacitance can be reduced in this way. In order to define the best procedure to achieve good measurements and to assess the impact of each factor on the final resolution, measurements were conducted from the center to the edge with tips of different stiffness.

In particular, measurements were conducted by Pt/Ir (3.2 N/m), diamond (20.7 N/m), and Adama tips (106.9 N/m). Sensitivity and elastic constant calibration were performed for each one, directly on GaN thanks to its hardness.
By comparing the acquired images, displayed in fig. 3.14, it is possible to notice that measuring at the edge is fundamental to get a reliable map, independently from tip stiffness, and that this is related to the flattening of the artifact at positive bias. However, the employment of a higher stiffness tip can enhance the quality of the image, as shown by the line profile across lower signal regions in the map at the edge. The comparison between Pt/Ir and Adama in fig. 3.15 displays clearly that for the second the contrast is more pronounced.

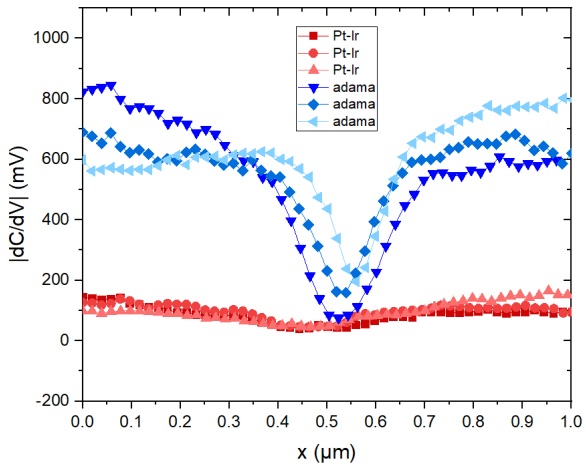

Figure 3.15: *Line profile across lower signal regions from the maps acquired at the edge of reference sample by Pt/Ir and Adama tips.*

Surface study

Firstly, the surface of reference, UID, and ELOG samples was investigated by SCM, by applying 1.2 V as AC bias and -1.5 V as DC one. Figure 3.16 shows topography (a) and |dC/dV| (b) maps acquired on the reference sample. White circles mark screw and mixed dislocations, while yellow circles are used for edge ones. A very good correspondence between dislocation pits and the lower SCM signal appears in the map on the right. This can be explained by considering dislocations as acceptors. Negatively charged dislocations are a source of band bending at their site (fig. 3.17). This determines the presence of a positive space region (depletion region of electrons). The capacitance formed by the depletion region of the dislocations adds to the tip-sample junction capacitance in series, thereby reducing the net capacitance and consequently, the |dC/dV|. This result is in good agreement with what was found in the past by Minj

et al. on a similar sample [47].

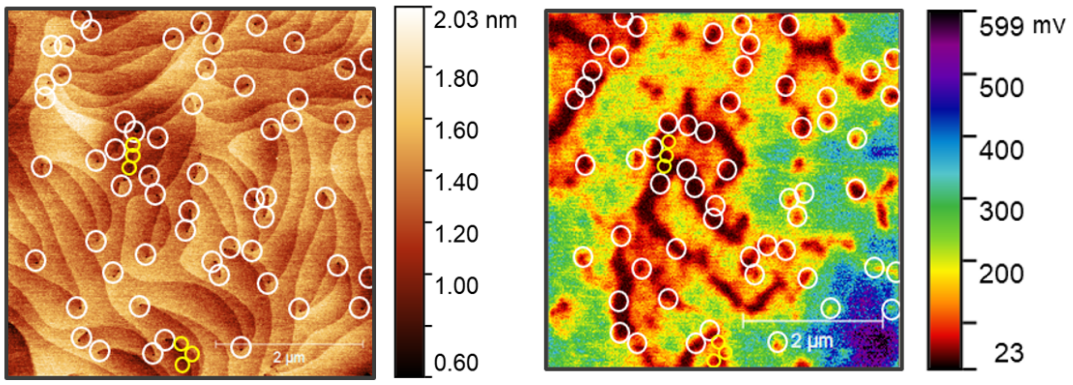

(a) **(b)**

Figure 3.16: *(a) Surface topography of reference sample. White circles mark screw and mixed dislocations, and yellow circles are related to edge ones. (b) $|dC/dV|$ map of same area.*

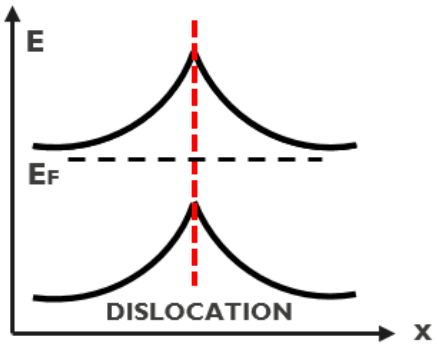

Figure 3.17: *Band bending at negatively charged dislocation site.*

By conducting spectroscopy on white and yellow marked areas, it was observed that these regions (red, and blue curves) require a larger forward bias compared to the background (black curve), as shown in fig. 3.18 (b).

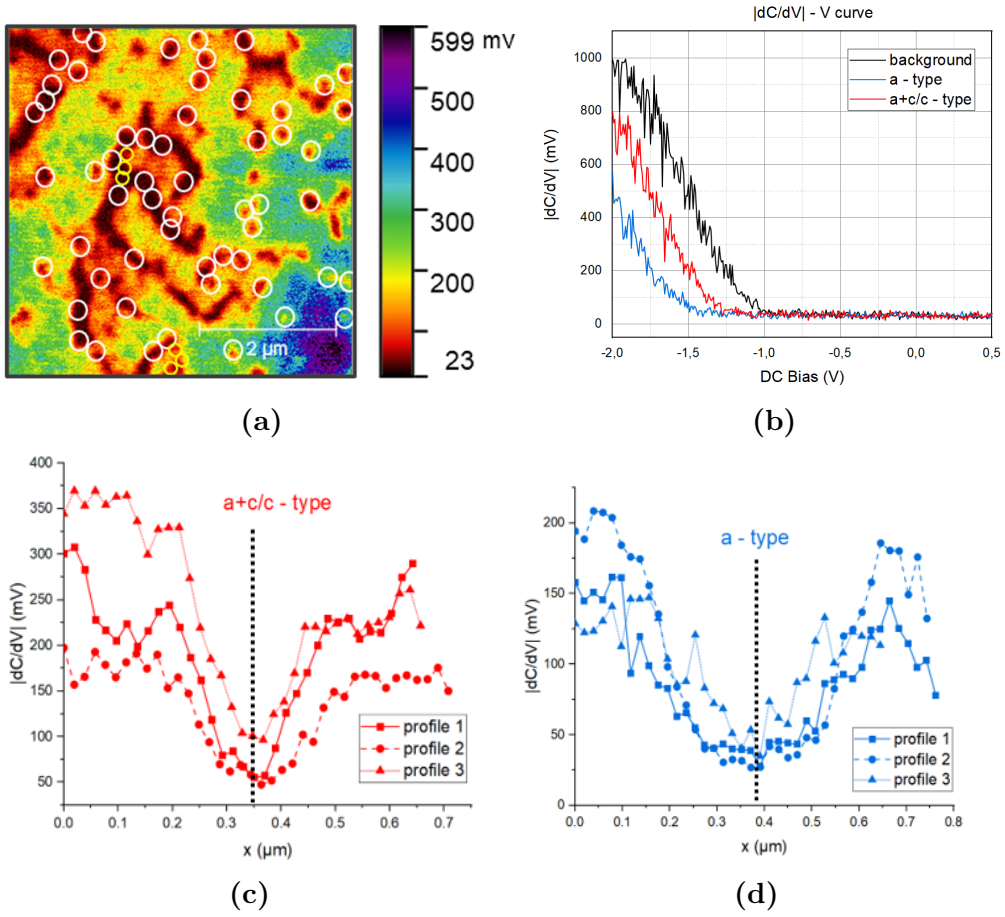

Figure 3.18: *(a) SCM map acquired on the reference sample. (b) Spectroscopy performed on screw, mixed (red), edge (blue) dislocations, and at the background (black). Line profiles acquired at white and yellow circles, indicating mixed/screw (c) and edge (d) dislocations on the topography, respectively.*

This finding aligns well with the presence of a larger depletion region at their respective locations. Additionally, the red curve corresponds to mixed and screw dislocations, whereas the blue curve represents measurements taken on edge pits. On average, it was found a difference of 0.3 V between the threshold voltage associated with the background and with the screw/mixed dislocation curve, while it was 0.5 V for the edge ones. Therefore, the latter appears to necessitate a higher voltage, indicating the presence of a larger depletion region. This observation is further supported by comparing the line profiles in fig. 3.18, which shows lower values of minima at edge dislocations (25 instead of 50 mV found at screw/mixed). This is a signature of the different electrical behavior of dislocation types, already observed by Minj et al. Several computational investigations have demonstrated that their electronic properties in terms of the local density of states

are closely related to the structural configuration of their core [60], [61].
The same measurements were conducted on UID and ELOG sample surfaces. It is possible to notice also in this case the presence of contrast, with some spots at higher signal with respect to the background (see fig. 3.19). For the ELOG sample, which exhibits

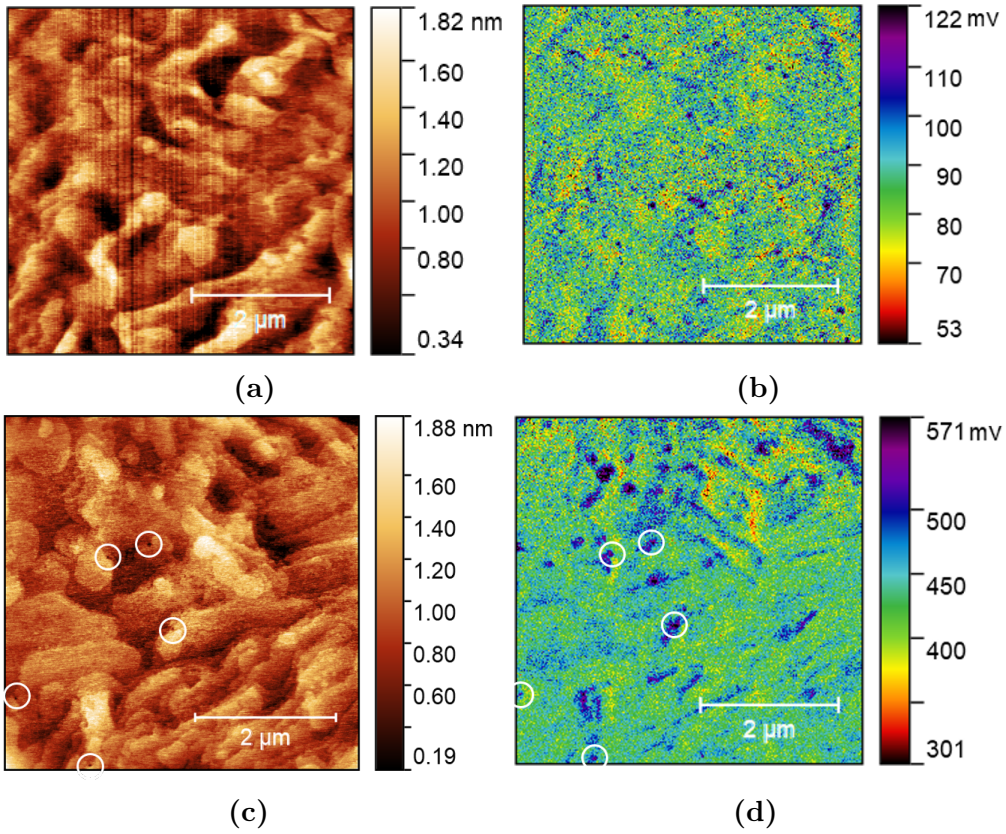

Figure 3.19: *(a) Topography and (b) |dC/dV| map of UID sample. (c) Topography and (d) |dC/dV| maps of ELOG sample.*

a simpler morphology, a correlation was found between dislocation pits and these spots (as evidenced by white circles), suggesting that they are consistently associated with these defects. Spectroscopy analysis in fig. 3.20 (a,b) confirmed that these spots behave differently from the background, showing a slightly larger signal. This difference is also evident from the line profiles (fig. 3.20 (c,d)).
The higher signal observed at dislocation sites of UID and ELOG samples contrasts with the results obtained from the reference sample, where dislocation pits are linked to a lower SCM signal. This can be explained by considering the non-monotonic behavior of |dC/dV| with electronic density. Numerical calculations by Giannazzo et al. [62] demonstrate that |dC/dV| decreases monotonically as the carrier density exceeds a threshold value, found around 10^{16} cm^{-3}, but increases before reaching that point

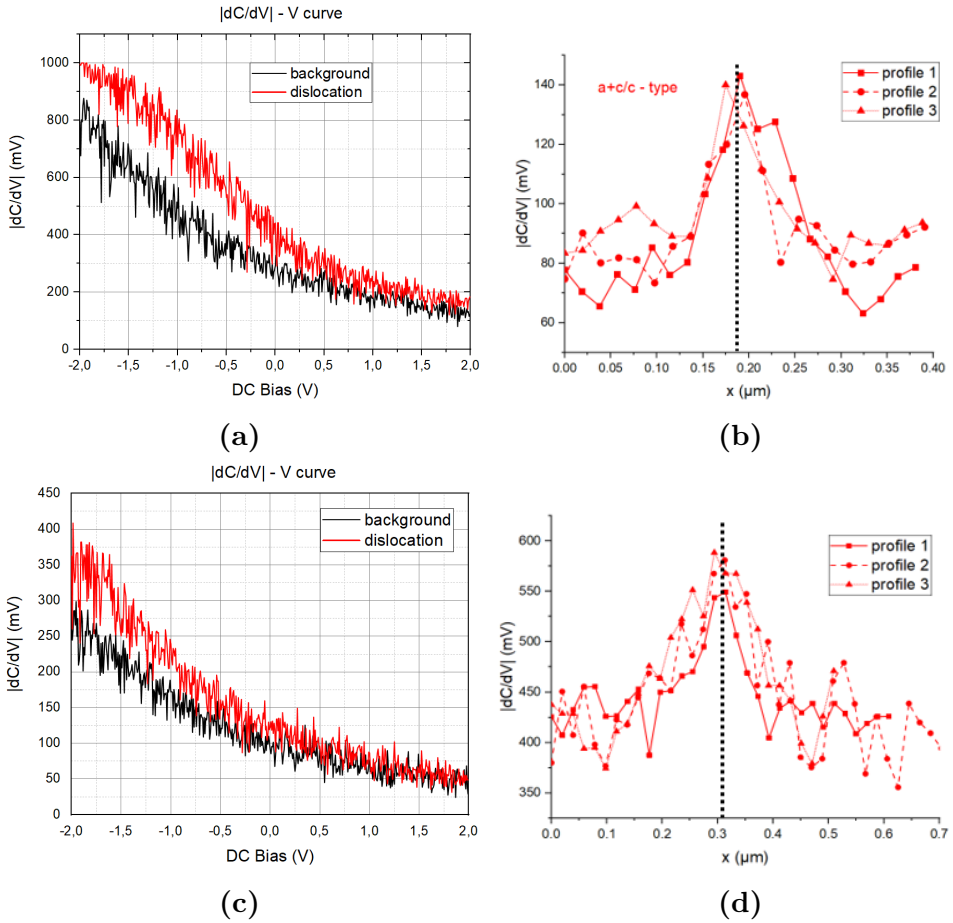

Figure 3.20: *(a) Spectroscopy in correspondence of higher signal spots (red) and background (black) on UID sample. (b) Line profile across higher signal spots on UID sample. (b) Spectroscopy across higher signal spots (red) and on the background (black) on ELOG sample. (d) Same line profile for ELOG sample.*

(fig. 3.21). It is important to note that the reference sample has a drift layer on top with a carrier density of 10^{16} cm^{-3}, while the other samples have a highly doped layer with a density of 10^{18} cm^{-3}. Dislocations always correspond to a lower carrier density, but the opposite trend is due to the different types of doping present at the two surfaces.

Cross-sectional study

Figure 3.22 and 3.23 show an overview of the SCM cross-sectional analysis on UID and ELOG samples. In this way, it was possible to map the drift layer and the electrical properties of dislocations across it. To achieve this, cleaving was performed along the

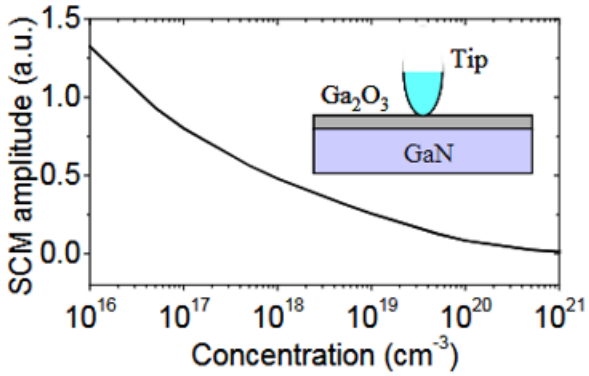

Figure 3.21: *Giannazzo et al. [62] simulation of SCM signal behavior as a function of carrier concentration.*

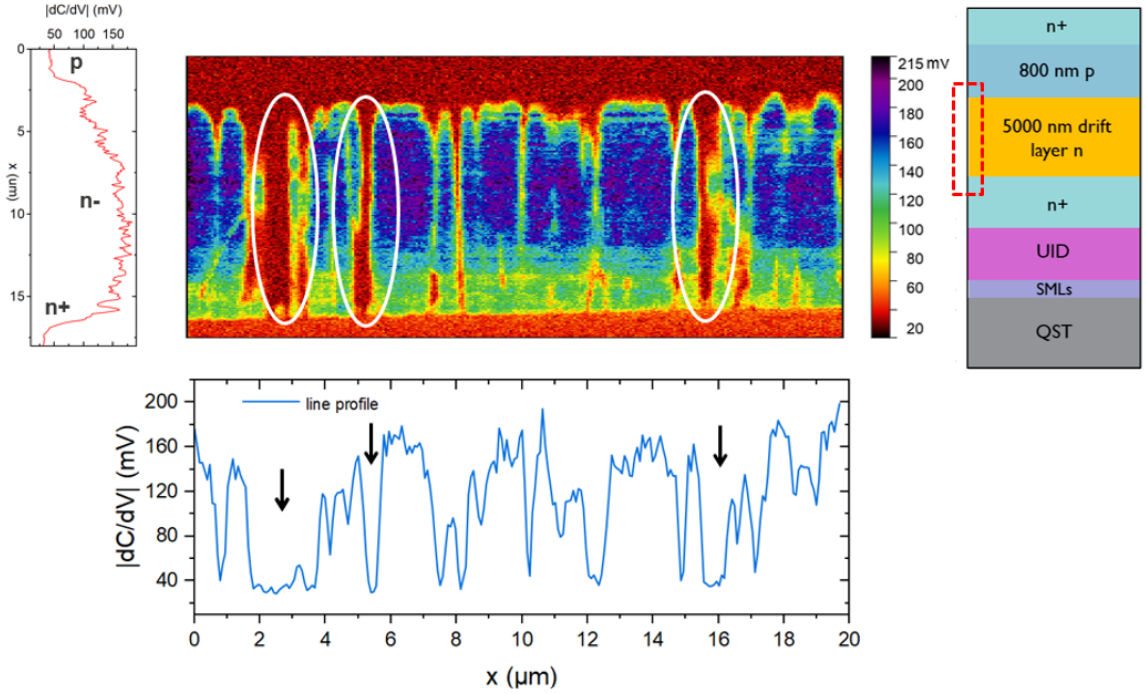

Figure 3.22: *The image shows the cross-sectional map of the UID sample, acquired across the drift layer, as shown from the vertical line profile on the left and by schematics on the right. White circles mark lower SCM signal regions, associated with dislocations. The line profile below displays the drop of the signal, with the black arrows marking it.*

plane (11-20), in ambient conditions. This method allows us to get insights into the drift layer while also dealing with fully fabricated devices. Several regions were investigated

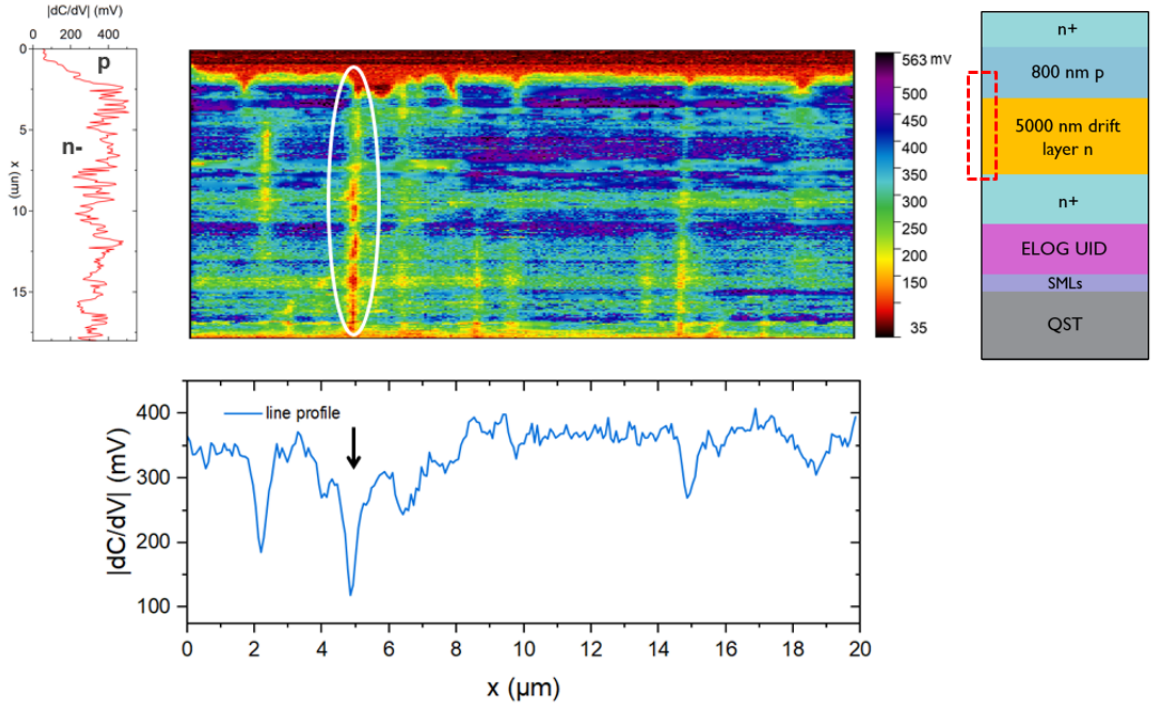

Figure 3.23: *The image shows the cross-sectional map of the ELOG sample, acquired across the drift layer, as shown from the vertical line profile on the left and by schematics on the right. White circles mark lower SCM signal regions, associated with dislocations. The line profile below displays the drop of the signal, with the black arrow marking it.*

with Pt/Ir coated and diamond tips. The maps were acquired by applying an AC bias of 1.2 V, coupled with a DC one of -1.5 V. It is possible to notice that the drift layer shows a higher SCM signal with respect to p and n+ ones, as expected by the lower doping level. Indeed, as described in the work by Giannazzo et al., |dC/dV| monotonously decreases with the carrier density exceeding 10^{16} cm^{-3}.

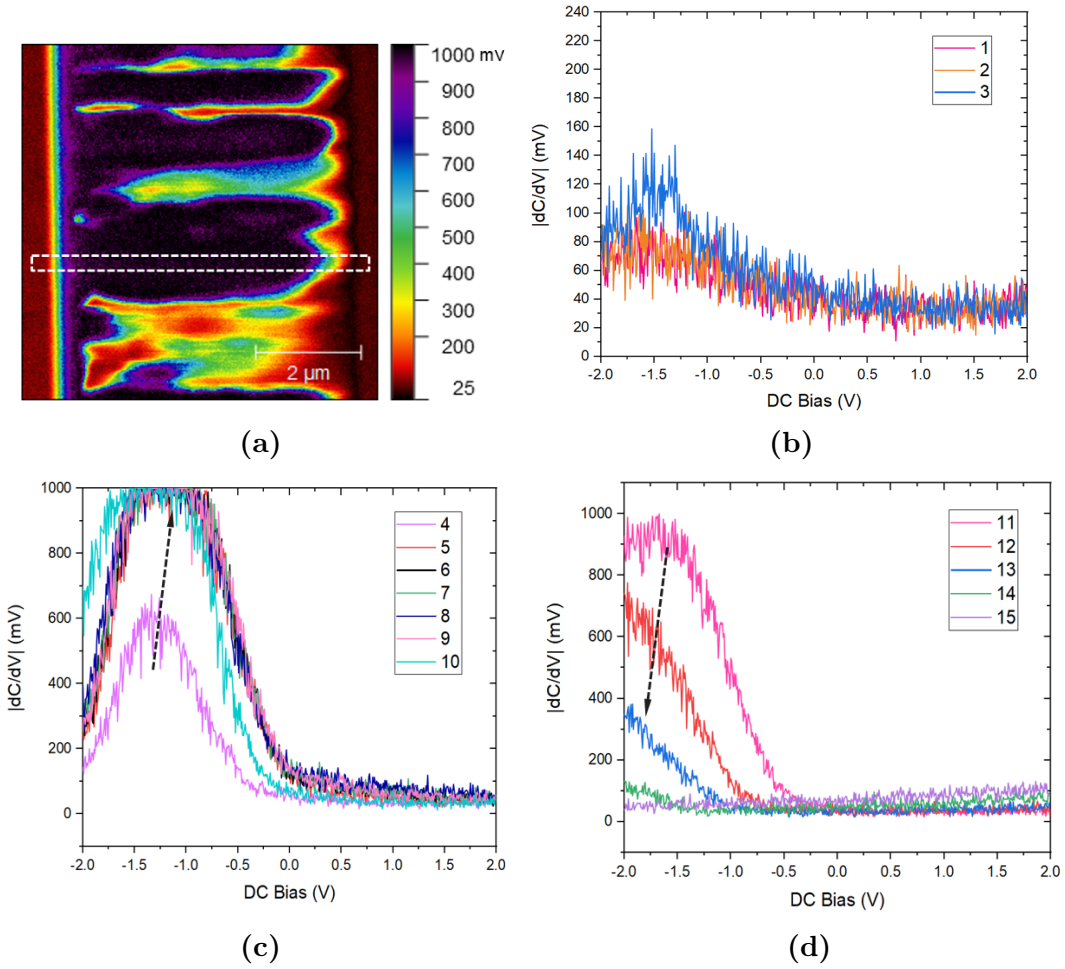

Figure 3.24: *(a) Cross-sectional map of UID sample drift layer. The region investigated by spectroscopy is marked. |dC/dV| spectroscopies at discrete positions (a) 1-3, (b) 4-10, (c) 11-15.*

Along the drift layer, the SCM distribution is not uniform but skewed-funnel-type local features are characterized by a significant drop of the signal. It was verified, from the simultaneously acquired topography maps, that the contrast seen in the SCM map had no correspondence with local morphological changes. As for the reference sample surface, they could be attributed to threading dislocations, that behave as acceptors, causing the formation of positive space charge regions around them. Near the p-n junction, the contrast formation results from the conjunction of space charge regions of the p-n junction and around the dislocation, which is seen as a skewed-funnel-type shape. Equivalently, this region around dislocations can be also interpreted as fully depleted i.e., with negligible electron density, and therefore, it would result in a |dC/dV| signal close to the noise level.

The |dC/dV| spectroscopy was performed over multiple points along the p-n junction (fig. 3.24 (a)), in a region free from dislocations. 1-3 curves (fig. 3.24 (b)), acquired at n+ layer, show an initial small magnitude for negative bias. 4-9 (fig. 3.24 (c)), achieved along the drift layer, are characterized by an increasing magnitude and a progressive overlap, a signature of homogeneity of electronic density along the growth direction. Peak formation is due to high-frequency capacitance-voltage relation, between the metallic Pt/Ir tip and GaN. By approaching the p-n junction (10-15, fig. 3.24 (d)) peaks shift and drop, while another component starts to appear at positive bias, which indicates that the net capacitance is influenced by the space charge region in the p-layer. By acquiring the

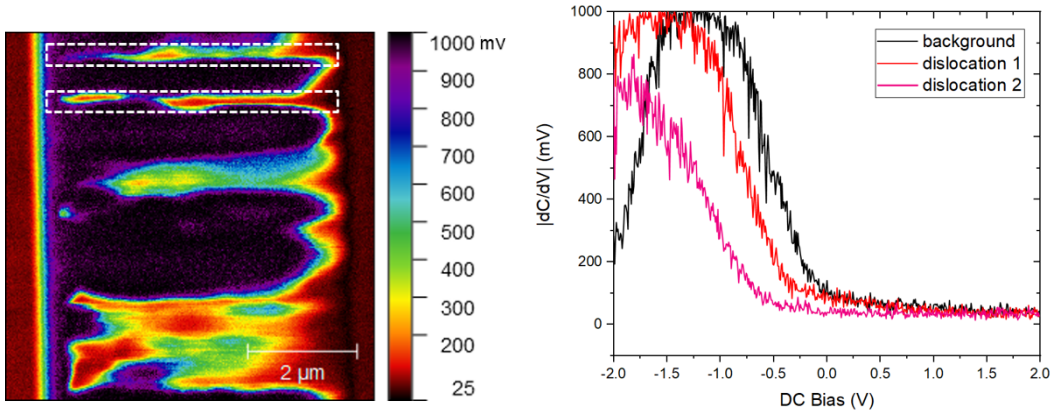

Figure 3.25: *(a) Cross-sectional map of UID sample drift layer. Dislocations investigated by spectroscopy measurements are marked. (b) |dC/dV| spectroscopy performed on dislocations (red, pink) and background (black).*

spectroscopy at the site of dislocations (fig.3.25), it is possible to notice a completely different behavior. The overlap due to the homogeneity of electronic distribution is no longer present and peaks are smaller and shifted towards higher forward bias, meaning that the electronic density is lower and the depletion region is larger.

3.1.3 Conductive Atomic Force Microscopy (C-AFM)

C-AFM analysis was conducted on both UID and ELOG samples, by using Pt/Ir and diamond tips. To visualize the expected leakage spots resulting from dislocations, it was necessary to access the p-type layer by removing the n+ layer. This was achieved by bevelling the epitaxial stack via mechanical polishing (fig. 3.26).

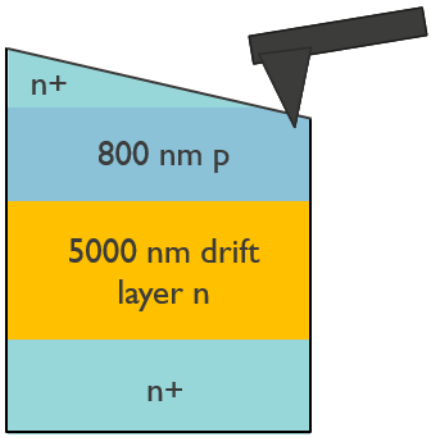

Figure 3.26: *Scheme of the beveled sample achieved by polishing.*

This was because the conductive n+-type layer would obstruct the observation of any leakage paths. In the case of the ELOG sample, a combination of polishing and KOH etching was necessary to eliminate non-conductive polishing lines that could potentially impact the measurements. For both samples, it was determined that the most effective approach to probe the leakages was by applying a reverse bias in the range between -8 and -10 V to the p-layer. The TUNA current amplifier was selected, providing a range of $\pm$ 245 pA. From the current maps obtained from 20×20 μm^2 regions (fig. 3.27, 3.28 (b)), the presence of spots with higher current levels, reaching up to 200 pA, can be observed. Spectroscopy, as shown in fig. 3.27, 3.28 (c), was conducted at various points on the leakage spots (represented by red, green, and blue curves) as well as on the background (represented by the black curve), by applying bias in a range between -9 and 5 V. It was

UID	V_t
spot 1	-4.8 $\pm$ 0.2
spot 2	-5.5 $\pm$ 0.8
spot 3	-5.2 $\pm$ 0.3

ELOG	V_t
spot 1	-3.6 $\pm$ 0.8
spot 2	-6.4 $\pm$ 0.2
spot 3	-8.0 $\pm$ 1.2

Table 3.2: *Threshold voltage at the three leakage spots on the surface of UID (left) and ELOG (right) sample.*

consistently observed that the leakage spots exhibited current flowing from a threshold voltage, ranging between -3 and -8 V, differently from the background displaying no measurable current. Threshold voltage values are summarized in table 3.2. Multiple

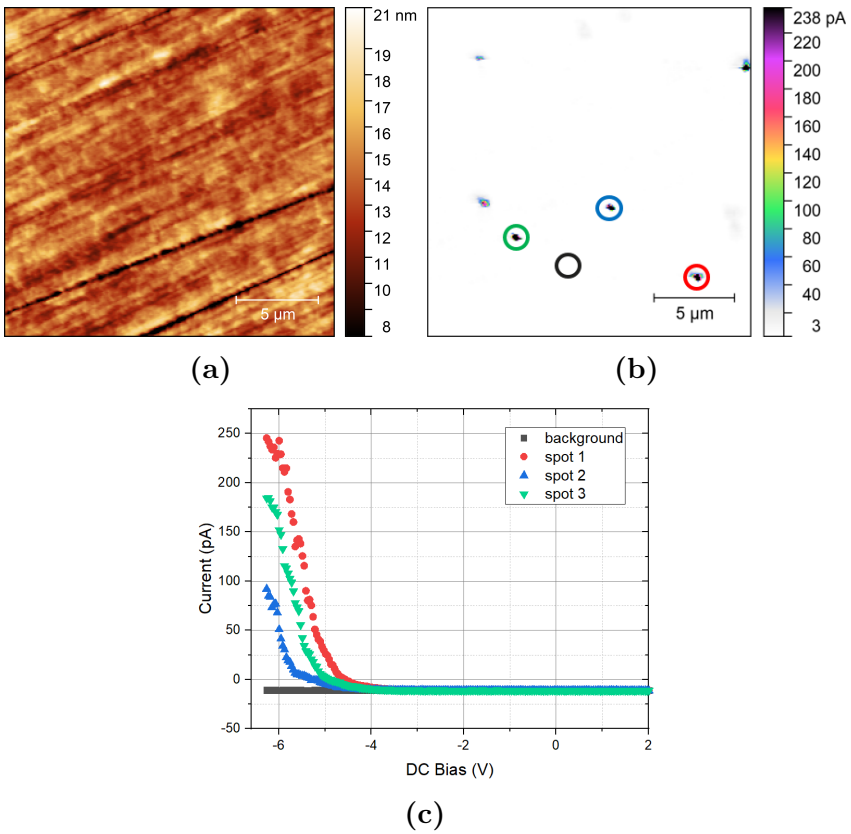

Figure 3.27: *(a) Topography and (b) current maps (20×20 μm^2) oF UID sample. Leakage spots are marked by red, green, and blue circles. (c) I-V curves acquired on marked spots and on the background (black circle).*

regions were measured, and the average leakage spot density was estimated by analyzing nine different images. The results are summarized in table 3.3. As for dislocations, in

	leakage spot density (cm^{-2})
UID	$(1.0\pm0.2)\times10^6$
ELOG	$(5.0\pm0.1)\times10^5$

Table 3.3: *Leakage spot density of UID and ELOG sample averaged over an area of 9×400 μm^2.*

this case UID sample shows a slightly higher leakage spot density. Comparing this with

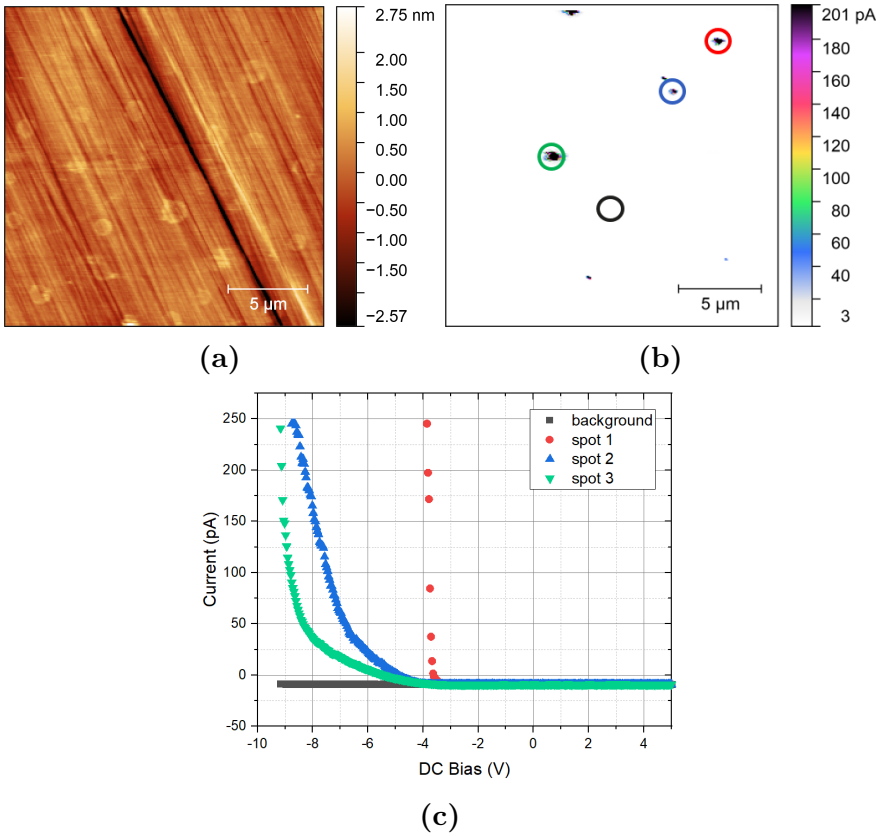

Figure 3.28: *(a) Topography and (b) current maps (20×20 µm²) on ELOG sample. Leakage spots are marked by red, green, and blue circles. (c) I-V curves acquired on marked spots and on the background (black circle).*

the dislocation density, it can be concluded that around 1% of the dislocations appear to be conductive. However, it cannot be ruled out that other dislocations may become conductive at higher voltages. Nevertheless, it is expected that the dislocations conductive at lower voltages are the most detrimental to the devices. This percentage provides support for the hypothesis that purely screw dislocations are the electrically active ones [63].

Modeling of I-V curves

Local current-voltage characteristics were acquired by C-AFM at the conductive dislocation site of UID sample, for a better understanding of the conduction mechanism. Measurements were repeated in different positions of dislocations. Eight curves were selected and an average was performed on them. Pt/Ir tip of C-AFM and the sample can be considered as a metal-semiconductor junction. In order to get insight into the type of transport, the Schottky Emission, the Fowler-Nordheim tunneling, the Poole-Frenkel

emission and the hopping conduction models were fitted on the acquired current-voltage curves. The electric field was estimated as the maximum electric field concentration, E_m, at the Schottky interface

$$E_m = \sqrt{\frac{2qN_d}{\epsilon_0 \epsilon_r}(\psi_{bi} - V - \frac{kT}{q})} \tag{3.1}$$

where ψ_{bi} was roughly calculated to be 1.9 eV. As shown by fig. 3.29, the Variable

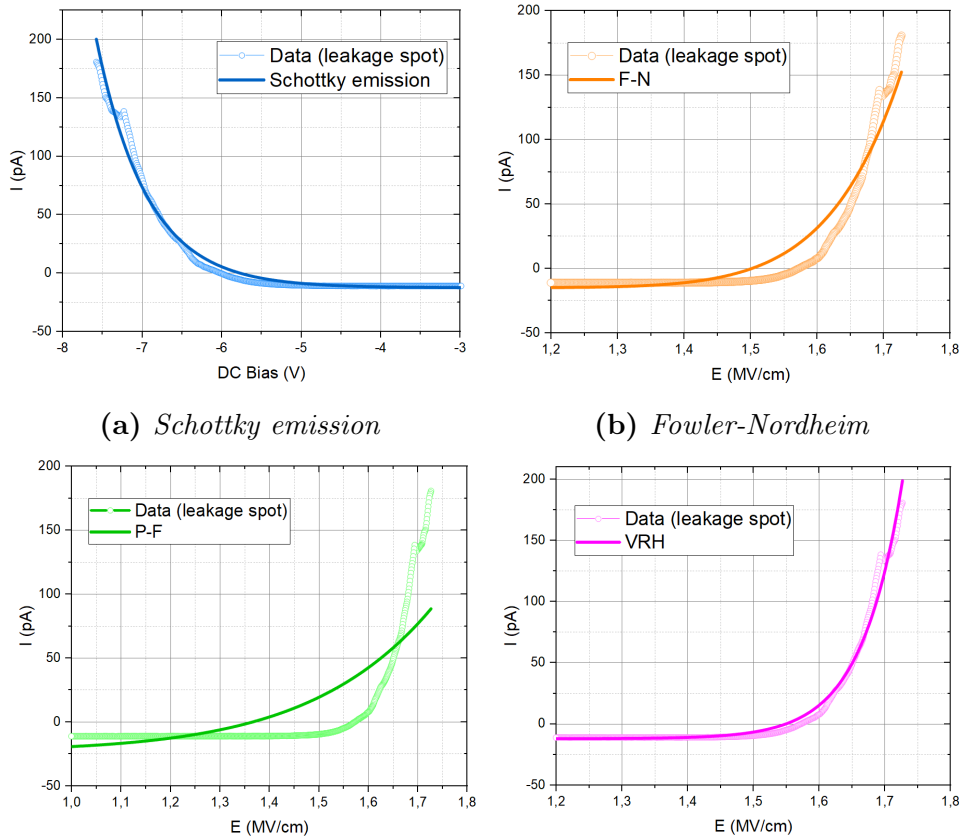

(a) *Schottky emission* **(b)** *Fowler-Nordheim*

(c) *Poole-Frenkel* **(d)** *Varibale Range Hopping*

Figure 3.29: *Schottky emission, Fowler-Nordheim tunneling, Poole-Frenkel emission and Variable Range Hopping fitting of I-V curves taken with Pt/Ir tips using a Bruker's Dimension Icon AFM with TUNA current amplifier.*

Range Hopping model provides the best fit and the most reliable results. Indeed, for what concerns thermionic emission, the ideality factor obtained from the fit is too high to be reliable. In particular, the fitting of VRH was realized by considering the following definitions

$$\mu = \frac{\nu_0 b}{2E} e^{-(\frac{\sigma}{kT})^2} (e^{(ebE/kT)} - 1) \tag{3.2}$$

$$\nu_0 = \Gamma_1 e^{(\frac{-4\pi}{h})\sqrt{2m^*\Phi_T}} \tag{3.3}$$

The parameters employed were the ones used by Moroz et al. [42], such as the escape frequency Γ_1=10^{13} s^{-1}, and σ=80 meV. Besides, it was used the effective mass of holes $m^* = 1.4m_0$ and the carrier density was estimated to be $n = \frac{1}{\pi r_d^2 b}$, with $r_d = 0.5$ nm [42]. The distance between the trap state along the dislocation b and trap energy E_t were the only free parameters. b was estimated to be 4.1±0.3 nm, corresponding to eight times the lattice parameter c. Linear charge density along the dislocation was estimated to be λ=$e/8c$=-39.1 pC/m, lower if compared with literature values [41]. However, this higher distance between traps could indicate a lower trap decoration of these defects. For what concerns the trap energy, it was found equal to Φ_T=0.4±0.1 eV. By comparing it with some studies, it seems compatible with the activation energy of N vacancy [64], [41]. The potential existence of nitrogen vacancies at the cores of dislocations in specific core configurations has been suggested by some DFT calculations [61]. This presence of nitrogen vacancies could possibly act as electron traps, enabling electron tunneling conduction. These results were achieved by using multiple assumptions and parameters. A large error

Parameter	***Fitted value***
b (nm)	4.1±0.3
Φ_t **(eV)**	0.4±0.1

Table 3.4: *Parameters achieved from the fitting of I-V curves by VRH model.*

was considered in order to account for the rough estimation of V_{bi}. A more precise result will be required to determine it from capacitance-voltage (C-V) analysis. Therefore, the extracted values should be considered as a rough estimate. Temperature-dependent measurements should be performed in order to confirm this result. However, it can be taken into account as a qualitative signature of Variable Range Hopping conduction responsible for leakage through electrically active dislocations.

3.2 Characterization of anomalous morphological features for UID sample

Several techniques, also in collaboration with other research groups, were employed in order to evaluate the nature of higher features on the UID sample surface (fig. 3.30). The hypothesis was about the presence of gallium oxide. Gallium that remained in the chamber during growth could have been absorbed on the surface forming a Ga-adlayer [65]. Instead, oxygen should not be present in the chamber, so it is supposed to reach the sample once exposed to air.

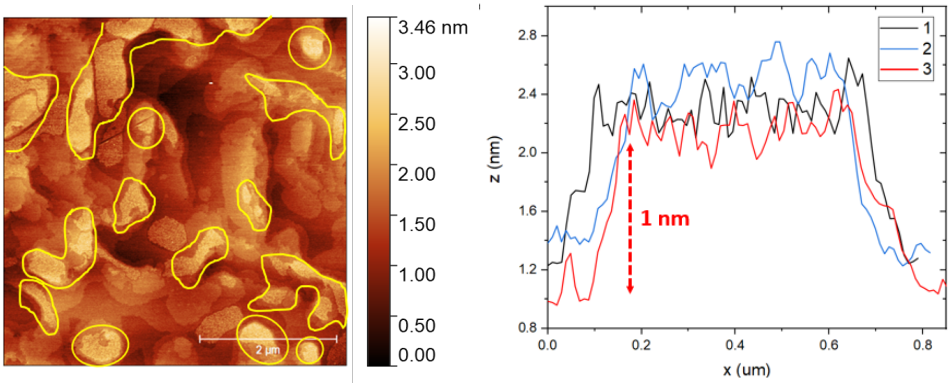

Figure 3.30: *(a) UID sample topography by AFM. Yellow marks indicate higher regions on the surface. (b) Line profile across three of the yellow-marked regions.*

3.2.1 Adhesion

Peak Force mode was employed in order to get the adhesion map on the surface of both samples. A peak force set point of almost 0.25 nN was employed. Figure 3.31 shows the result acquired on both UID and ELOG samples, by considering an area of 25 μm^2. The first is the only one to show the presence of a different contrast, in correspondence of higher regions from the topography image. Indeed, as it can be noticed from the line profile in fig. 3.32, adhesion was found to be lower at their site and this was the first indication of a different composition on that surface.

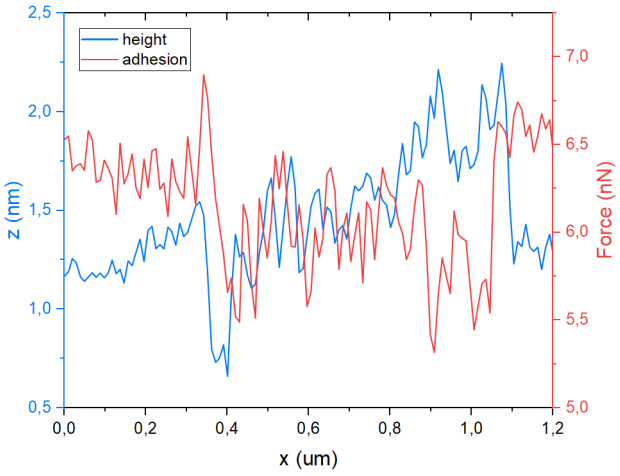

Figure 3.32: *Line profile acquired at one of the higher region in the topography map (blue) and at lower adhesion one (red).*

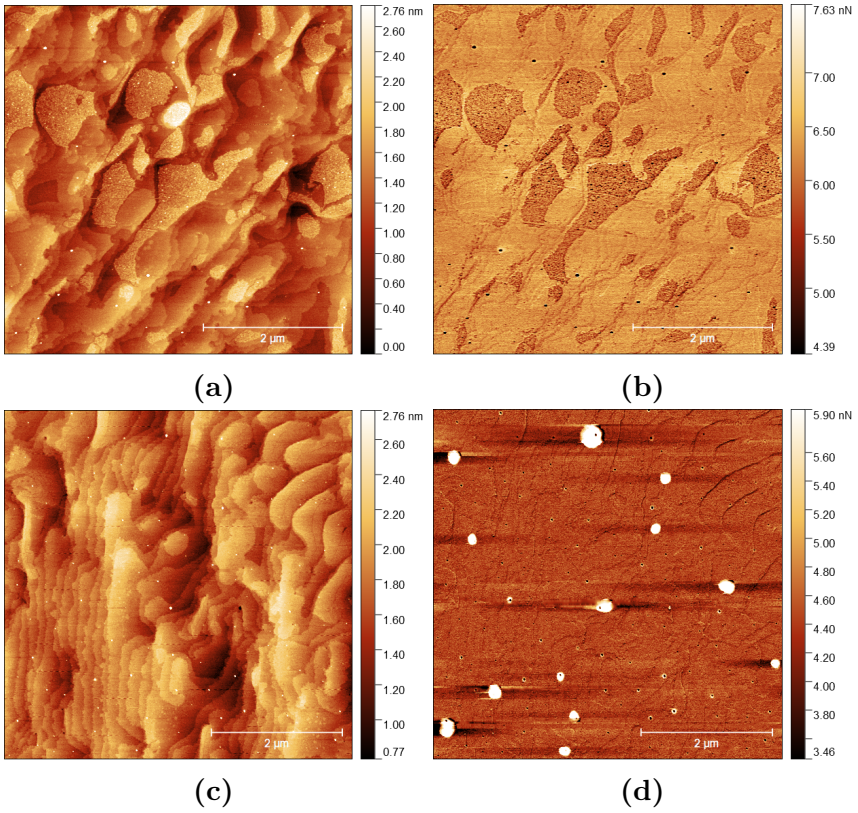

Figure 3.31: *The image displays the topography and adhesion maps of UID (a,b) ELOG (c,d) samples, by AFM in peak force mode.*

3.2.2 Conductive AFM

UID sample surface was probed by C-AFM, by using Pt/Ir and diamond tips. As shown in figure 3.34, it is possible to notice a correspondence between higher features on the topography and lower conductive regions in the current map (achieved by applying -2.2 V). The same measurement was conducted on ELOG sample, which showed instead a homogeneous current map. Spectroscopy was also performed over multiple points and, as shown in fig. 3.34, a difference in the threshold voltage was found by averaging on different curves. Averaged values obtained by fitting these curves are summarized in table 3.5. The higher absolute threshold voltage at the site of inhomogeneities was evidence of the validity of the oxide presence hypothesis.

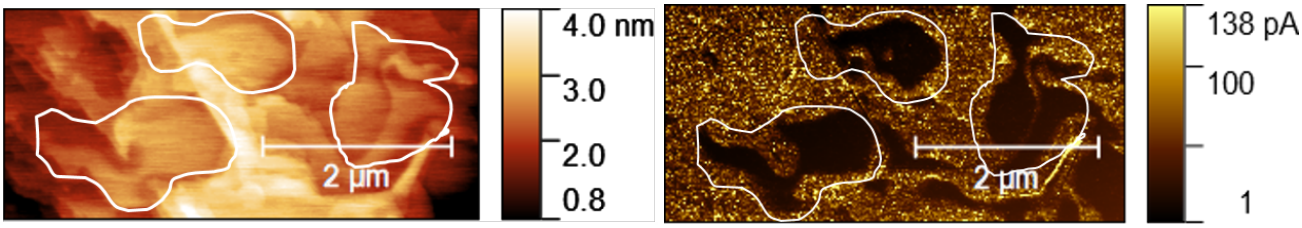

(a) (b)

Figure 3.33: *(a) Topography and (b) current map by C-AFM at -2.2 V.*

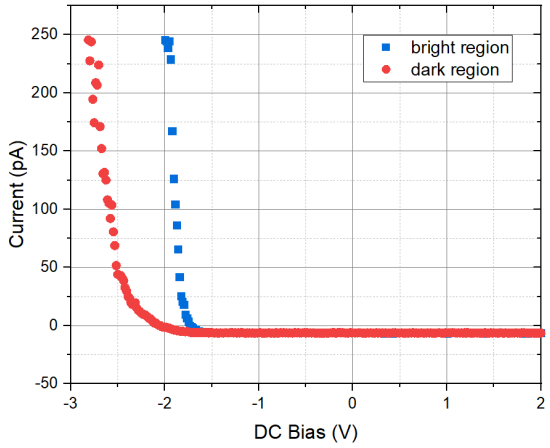

Figure 3.34: *I-V curve on dark (red) and bright (blue) regions of this map.*

	V_t
bright regions	-1.8 ± 0.2
dark regions	-2.6 ± 0.2

Table 3.5: *The table shows the threshold voltage averaged on different curves. They were acquired by performing current spectroscopy on different regions of the UID sample.*

3.2.3 X-ray Photoelectron Spectroscopy (XPS)

XPS measurements[1] were performed in order to probe surface composition. Measurements were done at an angle of 45°, by selecting a photon beam energy of 1486.6 eV. Reference, UID, and ELOG samples were all investigated to notice some differences,

[1] in collaboration with another team at IMEC

related to these unique features on the second sample. Data were analyzed through CasaXPS, in order to get the deconvolution of the peaks. From deconvoluted peaks (as shown in fig. 3.35), both binding energy and atomic concentration were established. For the first, calibration was performed on the C 1s spectrum at 248.8 eV. A sensitivity factor of 0.733, specific to each instrument, was used to convert peak areas to atomic concentrations. As a result of this, it is possible that the concentrations deviate from reality in the absolute sense (generally not more than 20% relative). Figure 3.35 displays

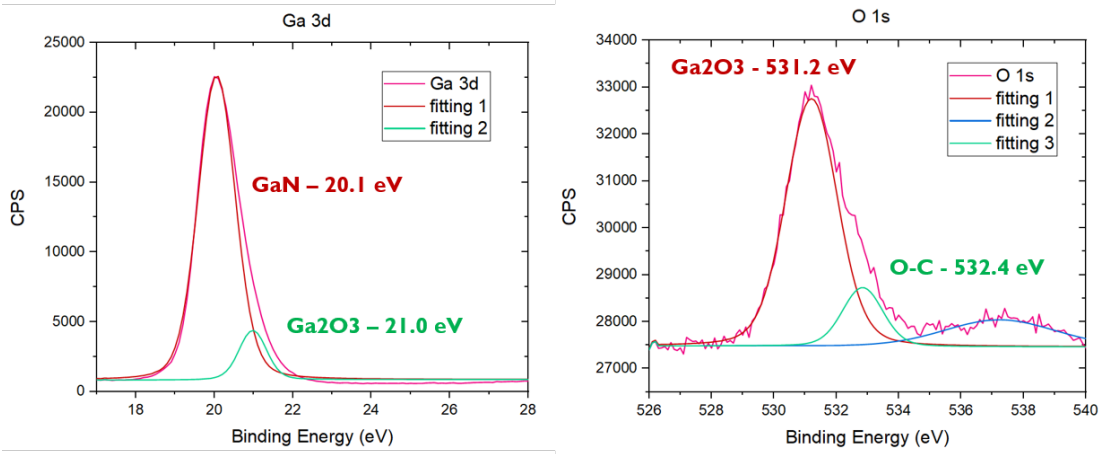

Figure 3.35: *Deconvoluted peaks from XPS Ga 3d and O 1s spectra, acquired on UID sample.*

the spectra of Ga 3d and O 1s. By comparing the binding energies (table 3.6) of the peaks with those reported in the literature, it was possible to determine that both spectra indicate the presence of gallium oxide, which aligns well with the initial hypothesis. The atomic concentration was calculated from spectra for all samples before and after Ar+ sputtering, a standard procedure for contamination removal. In particular, it was performed a low energy sputtering (100 eV) for 3 minutes. The results are shown in table 3.7. Regarding the oxygen percentage, as shown in the histogram in fig. 3.36, it is evident that only in the case of the UID sample it remains unchanged, while in the other cases, it consistently decreases. This suggests that oxygen in the UID sample may not be due to contamination.

	Binding Energy (eV)	Compound
Ga 3d	20.08 ± 0.02	GaN
	21.0 ± 0.1	Ga_2O_3
O 1s	531.21 ± 0.02	Ga_2O_3
	532.88 ± 0.05	O-C

Table 3.6: *The table shows the binding energy associated with the peaks from the deconvoluted spectra. Each binding energy was assigned to a specific compound through a comparison with the literature [66] [67].*

As grown	**O 1s**
RSF	0.733
UID	17.57
ELOG	13.79
reference	18.26

After sputtering	**O 1s**
RSF	0.733
UID	17.59
ELOG	11.27
Reference	13.07

Table 3.7: *On the left, the atomic concentration of O 1s for UID, ELOG, and reference samples (as grown). On the right, the same quantity after the sputtering process. The red box highlights the atomic concentration of the UID sample, which does not change after sputtering. 0.733 was used as the sensitivity factor.*

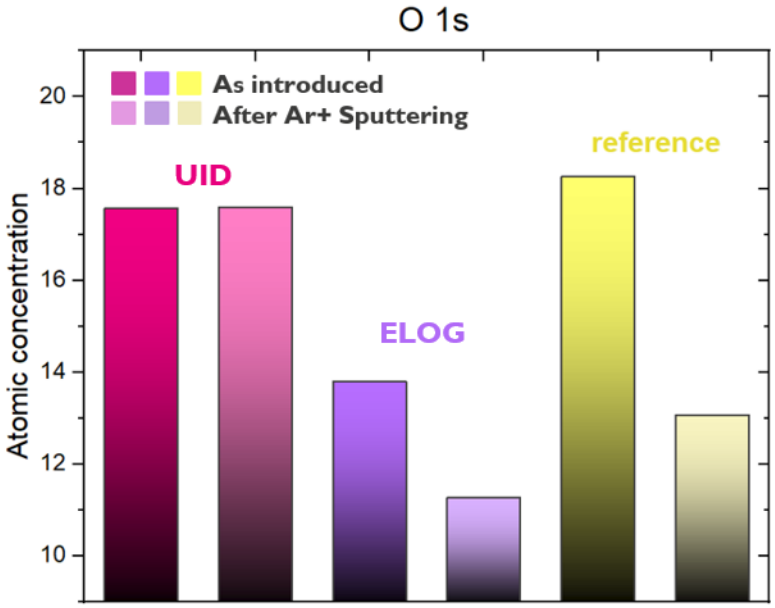

Figure 3.36: *The histogram shows the atomic concentration for reference, UID, and ELOG samples, before and after Ar+ sputtering.*

3.2.4 ToF-SIMS

ToF-SIMS[2] was used to generate a 15×15 μm^2 composition map of the surface. A beam of Bi^{1+} was employed, by selecting 30 keV as energy and 0.24 pA as current. The three images in fig. 3.37 depict the behavior of CN-, GaO-, and GaO_2- ions. It is evident that certain regions, as the ones marked by the white circle, exhibit an increase in GaO- and GaO_2- ions, accompanied by a decrease in CN- ions. This final outcome validates the initial hypothesis, confirming features characterized by a lower nitrogen percentage, as enriched in O.

[2]in collaboration with another team at IMEC

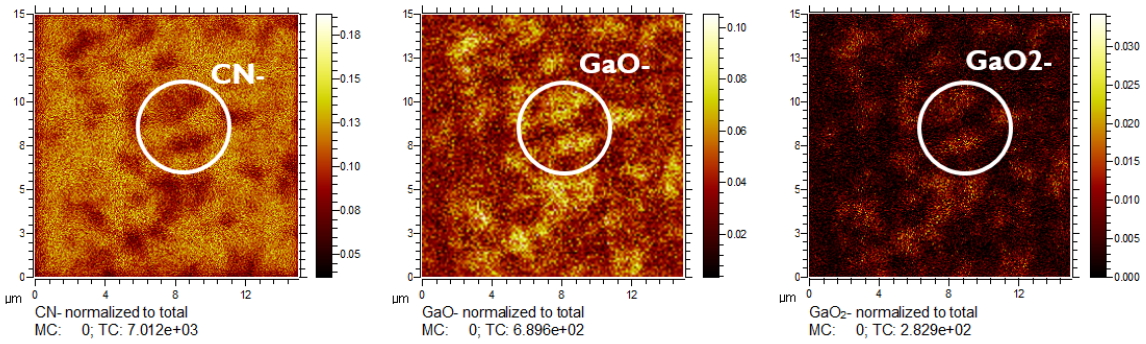

Figure 3.37: *ToF-SIMS images of GaN-, GaO-, GaO2-, and CN- normalized to the total ion image.*

3.2.5 Cathodoluminescence

During the employment of cathodoluminescence to obtain a reliable value for dislocation density, the presence of inhomogeneities in the signal background was observed. Notably, surface morphology inhomogeneities of UID sample appeared to exhibit different behavior also in terms of luminescence. This measurement was repeated on the UID sample both before and after etching with aqua regia and KOH (fig. 3.38). The electron beam voltage was set at 5 kV beam current at 0.80 nA to get the best resolution. From these CL maps it is possible to notice that while as-grown sample luminescence is higher at the site of inhomogeneities (fig. 3.38 (a)), the behavior is inverted after KOH etching (fig. 3.38 (c)). Besides, features seem to disappear after aqua regia etching (fig. 3.38 (e)).

3.2.6 Kelvin Probe Force Microscopy (KPFM)

In order to understand the distinct luminescence behavior, KPFM was employed to acquire maps of the band bending at the surface. The measurement was conducted in FM mode within a vacuum chamber, at a pressure of 10^{-5} torr, applying an AC bias of 1.5 V at 2 kHz. An area of 25 μm^2 was investigated. Once again, this measurement was repeated on the sample before and after etching with KOH and aqua regia. The CPD maps are shown in fig. 3.38 (b,d,f). Band bending can be derived from them by using the following relationship

$$\Phi_B = \phi_m - \chi_s - (E_c - E_F) - qV_{CPD} \tag{3.4}$$

where ϕ_m is the work function of the probe (5.5 eV for Pt/Ir [68]), χ_s is the electron affinity for GaN (4.1 eV [13]), $(E_c - E_F)$ is the energy difference from the Fermi level to

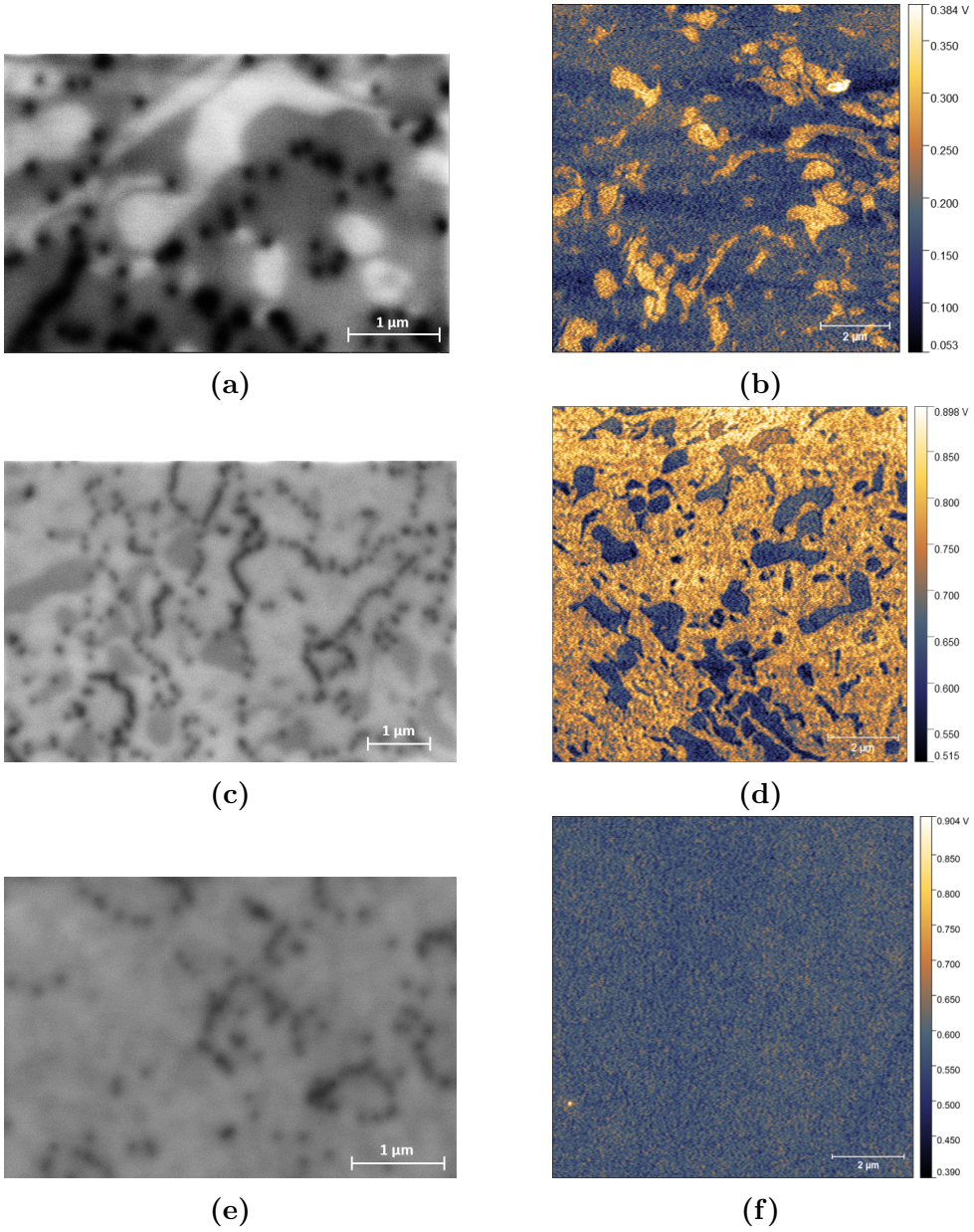

Figure 3.38: *On the left, CL maps of as grown (a) UID sample and after KOH (c) and aqua regia (e) etching. 5 kV was chosen as beam energy and 0.80 nA as beam current. On the right, CPD maps acquired by KPFM on as grown (b) UID sample and after KOH (d) and aqua regia (f) etching.*

the bottom of the conduction band (0.02 eV [69]), and qV_{CPD} is the contact potential difference measured experimentally. By considering that a higher CPD corresponds to

Band Bending (eV)	Inhomogeneities	Background
as grown	0.6	0.7
AR	-	0.8
KOH	0.8	0.6

Table 3.8: *The table summarizes the estimation of the band bending in correspondence of inhomogeneities and at the background by KPFM.*

O 1s	As grown	KOH
Ga_2O_3	18.48	4.13
OH	3.05	20.09

Table 3.9: *Atomic concentration of Ga_2O_3 and OH components, before and after KOH etching. The red box highlights the highest value, inverted after the etching process.*

a lower band bending, it becomes evident that the as-grown sample exhibits lower band bending in regions with inhomogeneities. After KOH etching the same inversion found for luminescence is recovered. On the other hand, aqua regia etching results in a uniform signal, aligning well with the previously observed uniform background in cathodoluminescence. This agreement indicates that the aqua regia etching is effective in removing the presence of inhomogeneities. Therefore, the comparison to CL maps shows a strong correlation with KPFM contrast.
In particular, band bending was roughly estimated by using eq. 3.5, and the results are summarized in table 3.8. XPS measurements were performed in order to find a relationship between the variation of band bending and the composition at the surface. By looking at O 1s spectra (fig. 3.39) and at the values of atomic concentration reported in table 3.9, it is possible to notice an inversion between the percentage of Ga_2O_3 and the OH group. Therefore, this could support the idea according to which the compositional change, due to KOH etching, is responsible for the band bending inversion.

In order to explain this result, the electric field existing at the surface must be considered. Calculations conducted in previous studies [47] have indicated that this field reaches magnitudes of approximately 10^5 V/cm up to a depth of 0.14 μm and it is capable of dissociating electron-hole pairs (fig. 3.40, right). Therefore, higher band bending within this electric field is expected to lead to a more effective dissociation. This process

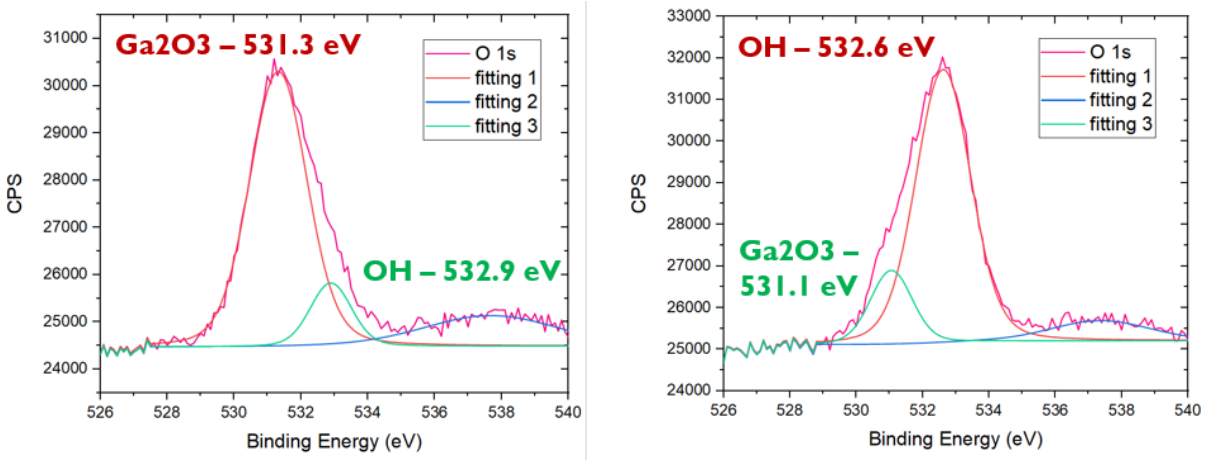

(a) **(b)**

Figure 3.39: *(a) O 1s XPS spectrum of UID sample (as grown). (b) O 1s XPS spectrum of UID sample after KOH etching.*

is summarized in the scheme in fig. 3.40, on the left. To ensure that the signal measured by CL originated from the surface, CASINO simulations were conducted by considering the same parameters used for CL measurement. The result is displayed in figure 3.41. These simulations revealed that approximately 90% of the signal is confined to the first 6 nm of depth, with most of the signal originating from the top layer, up to a depth of 200 nm. This finding validates that the CL signal primarily represents the surface behavior, which is influenced by the electric field and band bending effects. Therefore, this analysis allows us to conclude that the particular features noticed in the morphology of UID sample (fig. 3.42 (a)), related to gallium oxide (as confirmed by ToF-SIMS, in fig, 3.42 (b)), show a different luminescence in CL, as shown in fig, 3.42 (c), due to the band bending. It means that such a kind of local composition change seems sufficient to act on optical properties.

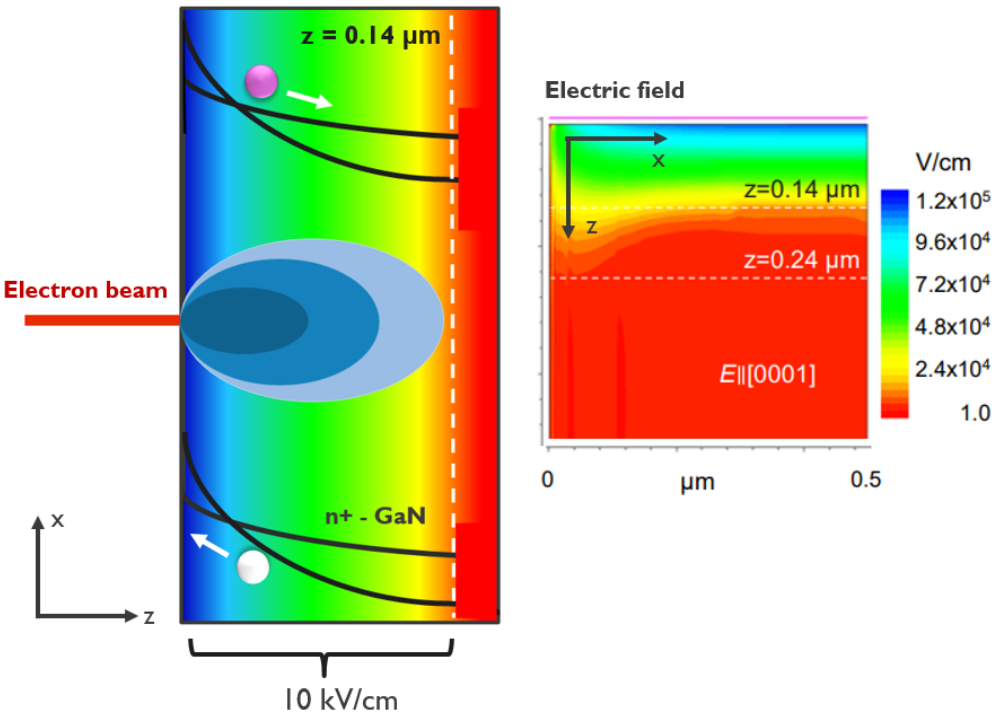

Figure 3.40: *Schematic of CL applied to the surface and band bending within the electric field, reproduced as shown in the simulation on the right [47].*

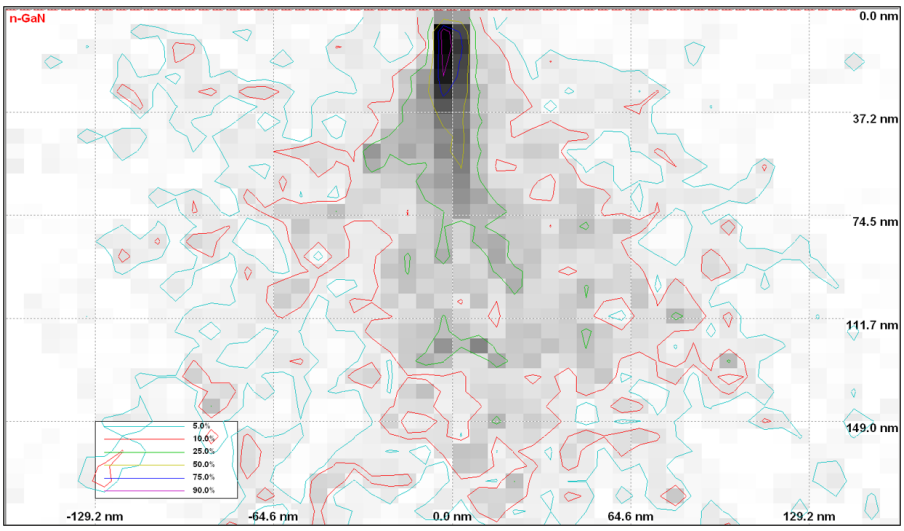

Figure 3.41: *CASINO simulation for GaN stack on UID showing the depth at which CL signal is confined.*

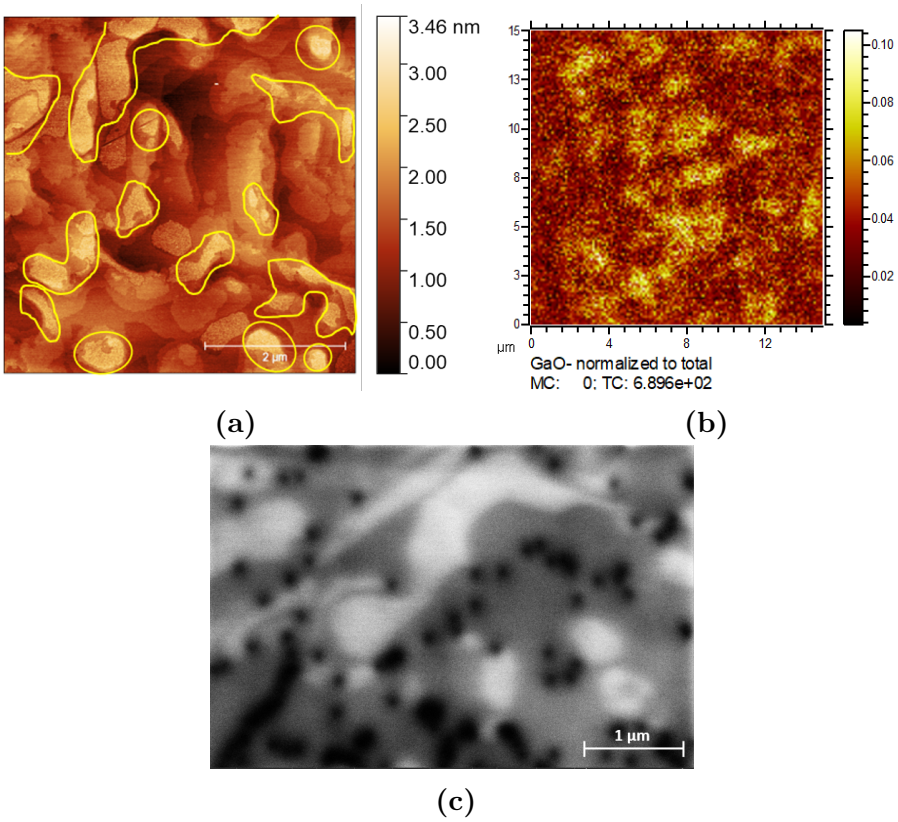

Figure 3.42: *(a) Topography by AFM on UID sample surface. (b) ToF-SIMS of the same surface, showing GaO- signal behaviour. (c) CL map, beam voltage 5 kV, beam current 0.80 nA.*

3.3 Chemical Etching of GaN in KOH: understanding of facet evolution

The formation of highly directional steps on GaN surface was observed in all three samples after 30% diluted KOH etching, as can be noticed in fig. 3.43. To get better images showing this process, a region on the reference sample surface was investigated before and after etching by AFM. The result is shown in fig. 3.44. A scratch was used to recognize the same region. White circles mark some of the regions that show the formation of these highly directional steps after the etching process.
The same effect has been observed in other studies [70] but with a different type of etching, and it was addressed to an anisotropy in the etching process. To explain this rather unusual step-edge anisotropy, the model developed by Xiu et al. [71] for growth was adapted to etching. In particular, it is possible to refer to the atomic configuration

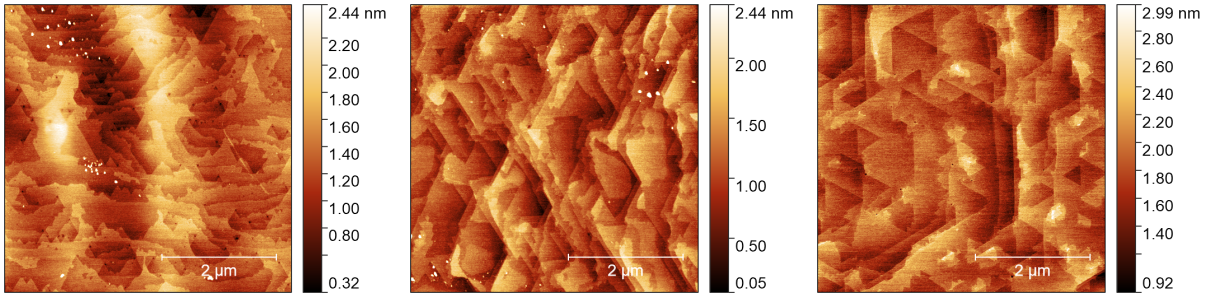

(a) **(b)** **(c)**

Figure 3.43: *Surface topography of (a) reference, (b) UID and (c) ELOG sample after KOH etching.*

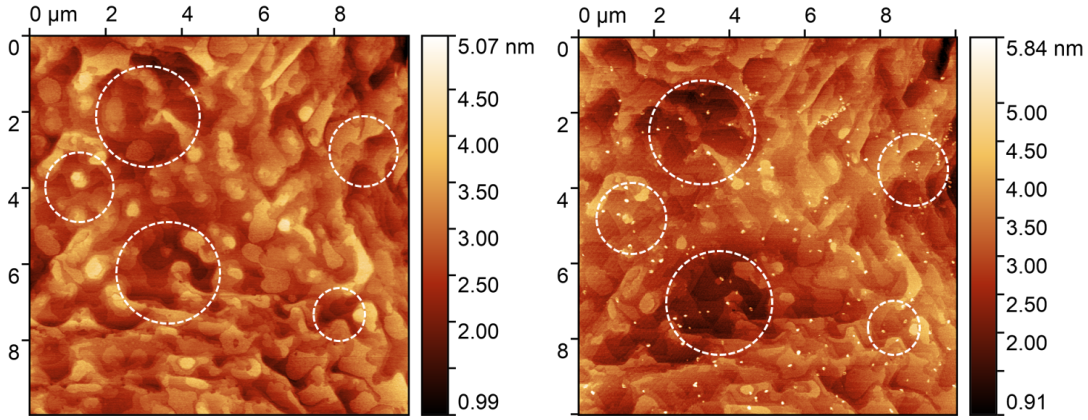

(a) *As grown* **(b)** *KOH*

Figure 3.44: *Comparison between the same area before and after KOH etching. White circles mark some regions at which highly directional steps formed.*

of a (111) bilayer lattice, labeling the symmetry crystallographic directions in both the fcc(111) (diamond or zincblende) and hcp(0001) (wurtzite) conventions (fig. 3.45). Considering only the dangling bonds in the bilayer, there are two types of step edges: type A edge, normal to [112] or equivalent directions, is characterized by two dangling bonds per edge atom and type B edge, normal to [211] or equivalent directions, is characterized by one dangling bond per edge atom (see fig. 3.46). For etching, the different rate is related to the number of nitrogen dangling bonds, that exert a repulsive force on hydroxyl group, that tries to break GaN bondings. This means that a higher number of them is related to a stronger repulsion and so to a less effective etching. Therefore, etching is expected to be faster along B step direction [72].

In order to verify this statement, an ECCI map of the reference sample surface was

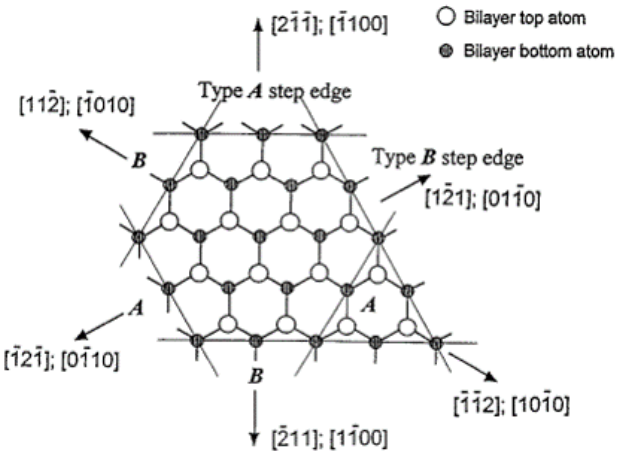

Figure 3.45: *Plan view of a bilayer, showing type A, B edges and fcc, hcp directions [71].*

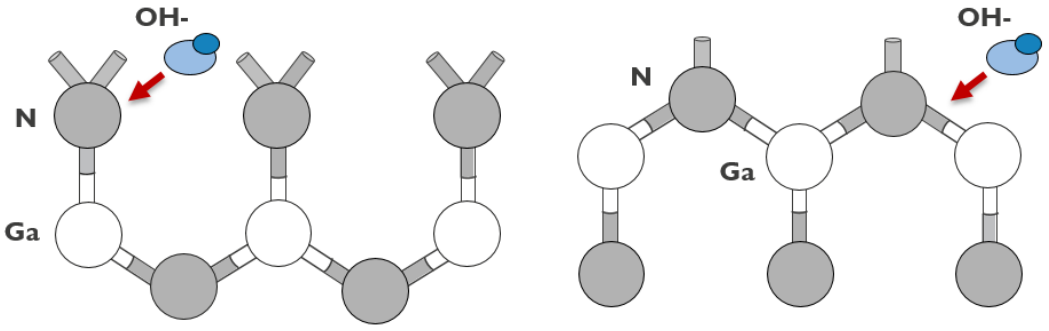

(a) *Step A* **(b) *Step B***

Figure 3.46: *Schematic diagram of steps A and B, with the hydroxyl group, from KOH, trying to break Ga-N bindings and nitrogen dangling bonds exerting a repulsive force.*

acquired, in which steps are clearly visible. Also, the ECP pattern was recorded. By exploiting ESPRIT DynamicS Bruker software it was possible to simulate the EBSD pattern, both kinematical (fig. 3.47 (a)) and dynamical (fig. 3.47 (b)). By comparing them with the experimental pattern, Kikuchi lines were addressed. The result is reported in fig. 3.48 (a). Through them, it was concluded that steps point in the [10-10] direction, as expected from the model. This is shown in fig. 3.48(b), in which one of the triangular features is marked by a white circle, and the directions are reported on the left side.

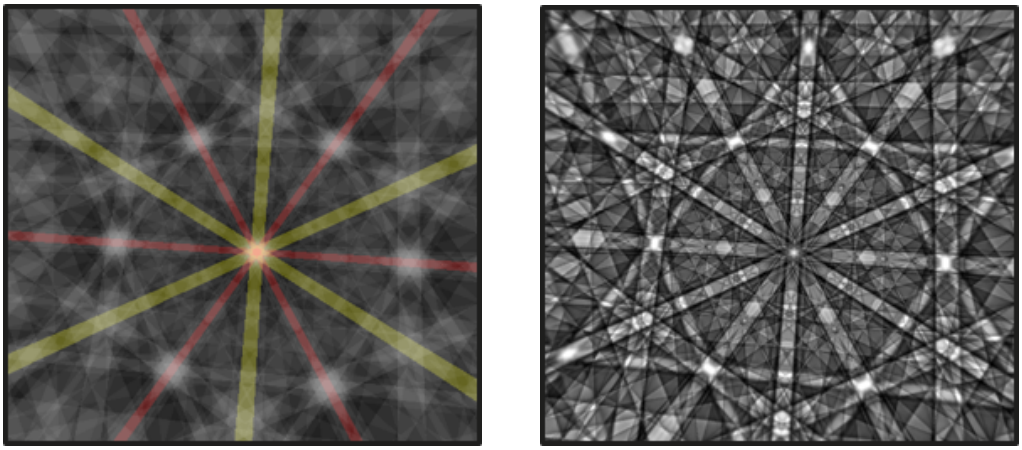

(a) *Kinematic Simulation* **(b)** *Dynamic Simulation*

Figure 3.47: *Kinematic and Dynamic simulations by ESPRIT DynamicS Bruker software. Yellow and red mark some of the Kikuchi lines in the pattern.*

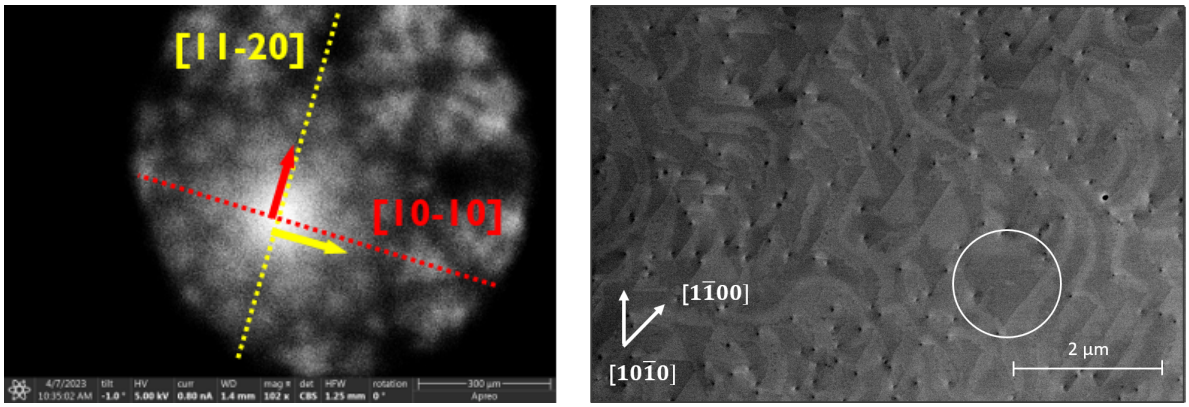

(a) *Experimental ECP* **(b)** *ECCI image*

Figure 3.48: *The experimental ECP pattern and the corresponding ECCI image. (a) Yellow and red lines are the ones achieved from the simulation. The corresponding directions are indicated. (b) The white circle marks one of the triangular features. Directions are reported on the side.*

Conclusions

The main goal of this thesis was to characterize two semi-vertical GaN stacks on QST® substrates, that differ for the type of buffer layer, named UID and ELOG, focusing on the dislocation density and evaluating their electric properties, by Scanning Probe Microscopy techniques. Electron Microscopy was also necessary to provide a complete characterization.
In particular, to measure the dislocation density, sample surfaces were probed by Atomic Force Microscope. In order to make dislocation pits more visible and to remove eventual contamination, aqua regia and KOH etching were both tried. Due to the complex morphology of the surface, which did not allow a reliable estimation of this density, Electron Channeling Contrast Imaging and Cathodoluminescence techniques were employed. The latter provided the most accurate result, thanks to the higher color contrast and the sensitivity to dislocations. The following table (3.10) summarizes dislocation density values.

	Dislocation density $(10^8\ cm^{-2})$		
	CL	**ECCI**	**AFM**
UID	6.1±0.5	1.3±0.3	0.5±0.1
ELOG	2.0±0.1	1.0±0.04	0.8±0.2
Reference	7.8±0.1	0.8±0.1	8.1±0.2

Table 3.10: *Table summarizes the dislocation density achieved by CL, ECCI, and AFM techniques from the three samples.*

Electrical properties were evaluated through Scanning Capacitance Microscopy and Conductive Atomic Force Microscopy. The first was used to perform a characterization on both the surface and cross-section of the sample. The latter allowed us to probe dislocations within the drift layer, in a full-grown device. Dislocations were confirmed, as shown in previous studies, to behave as deep acceptors, giving rise to a positively

charged space charge region in the surroundings. Besides, C-AFM analysis on beveled samples allowed us to probe the presence of leakage spots. By estimating their density, it was possible to conclude that they were 1% of total dislocation density, suggesting that probably pure screw dislocations could be the source of leakages. This represents an important step for what concerns the ongoing debate about the electrical activity of these defects. Moreover, a quantitative analysis of the dominant transport mechanisms was performed on the I-V curves, obtained through spectroscopy. This revealed that the Variable Range Hopping model is the most suitable to describe the transport at the interface between the tip and the p-type layer. Moreover, the distance between trap states along the dislocation and the trap energy were extracted by fitting this model. The results are summarized in table 3.11. By comparing this result to the literature, the trap energy was associated with nitrogen vacancies. A part of this study was also ded-

Parameter	***Fitted value***
b (nm)	4.1±0.3
Φ_t **(eV)**	0.4±0.1

Table 3.11: *Parameters achieved from the fitting of I-V curves by VRH model.*

icated to addressing the origin of the morphological features found in the UID sample. Adhesion characterization underlined the presence of a different chemical composition at their site. Besides, the current probed by C-AFM by applying the same bias, at their site, was considerably lower. For this reason, it was hypothesized that gallium oxide adlayer could be present and this idea was confirmed by XPS and ToF-SIMS results. Moreover, it was also noticed, by performing CL on this sample, the presence of a different contrast. Indeed, the luminescence increased at inhomogeneities. Kelvin Probe Microscopy was employed to determine the link with band bending. In particular, higher luminescence may be explained as due to the lower band bending at these features. By considering the electric field at the sample surface, lower band bending is associated with a weaker electron-hole pairs separation. This link was found also for the samples etched by KOH. In that case, an inverted behavior at inhomogeneities was noticed, as KOH had determined a larger band bending and thus a lower luminescence with respect to the background. About aqua regia, both on CL and KPFM maps, inhomogeneities seem to have disappeared after this kind of etching. Therefore, this study suggests a strong correlation between band bending and luminescence, which can be altered locally by the variation of chemical composition.
The third section of the work was devoted to the explanation of the formation of highly directional steps after KOH etching. This phenomenon was attributed to the presence of anisotropy in the etching process, due to the different number of nitrogen dangling

bonds at the two kinds of steps that characterize the GaN surface. Indeed, nitrogen dangling bonds exert a repulsive force on the hydroxyl group that tries to break GaN bonding. This determines a less effective etching of one step with respect to the other. The hypothesis was verified by addressing the direction of the steps and comparing it with the expected one from the model. Even if KOH etching is widely used on GaN, this kind of phenomenon was not explained in the literature, also because it was obtained by a particularly diluted KOH, differently from the molten one often employed in this kind of process.
The findings of this thesis hold significant potential for enhancing the development strategy of GaN-based power devices with applications reaching 1.2 kV and for a deeper understanding of GaN epitaxy on engineered substrates. Furthermore, the study of leakages from dislocations could be used to calibrate future TCAD simulations and contribute to the ongoing debate on the electrical activity of dislocations. Further studies could be dedicated to the employment of correlative methodologies to determine unequivocally the dislocation type of the conductive ones.

Acknowledgements

I would like to express my deepest gratitude to Professor Daniela Cavalcoli for her mentorship and helpfulness. I am grateful for giving me the opportunity to join IMEC and to work on this project.
I want to thank Albert Minj for mentoring me through this journey at IMEC, for his big support, and for his valuable teachings. I sincerely thank my manager Thomas Hantschel for allowing me to join his team and for the precious weekly discussion.
A special thanks also to Anurag Vohra and Karen Geens for providing me the samples, to Han Han and Fiona Mascarenhas for the acquisition of SEM data, to Thierry Conard and Inge Vaesan for XPS measurements, and to Celine Noel and Alexis Franquet for ToF-SIMS analysis.
I also want to thank Dr. Andrea Ciavatti for the guidance in the laboratories of UniBO.

Bibliography

[1] Salvatore Musumeci and Vincenzo Barba. "Gallium Nitride Power Devices in Power Electronics Applications: State of Art and Perspectives". In: *Energies* 16.9 (2023), p. 3894.

[2] Amit Kumar et al. "Wide band gap devices and their application in power electronics". In: *Energies* 15.23 (2022), p. 9172.

[3] Vladimir Odnoblyudov Shari Farrens Cem Basceri. *Engineered substrate structure for power and RF applications*.

[4] Ander Udabe, Igor Baraia-Etxaburu, and David Garrido. "Gallium Nitride Power Devices: A State of the Art Review". In: *IEEE Access* (2023).

[5] Matteo Meneghini et al. "GaN-based power devices: Physics, reliability, and perspectives". In: *Journal of Applied Physics* 130.18 (2021).

[6] Kwan Chi Kao. *Dielectric phenomena in solids*. Elsevier, 2004.

[7] Hadis Morkoç, Roberto Cingolani, and Bernard Gil. "Polarization effects in nitride semiconductors and device structures". In: *Material Research Innovations* 3 (1999), pp. 97–106.

[8] Safa Kasap and Peter Capper. *Springer handbook of electronic and photonic materials*. Springer, 2017.

[9] John T Torvik. "Dopants in GaN". In: *III-Nitride Semiconductors: Electrical, Structural and Defects Properties*. Elsevier, 2000, pp. 17–49.

[10] W Götz et al. "Local vibrational modes of the Mg–H acceptor complex in GaN". In: *Applied Physics Letters* 69.24 (1996), pp. 3725–3727.

[11] Shuji Nakamura et al. "Thermal annealing effects on p-type Mg-doped GaN films". In: *Japanese Journal of Applied Physics* 31.2B (1992), p. L139.

[12] Yoshitaka Nakano, Osamu Fujishima, and Tetsu Kachi. "Effect of p-type activation ambient on acceptor levels in Mg-doped GaN". In: *Journal of applied physics* 96.1 (2004), pp. 415–419.

[13] `https://www.ioffe.ru/SVA/NSM/Semicond/GaN/bandstr.html`.

[14] Yuhao Zhang, Armin Dadgar, and Tomás Palacios. "Gallium nitride vertical power devices on foreign substrates: a review and outlook". In: *Journal of Physics D: Applied Physics* 51.27 (2018), p. 273001.

[15] Taofei Pu et al. "Review of recent progress on vertical GaN-based PN diodes". In: *Nanoscale Research Letters* 16.1 (2021), p. 101.

[16] Shizuo Fujita. "Wide-bandgap semiconductor materials: For their full bloom". In: *Japanese journal of applied physics* 54.3 (2015), p. 030101.

[17] Masataka Higashiwaki et al. "Recent progress in Ga2O3 power devices". In: *Semiconductor Science and Technology* 31.3 (2016), p. 034001.

[18] Wengang Wayne Bi et al. *Handbook of GaN semiconductor materials and devices*. CRC Press, 2017.

[19] Matteo Meneghini et al. "GaN-Based Lateral and Vertical Devices". In: *Springer Handbook of Semiconductor Devices* (2022), pp. 525–578.

[20] Joseph P Kozak et al. "Stability, Reliability, and Robustness of GaN Power Devices: A Review". In: *IEEE Transactions on Power Electronics* (2023).

[21] Albert Minj. "Nanoscale-electrical and optical properties of iii-nitrides". In: (2013).

[22] Vladimir Odnoblyudov, Ozgur Aktas, and Cem Basceri. "Fundamentals of CTE-matched QST® substrate technology". In: *Thermal Management of Gallium Nitride Electronics*. Elsevier, 2022, pp. 251–274.

[23] Shuji Nakamura Shuji Nakamura. "GaN growth using GaN buffer layer". In: *Japanese Journal of Applied Physics* 30.10A (1991), p. L1705.

[24] D Hull and DJ Bacon. *Introduction to Dislocations 5th edn Butterworth*. 2011.

[25] JP Hirth and J Lothe. "Effects of Crystal Structure on Dislocations". In: *Theory of dislocations. Second edition. John Wiley & Sons. Inc* (1982), pp. 217–266.

[26] Z Zhuang, Z Liu, and Y Cui. *Dislocation-based single-crystal plasticity model*. 2019.

[27] Vasily Bulatov and Wei Cai. *Computer simulations of dislocations*. Vol. 3. OUP Oxford, 2006.

[28] M Willander and Suresh C Jain. *Silicon-Germanium Strained Layers and Heterostructures: Semi-conductor and semi-metals series*. Elsevier, 2003.

[29] MA Moram et al. "On the origin of threading dislocations in GaN films". In: *Journal of Applied Physics* 106.7 (2009).

[30] JWP Hsu et al. "Inhomogeneous spatial distribution of reverse bias leakage in GaN Schottky diodes". In: *Applied Physics Letters* 78.12 (2001), pp. 1685–1687.

[31] Bumho Kim et al. "Investigation of leakage current paths in n-GaN by conductive atomic force microscopy". In: *Applied Physics Letters* 104.10 (2014).

[32] Jin Wang et al. “Do all screw dislocations cause leakage in GaN-based devices?” In: *Applied Physics Letters* 116.6 (2020).

[33] Takeaki Hamachi et al. “Comprehensive analysis of current leakage at individual screw and mixed threading dislocations in freestanding GaN substrates”. In: *Scientific Reports* 13.1 (2023), p. 2436.

[34] Shigeyoshi Usami et al. “Correlation between dislocations and leakage current of pn diodes on a free-standing GaN substrate”. In: *Applied Physics Letters* 112.18 (2018).

[35] Shigeyoshi Usami et al. “Effect of dislocations on the growth of p-type GaN and on the characteristics of p–n diodes”. In: *physica status solidi (a)* 214.8 (2017), p. 1600837.

[36] Tetsuo Narita et al. “Identification of type of threading dislocation causing reverse leakage in GaN p–n junctions after continuous forward current stress”. In: *Scientific Reports* 12.1 (2022), p. 1458.

[37] Handong Jin et al. “It’s a trap! On the nature of localised states and charge trapping in lead halide perovskites”. In: *Materials Horizons* 7.2 (2020), pp. 397–410.

[38] Sven Besendörfer et al. “The impact of dislocations on AlGaN/GaN Schottky diodes and on gate failure of high electron mobility transistors”. In: *Scientific reports* 10.1 (2020), p. 17252.

[39] Brett Setera and Aristos Christou. “Threading dislocations in GaN high-voltage switches”. In: *Microelectronics Reliability* 124 (2021), p. 114336.

[40] Fu-Chien Chiu et al. “A review on conduction mechanisms in dielectric films”. In: *Advances in Materials Science and Engineering* 2014 (2014).

[41] Alexander Y Polyakov and In-Hwan Lee. “Deep traps in GaN-based structures as affecting the performance of GaN devices”. In: *Materials Science and Engineering: R: Reports* 94 (2015), pp. 1–56.

[42] Victor Moroz et al. “The impact of defects on GaN device behavior: Modeling dislocations, traps, and pits”. In: *ECS Journal of Solid State Science and Technology* 5.4 (2016), P3142.

[43] S Banerjee et al. “Defect Characterization of GaN stacks for Vertical Device Fabrication on 200 mm Engineered Substrates by TEM, CL and ECCI”. In: *to be published* (2023).

[44] Ricardo Garcıa and Ruben Perez. “Dynamic atomic force microscopy methods”. In: *Surface science reports* 47.6-8 (2002), pp. 197–301.

[45] Wilhelm Melitz et al. “Kelvin probe force microscopy and its application”. In: *Surface science reports* 66.1 (2011), pp. 1–27.

[46] Rachel A Oliver. "Advances in AFM for the electrical characterization of semiconductors". In: *Reports on Progress in Physics* 71.7 (2008), p. 076501.

[47] Albert Minj et al. "Correlating Structural and Electrical Characteristics of Threading Dislocations in Ga N-on-Si Heterostructures and p-n Diodes by Multiple Microscopy Techniques". In: *Physical Review Applied* 19.3 (2023), p. 034081.

[48] https://www.nanophys.kth.se/nanolab/afm/icon/bruker-help/Content/SoftwareGuide/NanoSco

[49] Stefan Zaefferer and Nahid-Nora Elhami. "Theory and application of electron channelling contrast imaging under controlled diffraction conditions". In: *Acta Materialia* 75 (2014), pp. 20–50.

[50] G Naresh-Kumar et al. "Rapid nondestructive analysis of threading dislocations in wurtzite materials using the scanning electron microscope". In: *Physical review letters* 108.13 (2012), p. 135503.

[51] Karl K Sabelfeld et al. "Dislocation contrast in cathodoluminescence and electron-beam induced current maps on GaN (0 0 0 1)". In: *Journal of Physics D: Applied Physics* 50.40 (2017), p. 405101.

[52] Fred A Stevie and Carrie L Donley. "Introduction to x-ray photoelectron spectroscopy". In: *Journal of Vacuum Science & Technology A* 38.6 (2020).

[53] Rajiv Kohli and Kashmiri L Mittal. *Developments in Surface Contamination and Cleaning, Vol. 1: Fundamentals and Applied Aspects*. William Andrew, 2015.

[54] L Lu et al. "Microstructure and origin of dislocation etch pits in GaN epilayers grown by metal organic chemical vapor deposition". In: *Journal of Applied Physics* 104.12 (2008).

[55] Dongzhu Lu et al. "Defect-related etch pits on crystals and their utilization". In: *Crystals* 12.11 (2022), p. 1549.

[56] Zhiyuan Gao et al. "Polarity results in different etch pit shapes of screw and edge dislocations in GaN epilayers". In: *2007 International Workshop on Electron Devices and Semiconductor Technology (EDST)*. IEEE. 2007, pp. 125–128.

[57] Dejin Zhuang and JH Edgar. "Wet etching of GaN, AlN, and SiC: a review". In: *Materials Science and Engineering: R: Reports* 48.1 (2005), pp. 1–46.

[58] B Heying et al. "Dislocation mediated surface morphology of GaN". In: *Journal of Applied Physics* 85.9 (1999), pp. 6470–6476.

[59] Jong Kyu Kim et al. "Effects of surface treatment using aqua regia solution on the change of surface band bending of p-type GaN". In: *Journal of electronic materials* 30 (2001), pp. 129–133.

[60] SL Rhode et al. "Dislocation core structures in Si-doped GaN". In: *Applied Physics Letters* 107.24 (2015).

[61] I Belabbas, J Chen, and G Nouet. "Electronic structure and metallization effects at threading dislocation cores in GaN". In: *Computational materials science* 90 (2014), pp. 71–81.

[62] Filippo Giannazzo et al. "Electrical activation and carrier compensation in Si and Mg implanted GaN by Scanning Capacitance Microscopy". In: *Solid State Phenomena* 131 (2008), pp. 491–496.

[63] JWP Hsu et al. "Direct imaging of reverse-bias leakage through pure screw dislocations in GaN films grown by molecular beam epitaxy on GaN templates". In: *Applied physics letters* 81.1 (2002), pp. 79–81.

[64] Song Yang et al. "Identification of trap states in p-GaN layer of a p-GaN/AlGaN/GaN power HEMT structure by deep-level transient spectroscopy". In: *IEEE Electron Device Letters* 41.5 (2020), pp. 685–688.

[65] AR Smith et al. "Reconstructions of GaN (0001) and (0001) surfaces: Ga-rich metallic structures". In: *JOURNAL OF VACUUM SCIENCE AND TECHNOLOGY B MICROELECTRONICS AND NANOMETER STRUCTURE* 16 (1998), pp. 2242–2249.

[66] CD Wagner et al. "NIST standard reference database 20, Version 3.4 (Web version)". In: *National Institute of Standards and Technology: Gaithersburg, MD* 20899 (2003).

[67] Ali Mahmoodinezhad et al. "Low-temperature growth of gallium oxide thin films by plasma-enhanced atomic layer deposition". In: *Journal of Vacuum Science & Technology A* 38.2 (2020).

[68] B Narsimha Reddy, P Naresh Kumar, and Melepurath Deepa. "A poly (3, 4-ethylenedioxypyrrole)–au@ WO3-based electrochromic pseudocapacitor". In: *ChemPhysChem* 16.2 (2015), pp. 377–389.

[69] Rong Huang et al. "Angular dependent XPS study of surface band bending on Ga-polar n-GaN". In: *Applied Surface Science* 440 (2018), pp. 637–642.

[70] S Kuwano et al. "Bilayer-by-bilayer etching of 6H-GaN (0 0 0 1) with Cl". In: *Surface science* 561.2-3 (2004), pp. L213–L217.

[71] MH Xie et al. "Anisotropic step-flow growth and island growth of GaN (0001) by molecular beam epitaxy". In: *Physical review letters* 82.13 (1999), p. 2749.

[72] Yung-Yu Lai et al. "The study of wet etching on GaN surface by potassium hydroxide solution". In: *Research on Chemical Intermediates* 43 (2017), pp. 3563–3572.